AD632106

Final Report

ONE-DIMENSIONAL STRESS WAVE PROPAGATION IN SOILS

Prepared for:

DEFENSE ATOMIC SUPPORT AGENCY
WASHINGTON, D.C. 20301

CONTRACT DA-49-146-XZ-343

STANFORD RESEARCH INSTITUTE

MENLO PARK, CALIFORNIA

*SRI

STANFORD RESEARCH INSTITUTE

SRI

DASA 1757

February 1966

Final Report

ONE-DIMENSIONAL STRESS WAVE PROPAGATION IN SOILS

Prepared for:

DEFENSE ATOMIC SUPPORT AGENCY
WASHINGTON, D.C. 20301

CONTRACT DA-49-146-XZ-343

By: LYNN SEAMAN

SRI Project PHU-5184

Approved: E. G. CHILTON, MANAGER
MECHANICS DEPARTMENT
PHYSICS DIVISION

Copy No. 16

PREFACE

The research reported here was sponsored by the Defense Atomic Support Agency and monitored by Lt. Frank Brady Jr. The study was conducted under Contract DA-49-146-XZ-343 from September 1964 to December 1965, and was a continuation of work begun in June 1959, under Contract DA-49-146-XZ-018, which has been published in four reports numbered DASA-1266-1 to DASA-1266-4.[1-4]

Supervisor for the project was Dr. Ernest G. Chilton and the project leader was Dr. Lynn Seaman. Dr. George N. Bycroft conducted and described the analysis in Appendix C. The analysis in Appendix D was prepared by Mr. Leonard McCulley and Dr. Clarence M. Ablow. The experiments were conducted by Dr. Seaman with the assistance of Messrs. Gerald Wagner, William Fehner, James Symes and Phillip Neketin.

Dr. Robert V. Whitman of Massachusetts Institute of Technology, the consultant on the project, helped to direct the course of the work. The Vicksburg clay soil used on the project was supplied by the Waterways Experiment Station of Vicksburg, Mississippi.

The notation has not been completely standardized for the whole report. Within the chapters the symbols are consistent and are listed before Chapter 1. The notation of each appendix is listed at the beginning of the appendix.

Test results are given in metric units. However, the soil column and some of the gages are designed using English units, and their discussions are shown in that system. The metric units used and their English equivalents are:

Quantity	Metric Unit	English Equivalent
Pressure, stress, modulus	1 bar*	14.50 psi
Length	1 cm	0.3937 in.
Wave Velocity	1 m/sec	3.281 ft/sec
Particle Velocity	1 cm/sec	0.03281 ft/sec

* One bar equals one million dynes/cm^2 and is approximately equal to one atmosphere.

ABSTRACT

Soil behavior during stress wave propagation was studied on a sand and two clays by making one-dimensional wave propagation tests on 5-meter long columns of the soils. Attempts were made to predict this behavior by determining soil properties in dynamic compression tests on small samples and by using these properties in a variety of mathematical models for soil.

In all the wave propagation tests, stress and acceleration records were very similar, showing that the three soils differ in degree, not in kind. Peak stress and particle velocity attenuated to 20-40% of the peak value in the length of the 5-meter column. The peak acceleration attenuated with the second power of arrival time. The rise time of the stress increased with depth. The wave velocity of the peak stress also increased with depth: average wave velocities ranged from 100 to 500 m/sec.

Both time-dependent and time-independent dissipation was observed in all soils. Time-dependent dissipation was dominant in soft clay; time-independent dissipation was more important in sand and stiff clay.

Two theoretical soil models were analyzed: one to investigate the effect of combined time-dependent and time-independent dissipation, and one to study the effects of nonlinear stress-strain relations and geostatic stress. Comparison of the theoretical predictions from the first of these and two previously studied models (using properties obtained from compression tests on soil samples) with the wave propagation results showed

1. For clays the arrival time of the wave at the column base was within 10% of that calculated from the tangent modulus, and for sand it was within 25%.

2. Attenuation of peak stress and particle velocity was predicted within ±50% at the base of the column (5-meter length).

One of the soils--a well-compacted kaolinite clay-exhibited an approximately linear loading relation during compression tests. Because of this linearity the model analyses were particularly applicable to the prediction of the behavior of this soil (all models used for predictions have linear loading relations). For this soil, attenuation was predicted within 10% and wave velocity within 5%; thereby verifying the usefulness of the theoretical models used.

In general, the earlier, simpler models are as suitable for predicting wave propagation behavior as the more complex models, but no single model can predict all properties reliably.

BLANK PAGE

CONTENTS

PREFACE ii

ABSTRACT iii

NOTATION FOR CHAPTERS 1 THROUGH 5 ix

CHAPTER 1 INTRODUCTION 1

1.1 Objective 1
1.2 Approach 1
1.3 Background 3

CHAPTER 2 SUMMARY AND RECOMMENDATIONS 5

2.1 Summary 5
2.2 Recommendations for Further Research 10

CHAPTER 3 PREDICTION PROCEDURE 13

CHAPTER 4 WAVE PROPAGATION EXPERIMENTAL RESULTS AND DISCUSSION . . . 19

4.1 Introduction 19
4.2 Test Conditions 19
4.3 Results 24
4.4 Discussion 52

CHAPTER 5 DISCUSSION OF THEORETICAL MODELS 65

5.1 Introduction 65
5.2 Viscoelastic Compacting and S-Hysteretic Models 66
5.3 Suitability for Use in Predictions 68

APPENDIX A DATA FROM WAVE PROPAGATION TESTS 72

A.1 Introduction 72
A.2 Test Facility and Gages 72
A.3 Soil and Test Conditions 81
A.4 Calibrations of Stress Gages 84

APPENDIX B SOIL PROPERTIES 90

B.1 Introduction 90
B.2 The MIT One-Dimensional Soil Tester 91
B.3 Test Procedure 93
B.4 Presentation of Data 96
B.5 Data Reduction: Dissipation Parameters 103
B.6 Data Reduction: Wave Velocity 106

CONTENTS (CONTINUED)

APPENDIX C VISCOELASTIC COMPACTING MEDIUM 115

C.1 Introduction 115
C.2 Wave Propagation Analysis 118
C.3 Justification for Use of Correspondence Principle 122
C.4 Results and Discussion 123

APPENDIX D NONLINEAR HYSTERETIC MEDIUM 137

D.1 Introduction 137
D.2 Governing Equations 138
D.3 Initial Values and the Linear Solution 144
D.4 Numerical Method 150
D.5 Results and Discussion 155

REFERENCES 163

TABLES

Table 4.1 Soils Tested 24

Table 5.1 Types of Soil Models 66

Table A.1 Gage Characteristics 81
Table A.2 Test Conditions 82
Table A.3 Representative Test Results 84

Table B.1 General Soil Properties 90
Table B.2 Dissipation Properties of the Soils 104

ILLUSTRATIONS

Figure

3.1 Stress Attenuation Prediction from the Constant Tan Delta Model 15
3.2 Stress Attenuation Prediction from the Linear Hysteretic Model 16

4.1 Two Segments of Soil Tube in Test Configuration 20
4.2 Soil Column Support Structure 21
4.3 Typical Soil Column and Gage Configuration 23
4.4 Stress Records from a Test on Column C 25
4.5 Idealized Stress Wave 26
4.6 Acceleration Records from a Test on Column C 27
4.7 Stress Attenuation: Column A, Kaolinite 30
4.8 Stress Attenuation: Column B, Kaolinite(T_0 = 6 msec) 31
4.9 Stress Attenuation: Column B, Kaolinite(T_0 = 2.5 msec) . . . 32
4.10 Stress Attenuation: Column C, Kaolinite 33
4.11 Stress Attenuation: Column D, Vicksburg Clay 34
4.12 Stress Attenuation: Column F, Vicksburg Clay 35
4.13 Stress Attenuation: Column E, Monterey Sand 36
4.14 Stress Wave Duration: Column B, Kaolinite 38
4.15 Stress Wave Duration: Column C, Kaolinite 39
4.16 Stress Wave Duration: Column D, Vicksburg Clay 39
4.17 Stress Wave Duration: Column F, Vicksburg Clay 40
4.18 Stress Wave Duration: Column E, Monterey Sand 41
4.19 Arrival Time-Depth Plot: Column C 43
4.20 Wave Velocity of the Peak Stress 44
4.21 Peak Acceleration 46
4.22 Peak Particle Velocity: Column B 48
4.23 Peak Particle Velocity: Column C 48
4.24 Peak Particle Velocity: Column D 49
4.25 Peak Particle Velocity: Column F 50
4.26 Peak Particle Velocity: Column E 51
4.27 Stress Attenuation with Nondimensional Depth: Column B . . . 56
4.28 Response of Embedded Stress Gage to Unloading 59
4.29 Static Unload Calibration for Embedded Stress Gages 60
4.30 Modification of Stress Record for Nonlinear Unloading Relation of Stress Gage 60
4.31 Time-Depth Plot for Calculation with Linear Hysteretic Model 63
A.1 Soil Tube Design 73
A.2 Soil Column Support Structure 74
A.3 Diaphragm Stress Gage 75
A.4 Piezoelectric Stress Gage 76
A.5 Surface Shear Gage used as a Force Gage 78
A.6 Force Gage G1 with Upper Disk Removed 79
A.7 Drop-Weights 80
A.8 Static Calibration of Two Stress Gages 86
A.9 Stresses in the Column 87

ILLUSTRATIONS (CONTINUED)

Figure

B.1 Grain Size Distribution for Monterey Sand 91
B.2 Loading Function for Compression Tests 92
B.3 Typical Stress-Strain Curve from Dynamic Compression Tests . . 92
B.4 MIT Dynamic One-Dimensional Soil Tester 94
B.5 Schematic Layout for Pressure System for MIT Tester 95
B.6 Stress-Strain Curves: Sample 1, Kaolinite 97
B.7 Stress-Strain Curves: Sample 2, Kaolinite 98
B.8 Stress-Strain Curves: Sample 3, Kaolinite 99
B.9 Stress-Strain Curves: Sample 4, Vicksburg Clay 100
B.10 Stress-Strain Curves: Sample 5, Monterey Sand 101
B.11 Measured Points on the Compression Test Data 102
B.12 Stress-Strain Curves from Cyclic Loadings: Constant Tan Delta Model 105
B.13 Computed Wave Velocities: Sample 1, Kaolinite 107
B.14 Computed Wave Velocities: Sample 2, Kaolinite (Predictions for Tests on Columns A and B) 108
B.15 Computed Wave Velocities: Sample 3, Kaolinite (Predictions for Tests on Column C) 109
B.16 Computed Wave Velocities: Sample 4, Vicksburg Clay (Predictions for Tests on Columns D and F) 110
B.17 Computed Wave Velocities: Sample 5, Monterey Sand (Predictions for Tests on Column E) 111

C.1 Stress-Strain Relation at Zero Rate of Strain 116
C.2 Representation of the Viscoelastic Compacting Model 117
C.3 Stress-Strain Relation for Response of Viscoelastic Compacting Model to a Half-sine Pressure Pulse 117
C.4 Stress Waves at Several Depths: Viscoelastic Compacting Model 124
C.5 Comparison of Attenuation by Viscous, Strain-Rate-Independent, and Combined Dissipation 124
C.6 Form of the Analytical Loading 127
C.7 Graphical Solution for Viscoelastic Parameters for the Viscoelastic Compacting Model 130

D.1 S=Shaped Stress-Strain Curve for Soil 140
D.2 The Characteristic Plane and Points Designated in the Analysis 145

D.3 Effect of Curvature and Geostatic Stress on Attenuation . . . 157
D.4 Effect of Curvature and Geostatic Stress on Attenuation . . . 158
D.5 Effect of Stress Level on Stress Attenuation 159
D.6 Effect of Stress Level on Particle Velocity Attenuation . . . 160
D.7 Effect of Applied Stress Duration on Stress Attenuation . . . 161
D.8 Effect of Applied Stress Duration on Particle Velocity Attenuation 161

NOTATION FOR CHAPTERS 1 through 5

c = wave velocity (meters/sec)

c_o = wave velocity at the surface, or wave velocity associated with $d\sigma/dt > o$

c_1 = wave velocity associated with $d\sigma/dt < o$

E = spring constants for viscoelastic compacting model (bars)

E_o = spring constant of series spring of viscoelastic compacting model, or modulus during loading for linear hysteretic model

E_1 = unloading modulus for linear hysteretic model

g = acceleration of gravity, 981 cm/sec^2

M = soil modulus

T = time required for stress to decay from its peak value to 0.368 times its peak value

T_o = value of T at the top of the soil column

t = time

t_p = time of peak stress

v = particle velocity (cm/sec)

v_m = peak particle velocity

v_{mo} = peak particle velocity at the surface

α = $(1 - \sqrt{E_o/E_1})/(1 + \sqrt{E_o/E_1}) = (1 - c_o/c_1)/(1 + c_o/c_1)$, the strain-rate-independent dissipation parameter

ϵ = strain

η = viscosity of viscoelastic compacting model (bar-sec)

ξ = viscous dissipation parameter denoting lag between peak strain and peak stress

ρ = density (gm/cm^3)

σ = stress

σ_m = peak stress

σ_{mo} = peak stress at the surface, applied peak stress

τ_p = t_p/T_o, nondimensional arrival time of the peak stress

BLANK PAGE

CHAPTER 1
INTRODUCTION

Knowledge of the response of soil to nuclear explosions is necessary for the proper design of underground protective structures. This study was concerned with the transmission of forces from the explosion through the soil to the vicinity of the structure. The dissipative properties of the soil modify the forces during transmission: the relationship between the dissipative properties and the modifications was studied on this project.

The present study was restricted to near-surface phenomena, to moderately-compacted soils similar to those found near the surface, and to overburden pressures produced by depths up to five meters. The applied loading had a peak value of several atmospheres and a duration of a few milliseconds. The loading history was similar to the pressure history of an airblast so that the study is especially pertinent to situations in which there is an air or surface burst. All the tests and analyses were concerned with one-dimensional phenomena only.

This project is the fourth in a series initiated for the study of wave propagation in soils. The particular feature of the present project is the extension to clay soils (previous projects dealt with sand). The results of the study can be used for design of underground structures and for correlation of data from large-scale field tests.

1.1 Objectives

The purpose was to study wave propagation in soils and to develop methods for predicting wave propagation phenomena.

1.2 Approach

Our approach consisted of three major phases:

1) The experimental determination of wave propagation phenomena in typical near-surface soils.

2) The dynamic testing of small samples of these soils in a laboratory dynamic compression tester.

3) The development of theoretical models which use the results from the laboratory compression tester to predict the wave propagation results.

For the wave propagation tests our approach was to apply a pulse loading to a one-dimensional column of soil. The pulse loading was similar to the airblast pressure wave from an explosion. The approach included measurements of stress and particle velocity in the soil to provide information on the stress wave caused by the pulse loading. Soils with a range of properties were studied to provide a broad base for a prediction procedure: dry sand, wet kaolinite clay, dry kaolinite, and a sticky, natural clay from Vicksburg, Mississippi.

Our approach in the conduct of compression tests was to attempt to duplicate the loading and soil conditions of the wave propagation tests on a small sample of the soil: same boundary conditions, stress levels, loading rates, water contents, and densities. Stress on the sample and strain of the soil sample were measured simultaneously during testing. The stress-strain data were then used to determine the wave velocity and dissipation parameters to be used for prediction of wave propagation phenomena.

The theoretical models were developed to study certain aspects of wave propagation and the relation between wave propagation phenomena and compression phenomena. The aspects considered were: attenuation and dissipation, nonlinearities of the stress-strain curve, and the geostatic stress. Each theoretical model studied contained two or more of these features. By comparing the theoretical prediction of these models with the measured wave propagation phenomena, we attempted to determine which features of soil behavior are significant, which features could be predicted and the degree of accuracy of the prediction.

1.3 Background

Many investigators have studied one-dimensional wave propagation phenomena to get some insight into three-dimensional phenomena. These one-dimensional studies should lead naturally toward an eventual understanding of three-dimensional phenomena. For experiments to approximate a one-dimensional case, conditions must be controlled in the other two dimensions. Strain and pressure are the conditions usually controlled, either by maintaining zero strain or constant pressure in the second and third dimensions. The constant lateral pressure condition was employed by E. T. Selig[5] and R. L. McNeill.[6] The zero lateral strain condition was used by W. Heierli,[7] R. V. Whitman,[8] J. V. Zaccor and N. R. Wallace,[9] H. W. Kriebel[2] and the present investigator. Each of these boundary conditions represents three-dimensional wave propagation conditions in certain limited regions surrounding an explosion.

The constant lateral pressure condition can be obtained by encasing the soil in a rubber membrane or tube and applying external pressure or internal vacuum. The zero lateral strain condition has been accomplished using a stiff tube (Heierli,[7] Kriebel,[2] present study) or a pressurized fluid boundary (Zaccor and Wallace[9]).

Pressures have been applied with a shock tube, a drop-weight, or a contained explosion. The soil response to the stress wave was measured with various transducers: stress gages, force gages, accelerometers, soil strain gages, and displacement gages.

Test results have been correlated in various ways by the different investigators, but for their tests on sands, all have used a strain-rate-independent model as the basis for analyses. Heierli had a good correlation of force history between experiments and analysis. Zaccor and Wallace were able to relate the wave velocity and particle velocity found in wave propagation experiments to the modulus measured in compression tests. Selig,[5] McNeill,[6] and Seaman and Whitman[4] were able to predict peak stress attenuation.

Theoretical analyses that have been conducted can be separated into two groups on the basis of the type of dissipative mechanism hypothesized for the soil. All the experimentalists mentioned earlier used nonlinear and strain-rate-independent models for soil. Other theoretical studies on this type of model have been published by Weidlinger and associates.[10-11-12]

The other dissipative model is strain-rate-dependent and has been studied recently for its applicability to soils by Kondner,[13,14] Christensen and Wu,[15] and Whitman.[16] Their experiments were in the form of dynamic compression tests on soil. These studies have shown that the dissipative character of certain clay soils is similar to that of the standard linear (3 element) viscoelastic model in the frequency ranges considered. The wave propagation calculations of Lai and Sauer[1] show that this model does not adequately represent the attenuation or wave front changes seen in actual soils. Thus, the model should be modified for application to wave propagation predictions. A viscoelastic model that exhibits the same dissipation at all frequencies (constant tan delta model) was analyzed by Bycroft.[3] Although the wave propagation behavior of this model is similar to that observed experimentally, its properties are different from those seen in compression tests.

CHAPTER 2

SUMMARY AND RECOMMENDATIONS

2.1 Summary

2.1.1 Wave propagation tests in sand and clay. One-dimensional wave propagation tests were performed on Monterey beach sand, a kaolinite clay, and a Vicksburg backswamp clay. These soils, which represent a wide range of soil properties, had a stiffness and density comparable to that of natural soils near the surface of the earth. One-dimensionality was obtained by confining the soil in a 5-meter long tube which allowed the soil to move along the axis of the tube but restrained the radial motion. Loading was in the form of a stress pulse with amplitudes up to 11 bars and durations from 2 to 6 msec.

These first complete one-dimensional tests on clays and the continuing tests on sand indicated that the wave transmission properties of the two materials were very similar. All soils exhibited both time-dependent and time-independent energy dissipation. The differences in the soils appeared in wave velocities and in the relative importance of the two types of dissipation. Stress and acceleration records obtained from tests on the sand and clays were qualitatively identical. The stress waves spread out and the peaks attenuate as they travel through the soil. For all tests the peak stress attenuated to between 1/5 and 2/5 of the applied peak in the length of the 5-meter column. The peak particle velocity attenuated the same amount. The peak acceleration attenuated with the second power of arrival time. The rise time of the stress and the wave velocity associated with the peak stress both increased with depth. The duration of the stress wave increased 4 or 5 times in the first 2 meters (and was not measurable beyond that depth because of the arrival of the reflected wave from the base of the soil column).

The test apparatus included an articulated soil tube for holding the soil, stress gages and accelerometers for measuring characteristics of the stress wave, and a drop-weight mechanism for applying the loading. The soil tube and accelerometers appeared to be adequate for the study. The stress gages exhibited certain calibration problems which affected all aspects of the stress data: the peak stresses were given within 20%, wave durations were lengthened as much as 60%, and rise times were altered an indeterminate amount. The drop-weight provided a stress pulse which lacked the shock front and exponential decay characteristic of air blast loadings. Because of this lack, the experimental conditions do not correspond exactly with either field conditions or conditions assumed for theoretical analyses.

2.1.2 Soils Properties from Compression Tests. One-dimensional dynamic compression tests were performed on samples of the soils under confinement conditions which closely approximated those used in the wave propagation tests. The compression tests were used to determine soil properties, particularly the moduli during loading and unloading and the dissipation characteristics. The moduli and dissipation characteristics, which are related to the behavior of the soil during wave propagation are determined from stress-strain data obtained during the compression tests. All of the soils showed a considerable difference between the loading and the unloading stress-strain relation. In the driest kaolinite soil, the loading relation was essentially linear, but the other soils exhibited a relation that was concave to the stress axis, i.e, stiffening on loading. In all cases, the unloading relation was concave to the stress axis.

The slopes of the stress-strain curves were measured to determine the soil modulus from which wave velocities for the soil were calculated. The tangent moduli at the stress level of 6 bars varied from 750 to 4800 bars (11,000 to 70,000 psi). For the sand, there was a small initial hump on the stress-strain curve; the size of the hump was proportional to the preload level. For the clay, the slopes are functions only of total stress level--preload plus dynamic stress increment. Time-dependent dissipation, as measured by the viscoelastic parameter tan δ, was prominent in the clays (tan δ = 0.3) but not so significant for the sand

($\tan \delta = 0.12$). Time-independent dissipation or compaction, measured by α, was important for sand and stiff clay ($\alpha = 0.12$ to 0.15) but could hardly be detected in the wet clay ($\alpha = 0.02$).

2.1.3 Theoretical Models. As a basis for correlating the wave propagation and compression test data, and eventually as a basis for wave propagation predictions, several theoretical models for soil have been analyzed. Each of the models represents only two or three of the dominant features of soil. The simplest models are characterized by two constants: one for wave velocity and one for dissipation. These models are the linear hysteretic model (dissipation independent of strain-rate) and the constant tan delta model (strain-rate-dependent dissipation), both of which were analyzed during a prior contract.[3]

A slightly more complex model with both strain-rate-independent and strain-rate-dependent dissipation was analyzed under the present contract. The analysis of this model, the viscoelastic compacting model, showed the interaction of the two types of dissipation in affecting attenuation and changes in wave shape. A fourth model with a nonlinear loading characteristic and strain-rate-independent dissipation (S-hysteretic model) was analyzed to study the effect of overburden or geostatic stress on wave propagation characteristics. For this model the attenuation rate is markedly reduced by the presence of the geostatic stress.

The numerical constants for the theoretical soil models were found from the dyanmic compression tests. Wave velocity was determined from the slope (tangent modulus) of the stress-strain curves. The lag time between the peak stress and the peak strain was used as a measure of the viscous dissipation parameter, $\tan \delta$. The ratio of the slopes of the stress-strain curves during loading and unloading was used as a measure of the compacting dissipation parameter, α.

2.1.4 Comparison of Theoretical and Experimental Results. A comparison of wave propagation results and of theoretical predictions based on compression test properties shows that

1. Arrival time of the stress wave can be predicted from the compression modulus of the soil, and

2. Stress attenuation can be predicted from the dissipative soil parameters found in the compression tests.

The correlation between the predicted and measured values was rather imprecise in most cases, but it showed that the approach is valid although improvements are needed in the testing and in the prediction procedure. Thus a rational basis for predicting wave propagation behavior from soil properties has been established.

One of the soils--kaolinite clay compacted at a water content of 18.8%--exhibited an approximately linear loading relation during compression tests. Because of the linearity, the model analyses were particularly applicable to the prediction of the behavior of this soil. (All three models used for predictions have linear loading relations.) Predictions were made for wave velocity, surface particle velocity, the variation of particle velocity with depth, and the attenuation of peak stress with depth. For this soil the experimental results agreed very well with these predictions, not only in trend but in magnitude. The attenuation with depth was predicted reasonably well by any of the three models used: constant tan delta, linear hysteretic, and viscoelastic compacting.

The other soils exhibited stress-strain relations which were definitely nonlinear. As might be expected, the correlation between the model predictions and the measured values from these soils was rather imprecise.

Attenuation of stress and particle velocity in the clays was best predicted by the constant tan delta model (purely time-dependent dissipation), although the data ranged ±50% of the prediction. For the sand, the soil column experiments showed a faster attenuation rate than any of the model predictions; however, the attenuation pattern was similar to that given by the viscoelastic compacting model (combined time-dependent and time-independent dissipation) and the values were within 50% of the predicted. It was found that the best abscissa for attenuation plots is a nondimensional arrival time: the actual arrival time divided by the loading duration. This same abscissa is indicated by all three models used for predictions. Experimental scatter is considerably reduced by

the use of this abscissa. Also, tests with loading durations from 1 msec to 10 msec have shown that the effect of load duration on attenuation is properly accounted for by this abscissa.

For the clay tests, the peak particle velocity at the surface was predicted from the simple equation $\rho c v = \sigma$, where ρ is density, c is wave velocity, v is particle velocity and σ is stress. In this case, the predicted value of particle velocity, v, was within 10% of the experimental values. For the sand, the predicted particle velocity was 50% higher than the experimental values.

Wave velocity was determined as the difference in arrival times of peak stress at two depths. The measured arrival times and wave velocities derived from them were correlated with the wave velocities and arrival times computed from the tangent moduli obtained from dynamic compression tests on the soil. For clay column tests the arrival times at the column base were predicted within 10% from the data on soil moduli; for sand the predictions were within 25%. The wave velocity data from the tests on rather dry kaolinite showed that the velocity was essentially the same at all depths and was predicted within a few percent from the tangent modulus measured in a dynamic compression test on the soil. For the other column tests, the experimental wave velocities tended to increase with depth while the values predicted from the modulus decreased with depth. This disparity indicates that the soil modulus does not provide a sufficient basis for predicting the wave velocity in detail. Other factors--geostatic stress, curvature of the stress-strain relation, time-dependence of the soil, and the rise time and duration of the stress wave--must all be brought in to make a complete prediction for wave velocity of the peak stress. The prediction of wave velocity from the tangent modulus obtained in dynamic compression tests should be compared with predictions from static moduli and from seismic tests. Seismic velocities are generally two or three times as large as velocities of large amplitude stress waves. Static moduli are about one-half the dynamic moduli; hence, predictions based on static moduli should be 30% low.

Use of the experimental and theoretical results for prediction of phenomena in full-scale field conditions should be made with caution. The present results were obtained in a one-dimensional (controlled lateral strain) condition and their applicability to more complex geometries is unknown. The wave durations involved in these tests are one-tenth to one-thousandth those found in the field, and the preloads and dynamic pressures were limited. Hence, the use of these results for prediction of full-scale phenomena would require considerable extrapolation.

2.2 Recommendations for Further Research. For DASA's purposes, i.e., for the design and analysis of shallow-buried underground protective structures, it is important to develop an understanding of wave propagation in soils under conditions which closely approximate those of the full-scale problem. Therefore, the present investigation should be extended in the following directions:

1. To depths of tens of meters below the surface of the ground.
2. To dynamic pressures of 70 bars (1000 psi) and positive pressure durations up to 1 second.
3. To soils which are compacted to densities as high as those obtained with modern highway compaction equipment (and thus comparable to well-consolidated soils and soils likely to be found in backfills over buried shelters).
4. To three dimensions.

Steps in each of these directions would provide significant improvements in our understanding of actual structural response which would be caused by a near-surface nuclear explosion.

From the researchers' point of view, the first three represent simply extrapolations on presently held information on the wave propagation problem. Work in these three directions will serve to confirm or improve and quantify the prediction procedure of Chapter 3. The step to three dimensions will necessarily involve the investigation of phenomena which differ considerably from the one-dimensional phenomena investigated herein. Some progress is now possible in each of these four directions.

To accomplish the extension in these directions we recommend:

1. One-Dimensional Wave Propagation Experiments. These tests should be similar to those reported herein with the following modifications. Loading with several decay rates should be used; in particular, a loading with no decay should be used to determine wave velocity through the soil, a rapid decay should be used to obtain a high attenuation, and a small decay should be used because that would be most like field conditions. Tests should be made at several preload levels, from zero to several bars, to simulate the overburden pressures felt by soils at various depths. The dynamic pressures used should be extended up to 70 bars to simulate likely structural design conditions. The soils used should represent a wide range of compactions and dissipative properties. The three soils treated in this report represent an adequate range of dissipative properties, but were only moderately compacted for the tests.

2. Improvement of Wave Propagation Test Equipment. The gages for measuring stress and the system for applying the loading should be improved for future tests. The gage design should be based on a force gage concept so that the total force travelling through the soil is measured. (Stress equals the force divided by the cross-sectional area of the column.) By using a force gage, one eliminates the problem of over or under-registration which is common with stress gages The gage calibration should be the same during loading and unloading so that the entire stress wave can be correctly recorded. The density and stiffness of the gage should be similar to those of the soil to minimize the disturbance caused by the presence of the gage. One gage design which appears to meet those requirements has been described in a proposal to DASA.*

* SRI Proposal PHU 65-192 submitted to DASA on October 11, 1965.

To best simulate blast pressures from nuclear weapons, the applied pressure history should have a shock front and a pressure decay thereafter. These conditions can be obtained in several types of shock tubes. With a shock tube, pressures up to 70 bars can be obtained and the pressure histories can be readily controlled and repeated.

3. Dynamic Compression Tests on Soil Samples. Laboratory compression tests should be performed to determine soil properties, and the effects of strain rate, stress level, and preload on those properties. To do this, the compression test program described in this report should be expanded to include pressure pulse rise times from 2 msec to 2 minutes. With such a program, a fairly complete picture of the effects of strain rate can be mapped out. Such tests should be conducted at several dynamic stress levels and several preloads.

4. Three-Dimensional Wave Propagation Study. Considerable progress can now be made toward solving the three-dimensional problem of blast loading on soil in which there are buried structures. The following steps should be taken:
   a. Analysis of the response of an elastic half-space to a blast loading on its surface.
   b. Development of experimental techniques to measure the response of an elastic model of a half-space to a simulated blast loading. The model response should be compared with the analytical results to evaluate the validity of the experiments.
   c. Conduct of experiments in an elastic half-space model in which small structures have been embedded. The testing techniques of step b should be used.
   d. Conduct of experiments in a half-space of dissipative material (with dissipation properties like those of soils) in which structures have been embedded.

CHAPTER 3

PREDICTION PROCEDURE

The procedure for prediction of stress wave propagation phenomena in soils is neither complete nor verified. Some of the details of the procedure seem quite clear now, others are almost pure speculation. By outlining it here, we simply indicate the direction which has been taken toward understanding the phenomena. The experimental findings of Chapter 4 are used to indicate the level of accuracy expected in the parts of the prediction. The prediction procedure is strictly applicable to one-dimensional phenomena only, although some of the concepts may be useful in studying more complex geometries. The test results, on which the procedure is based, were limited to wave durations of several milliseconds, dynamic stress levels of 11 bars or less and preload levels up to 0.7 bars. Extrapolations of these results to much longer durations or higher stresses should be made with caution.

A prediction procedure requires knowledge of the soil for which the prediction is to be made. With qualitative knowledge we decide which soil model parameters are paramount. Quantitative knowledge of the pertinent values of these parameters must then be found from laboratory tests.

The prediction should be made on the basis of average soil properties for the depths and stress levels that pertain to a particular problem. The theoretical models used for the prediction are characterized by a wave velocity and one or two dissipation parameters. The models describe the soil as compacting (showing a residual strain after a loading cycle), strain-rate-dependent (viscoelastic), or both viscoelastic and compacting. When we have chosen one of these models the qualitative nature of the soil has been decided. The experiments described in Chapter 4 show that the constant tan delta model (purely

viscoelastic dissipation) is the best choice for the clay soils but that the viscoelastic compacting model (both types of dissipation) is best for sand.

Next, tests are performed to find the magnitude of the parameters in the theoretical models. These parameters can be found from dynamic compression tests on thin samples of the soil. The stress on the soil and the strain of the sample must be recorded during the test. The equipment and procedure for performing the test are given in Appendix B. A modulus for the soil can be found from the slope of the stress-strain relation at the stress level of interest. The amount of time the peak strain lags behind the peak stress is used to determine the viscoelastic properties. The slope of the unloading stress-strain curve is compared to the loading slope to determine the compacting parameter. These data reduction procedures are given in Appendix B.

After the theoretical model has been specified quantitatively, the model can be analyzed for its behavior during wave propagation. Then the analytical behavior can be used to predict the corresponding response of the soil. For simple models, the analysis can be done once and graphed. This is the case for the constant tan delta and linear hysteretic models for which attenuation curves are given in Figs. 3.1 and 3.2. The prediction of the linear hysteretic model gives the same attenuation for stress and particle velocity. For the constant tan delta model, the stress and particle velocity attenuations are nearly the same (as noted in Ref. 3). In a given situation, it is expected that the applied stress wave form would be known so that a knowledge of the amount by which stress attenuates with depth (such as in Figs. 3.1 and 3.2) is all that is required for the prediction of stress attenuation. For the prediction of particle velocity attenuation, the particle velocity at the surface must be determined first. This peak value is calculated from

$$v_{mo} = \frac{\sigma_{mo}}{\rho c_o} \tag{3.1}$$

where σ_{mo} is the peak applied stress,

ρ is the material density, and

c_0 is the wave velocity corresponding to σ_{mo} at the surface (found from the tangent modulus).

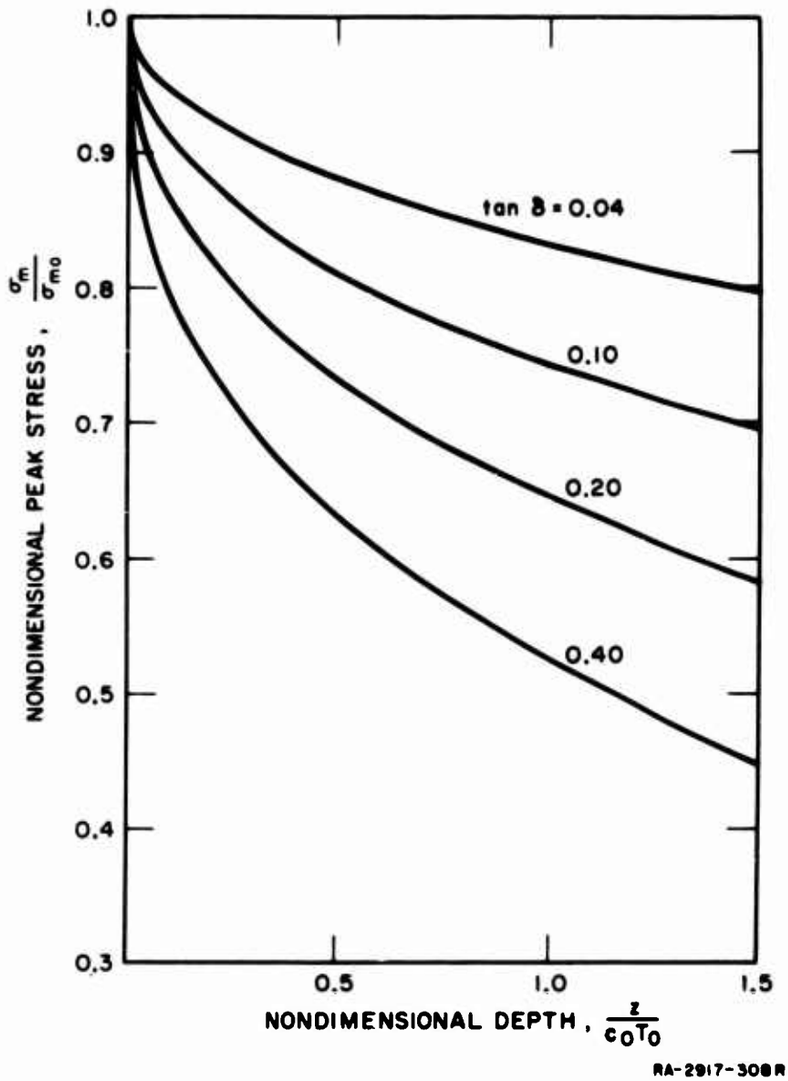

FIG. 3.1 STRESS ATTENUATION PREDICTION FROM THE CONSTANT TAN DELTA MODEL

Attenuation equation

$$\sigma_m/\sigma_{m0} = (1 - 0.15 \tan \delta)\, e^{-7/8 \sqrt{(z/c_0 T_0) \tan \delta}}$$

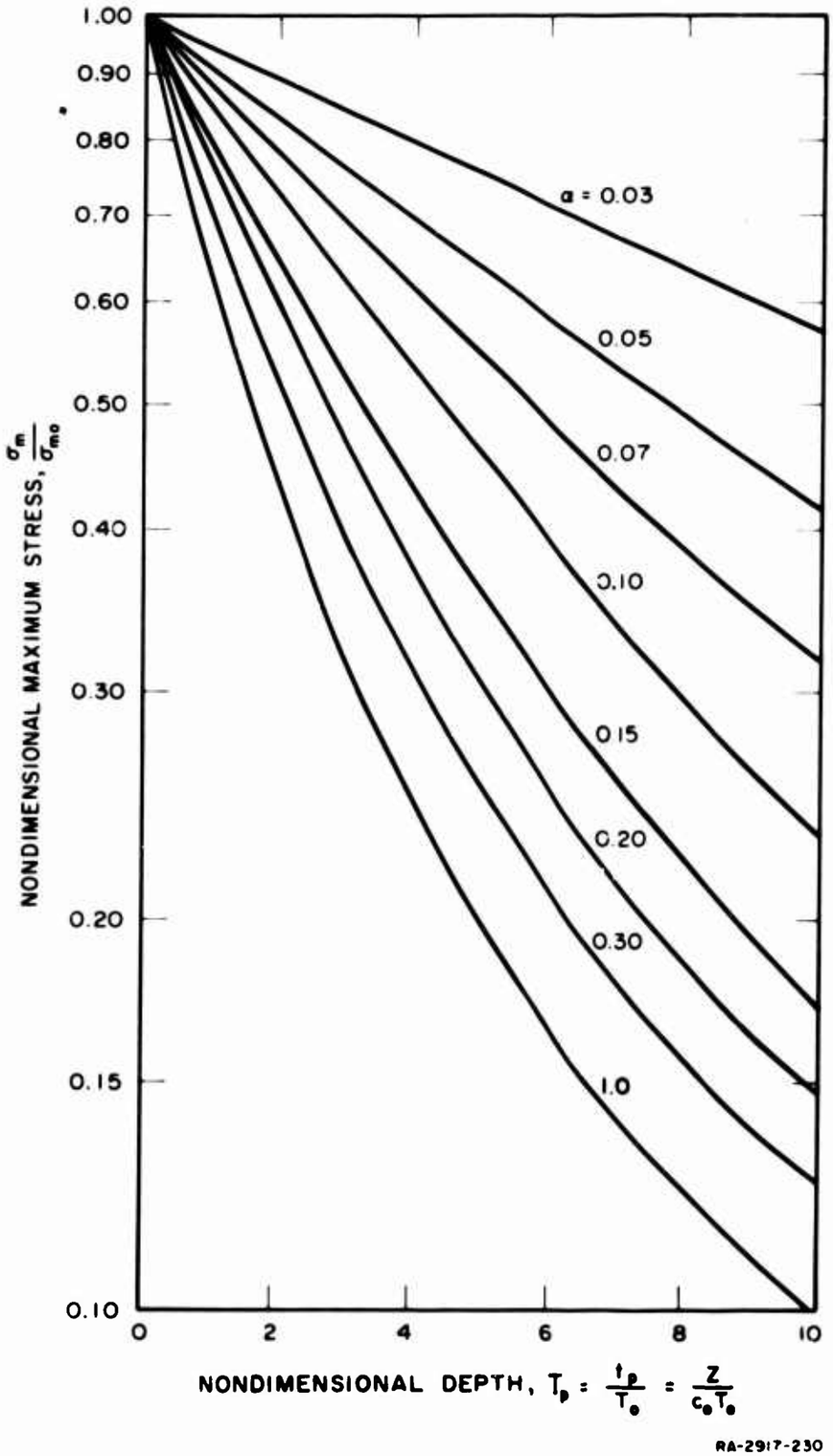

FIG. 3.2 STRESS ATTENUATION PREDICTION FROM THE LINEAR HYSTERETIC MODEL

Curves from Eq. C.22

The experimental stress attenuation and particle velocity attenuation are not well represented by the theoretical predictions of any of the models. The constant tan delta model appears to represent the results for clay best; however, the experimental points are as much as 50% above or below the prediction. The peak particle velocity was obtained within 5 or 10% from Eq. 3.1 for the clay and with less accuracy for the sand. The attenuation predictions for particle velocity were no more accurate than those for stress.

The duration and rise time of the stress wave may also be predicted from the theoretical models. However, neither the duration nor rise time have been adequately predicted by the linear hysteretic model. The complete wave form from the other models has not been studied so no prediction is available from them.

The wave velocity is taken directly from the tangent modulus from the compression test data and is not modified by the models. Based on this wave velocity, an arrival time at the base was predicted. The predicted times for the clay columns were within 10% of the experimental values; the predicted time was 25% short for the sand.

BLANK PAGE

CHAPTER 4

WAVE PROPAGATION EXPERIMENTAL RESULTS AND DISCUSSION

4.1 Introduction

Wave propagation experiments were conducted in three soils to determine the general nature of the phenomena involved and also to accumulate data with which to evaluate the predictions obtained from theoretical soil models. In this chapter, we show

1. the principal features of wave propagation in the soils,
2. the degree to which these features can be predicted theoretically, and
3. the features that do not correspond to the theoretical predictions.

As a preparation for the wave propagation results, the test conditions are first outlined, and then the main test results are given. Further information on test apparatus, gages, and calibration procedures are given in Appendix A.

4.2 Test Conditions

The test facility consisted of a soil tube and its support structure. The soil tube, shown in Fig. 4.1, was constructed of alternate rings of aluminum and neoprene rubber. The aluminum rings provided a high radial stiffness to prevent radial motion of the soil, and the rubber spacers reduced the axial stiffness of the tube. Thus, the tube was intended to allow only one-dimensional (axial) motion in the soil. Further information on the stiffness of the tube and on the degree to which it required one-dimensional motion in the soil is given in Ref. 3 and 4.

The tube was made up in segments, each about 0.7 meters long (see Fig. 4.1). In Fig. 4.2, the column is shown at full height of 4.5 meters (seven segments), with its associated support structure.

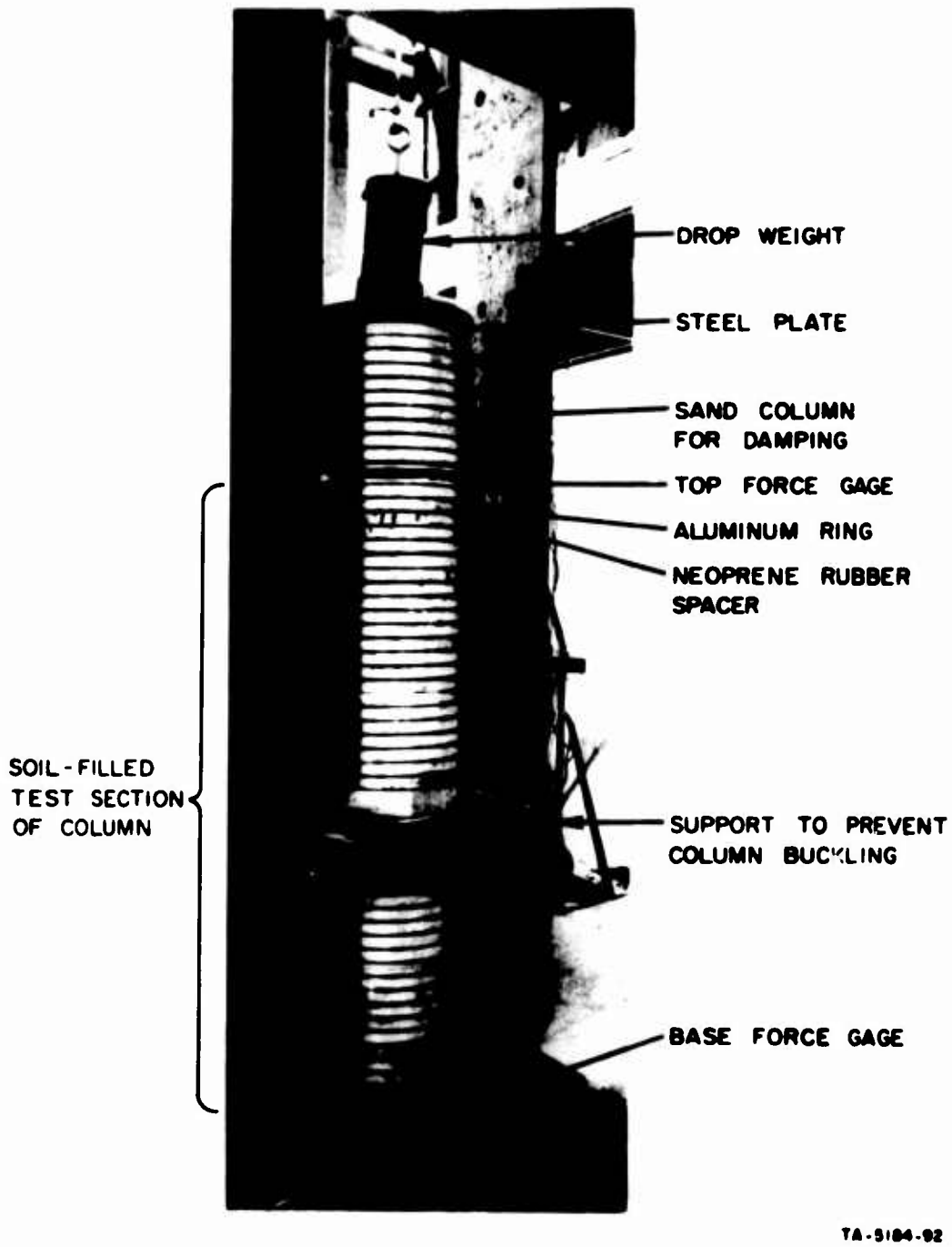

FIG. 4.1 TWO SEGMENTS OF SOIL TUBE IN TEST CONFIGURATION

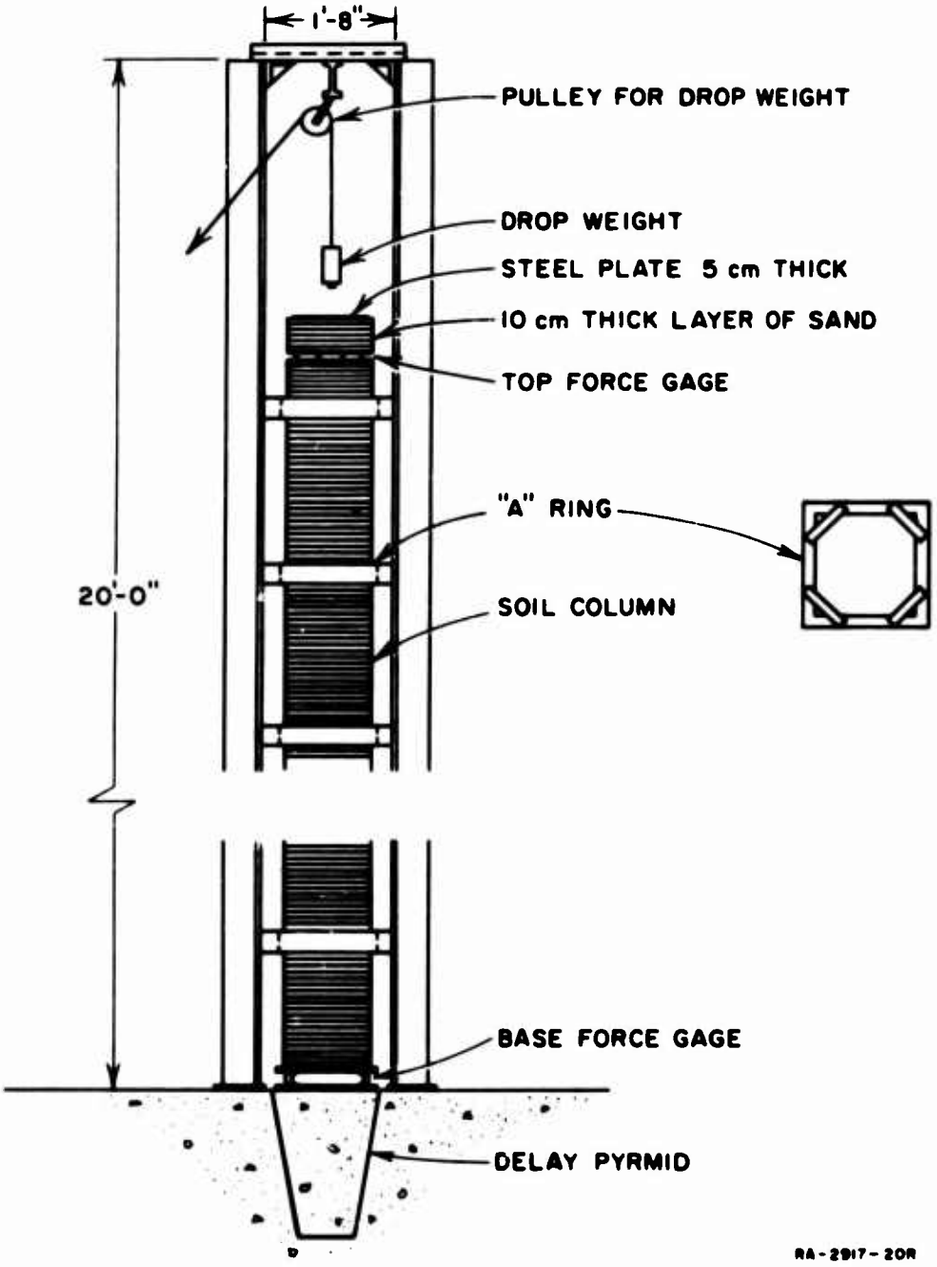

FIG. 4.2 SOIL COLUMN SUPPORT STRUCTURE

The drop weight mechanism (Fig. 4.2) was used to apply a large stress for a short duration on the top of the column. The stress waves closely resemble those from blasts: rise time of 0.2 to 1.0 msec to a peak and then an approximately exponential decay with an exponential time constant of 2 to 6 msec. In most of the tests, the weight, a steel cylinder with a steel ball at the base for a striker, was dropped onto a 5-cm-thick steel plate resting on the soil column. Immediately below the plate was a 10-cm-thick layer of dry sand to damp out ringing produced by the impact. Below the sand was the top force gage and then below that the soil being tested. For some of the tests on wet kaolinite, the weight was equipped with a large striking plate (see Fig. A.7) and was dropped directly onto the damping sand.

Measurements of the soil stress and motion during wave propagation was obtained from stress gages and accelerometers embedded in the soil and from force gages at both ends of the column. The sensing element was either a piezoelectric crystal or a strain gage bridge. In either case, the response of the gage was fed to oscilloscopes and recorded with oscilloscope cameras. Characteristics of the gages and the calibration procedures for the stress and force gages are detailed in Appendix A. A typical layout of the column and gage is shown in Fig 4.3.

Three soils, exemplifying a wide range of properties, were used in the tests: a Monterey beach sand, a kaolinite, and Vicksburg back-swamp clay. The sand was composed of clear, dry, subangular particles of nearly uniform size. The kaolinite was purchased as a white powder and was reconstituted with water to form a soil. The Vicksburg back-swamp clay is a natural soil that was mixed with water to obtain a desired consistency. These three soils ranged from dry to very wet, hence bracketing the variation of water contents of soils used for construction. The tangent modulus of the soils at a stress level of 6 bars varied from 750 bars to 4800 bars. This range is common to soils found near the surface of the earth but not to soils which have been highly-compacted, hardened by drying, or consolidated under a high overburden pressure.

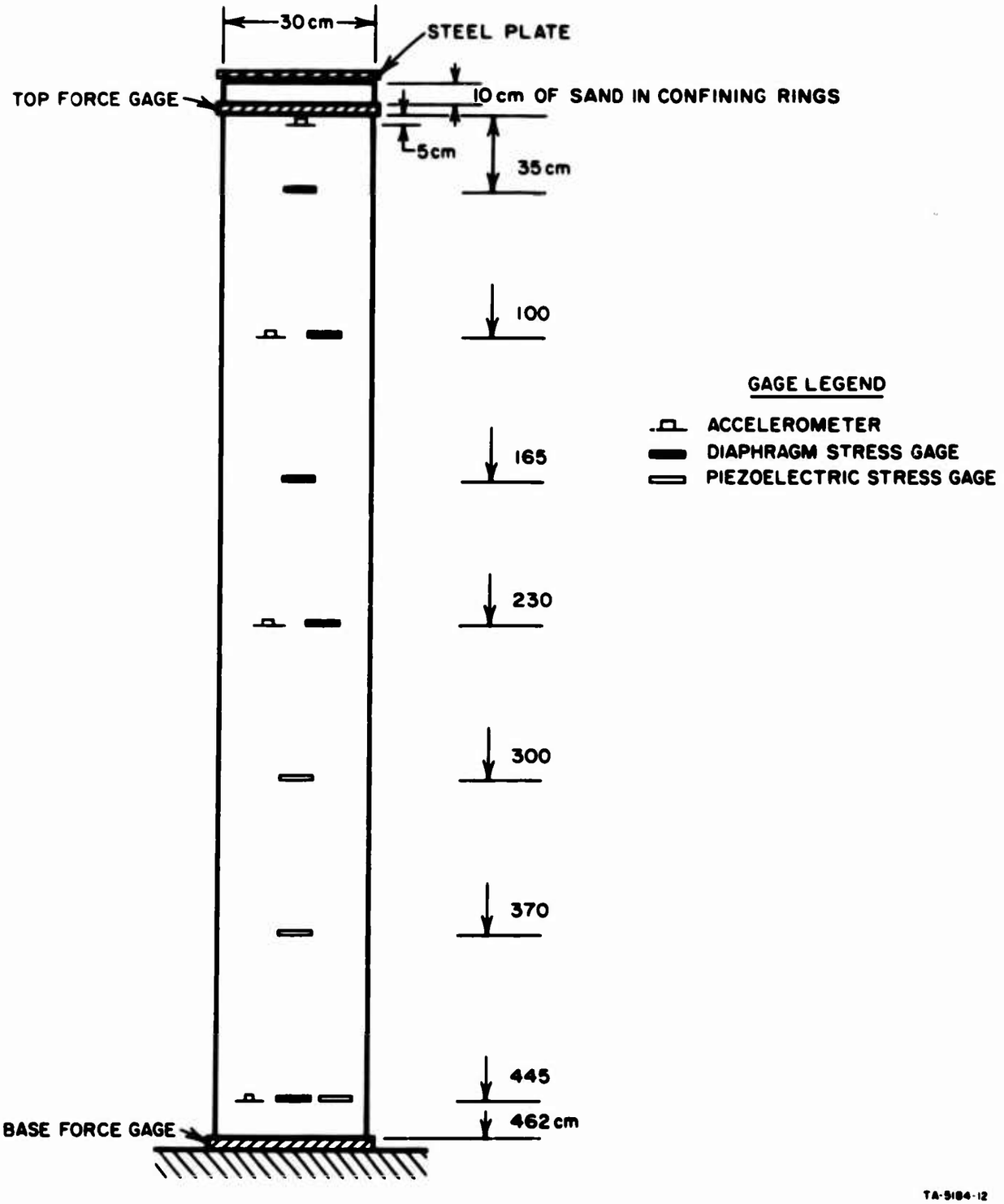

FIG. 4.3 TYPICAL SOIL COLUMN AND GAGE CONFIGURATION

The soil tube was filled six times for the wave propagation tests. The soils used for each column and information about the placement of the soil are given in Table 4.1. Further data on the soils placed in each column are given in Appendices A and B.

TABLE 4.1

SOILS TESTED

Column Designation	Soil Name	Compaction Method	Water Content (%)	Dry[a] Density (gm/cm^3)	Comments
A	Kaolinite	Hand Tamping	34.7	1.29	Wet, very compressible
B	Kaolinite	Hand Tamping	31.7	1.34	Wet, compressible
C	Kaolinite	Static Pressure	18.8	1.42	Dry, granular appearance
D	Vicksburg Clay	Pneumatic Tamper	26.8	1.34	Sticky; nonuniform moisture content
E	Monterey Sand	Sprinkling	-	1.63	Dense
F	Vicksburg Clay	Static Pressure	24.4	1.52	Near optimum[b] moisture content

[a] Dry density is the weight of solids divided by the volume.

[b] Optimum moisture content is content at which maximum dry density (maximum compaction) can be obtained with a given compaction technique. The compaction method used as a reference here is the Standard Proctor.

4.3 Results

When an impulse is applied to the top of a column of soil, a stress wave propagates down the column. Typical stress records obtained at various points along the column are shown in Fig. 4.4. At the top, the stress wave shape shows the manner in which it was formed--by impact of a dropped weight on a steel plate. Hence, the wave has a rise time of a few tenths millisecond and may indicate some oscillations caused by ringing in the steel plate. As the wave progresses down the column, the oscillations damp out, and the rise time and duration of the wave increase.

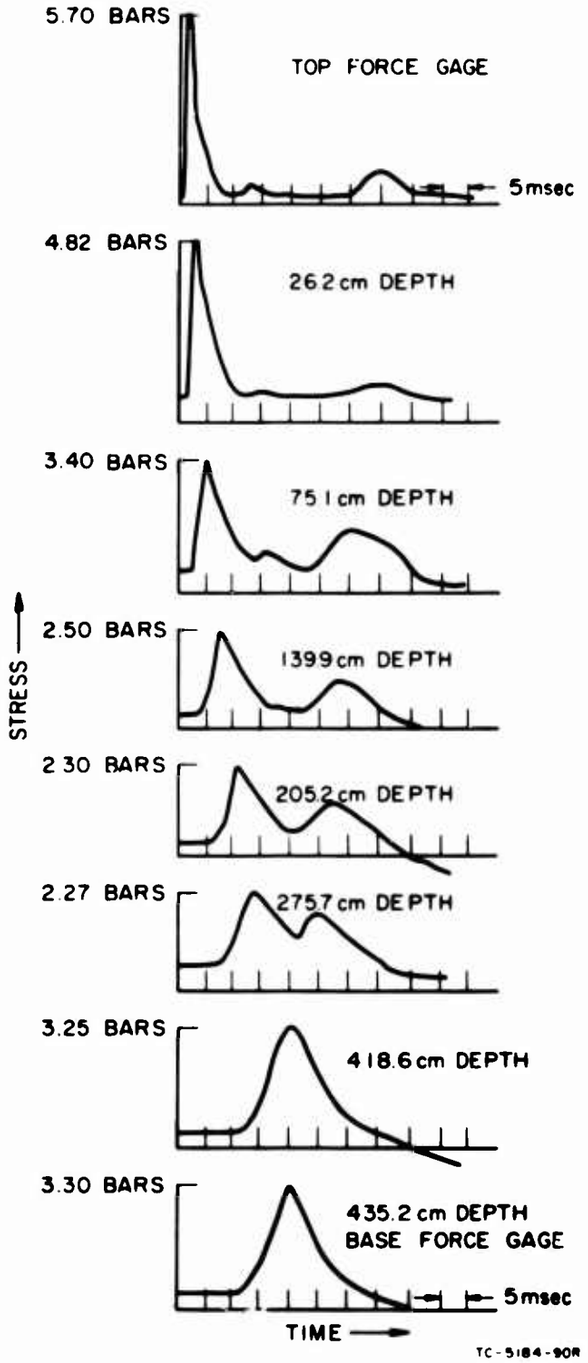

FIG. 4.4 STRESS RECORDS FROM A TEST ON COLUMN C

Test 6 on Dry Kaolinite, Drop Height of 100 cm

The records indicate that the wave changes shape as it progresses down the column. At the base there is a reflection that doubles or triples the magnitude of the wave: therefore, some care must be taken to distinguish the features belonging to the initial wave from those that accompany the reflected wave. As the initial wave travels down the column, its peak is reduced and its duration increased. An idealized form of the stress wave is shown in Fig. 4.5. It has a rapid rise to a sharply defined peak stress and then an exponential decay. The time, T, required for the stress to reduce to .368 times its peak value is the exponential decay constant for the idealized stress wave. This idealized stress wave is the general form assumed in both the data reduction and the computation with the theoretical soil models.

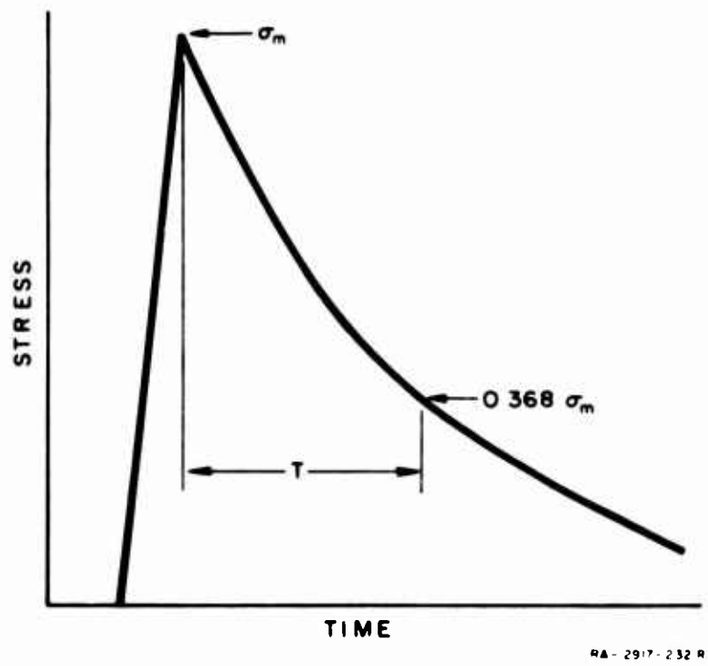

FIG. 4.5 IDEALIZED STRESS WAVE

Associated with the stress wave are the particle accelerations and velocities--the motions of the soil caused by the stress. Examples of acceleration records are shown in Fig. 4.6. The general shape of the acceleration wave does not change much, but the peak is drastically reduced and the duration is greatly increased. Accelerations were not

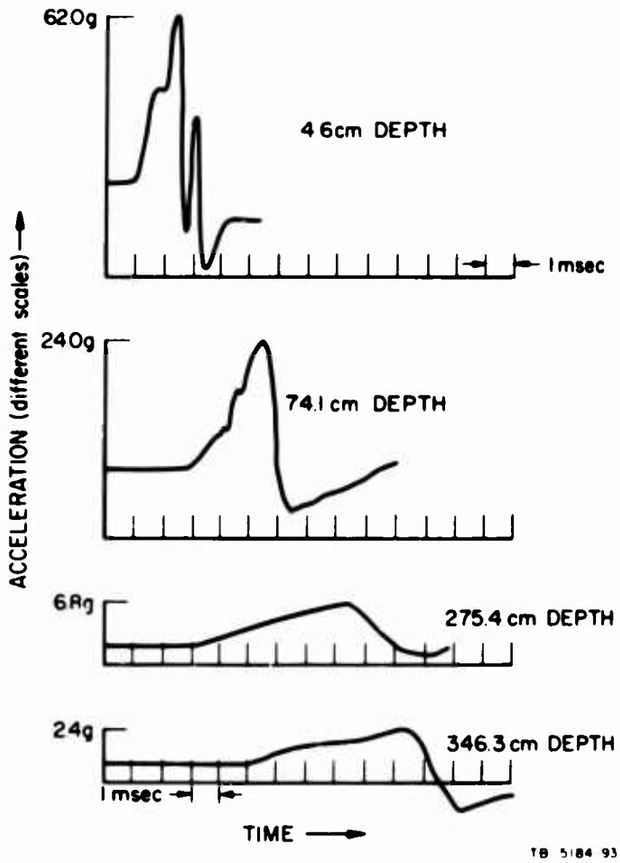

FIG. 4.6 ACCELERATION RECORDS FROM A TEST ON COLUMN C

Test 24 on Dry Kaolinite, Drop Height of 30 cm

considered in the theoretical predictions and no standard form for the acceleration wave was adopted. Particle velocity records were obtained from the acceleration by graphical or electronic integration with respect to time. The particle velocity wave form is almost identical to that of the initial stress wave.

The features of the stress and acceleration waves that were considered are:

1. attenuation of the peak stress with depth,
2. change in the duration of the stress wave with depth,
3. variation of the wave velocity with depth,
4. attenuation of peak acceleration with depth, and
5. attenuation of peak particle velocity with depth.

For attenuation of peak stress and particle velocity, variation of wave velocity, and the change in duration we have made theoretic predictions. The predictions are from the linear hysteretic model, visc compacting model, and the constant tan delta model. These three repre nt different types of energy dissipating mechanisms. The linear hysteretic model shows dissipation by a frictional mechanism. The dissipation parameter is α, which ranges from 0 for no dissipation to 1.0 at maximum dissipation. For the tested soils, the maximum α is 0.15 (Appendix B). In the constant tan delta model, the dissipation is viscous, and the phase lag between stress and strain is the same at all frequencies. Tan δ, the dissipation parameter, ranges from 0.1 to 0.3 for the tested soils; it is a measure of the phase lag between stress and strain that occurs under cyclic loading. The viscoelastic compacting model combines viscous and frictional types of dissipation. The dissipative parameters are α, as with the linear hysteretic model, and τ/E_0, a measure of the lag time between stress and strain. For our soils, τ/E_0 varies between 20 and 30 msec. The first two of these models were analyzed in Ref. 3 and the third is treated in Appendix C of the report. The methods for obtaining the soil properties used with these models are described in Appendix B.

Six complete columns were constructed using the three soils (see Table 4.1). For convenience in comparing the results from the tests,

the results for each wave propagation feature are grouped together. That is, first the stress attenuation curves from all the tests are given, then the wave durations, etc. The sequence is A, B, C, D, F, and E so that the three tests of kaolinite (A, B, and C) and the two of Vicksburg backswamp clay (D and F) are together.

Stress attenuation data from the tests are summarized in Figs. 4.7 to 4.13. In most cases, there is considerable scatter in the data. To some extent this is caused by unreliability of the stress gage calibrations. However, much of the apparent variability in the data is caused by changes in the conditions from test to test. Each graph shows points from tests in which there were several stress levels, durations, and even different wave velocities. The prediction curves on each figure are based on average values of the stress and duration and on predicted wave velocities obtained from the modulus of the soil (Appendix B).

The limited number of points from Column A appear to follow the prediction of the constant tan delta model reasonably well (Fig. 4.7). For Column B there are two figures, one for the tests in which the drop-weight impacted the sand above the force gage directly (Fig. 4.8) and one for the usual configuration with a steel plate atop the column (Fig. 4.9). The importance of drop height (and, therefore, of stress level) on attenuation is particularly noticeable in Fig. 4.9. For both groups of tests on Column B, the best prediction is from the constant tan delta model.

The first reasonably consistent data appear in Fig. 4.10 and was obtained from the well-compacted clay of Column C. All the theoretical predictions are in the vicinity of the data, but the constant tan delta model appears to represent the trend of the data best. The stress values at the depth of 4.35 meters are from the base force gage. This gage registered the sum of the initial stress wave and the wave reflected from the base. To obtain a value for the stress in the initial wave, the peak value was divided by the ratio of the impulse at the base to the impulse at the top. This value of the stress in the initial wave is represented by the points at 4.35 meters. This procedure for getting a peak stress at the base for the initial stress wave was used for Columns C through F, and it is further explained in Appendix A.

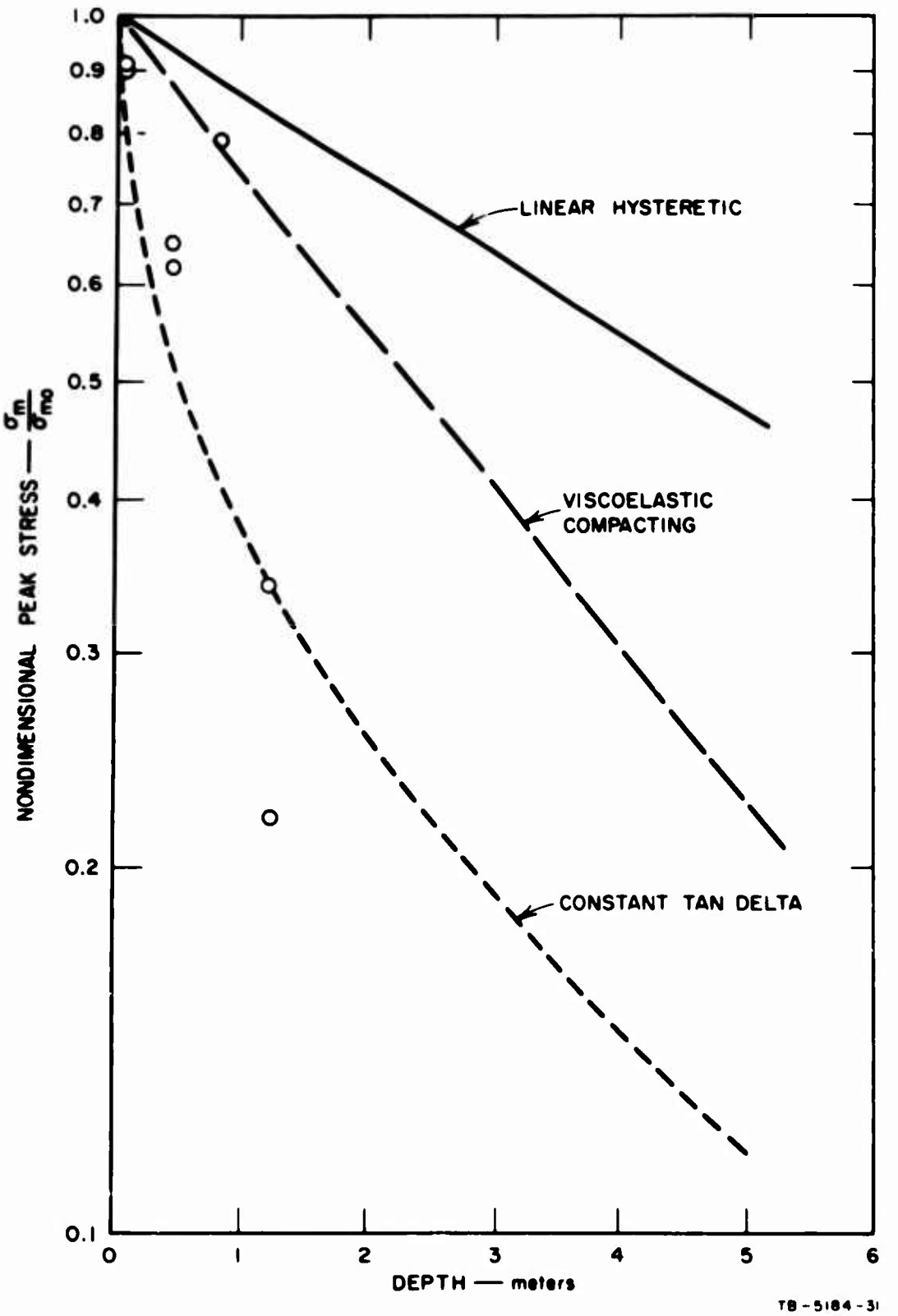

FIG. 4.7 STRESS ATTENUATION: COLUMN A, KAOLINITE

Curve Parameters
Linear Hysteretic: $\alpha = 0.02$
Viscoelastic Compacting: $\alpha = 0.02$, $E_1/E_0 = 2.0$, $\eta/E_0 = 30$ msec
Constant Tan Delta: $\tan \delta = 0.30$
c = 100 m/sec for all models.

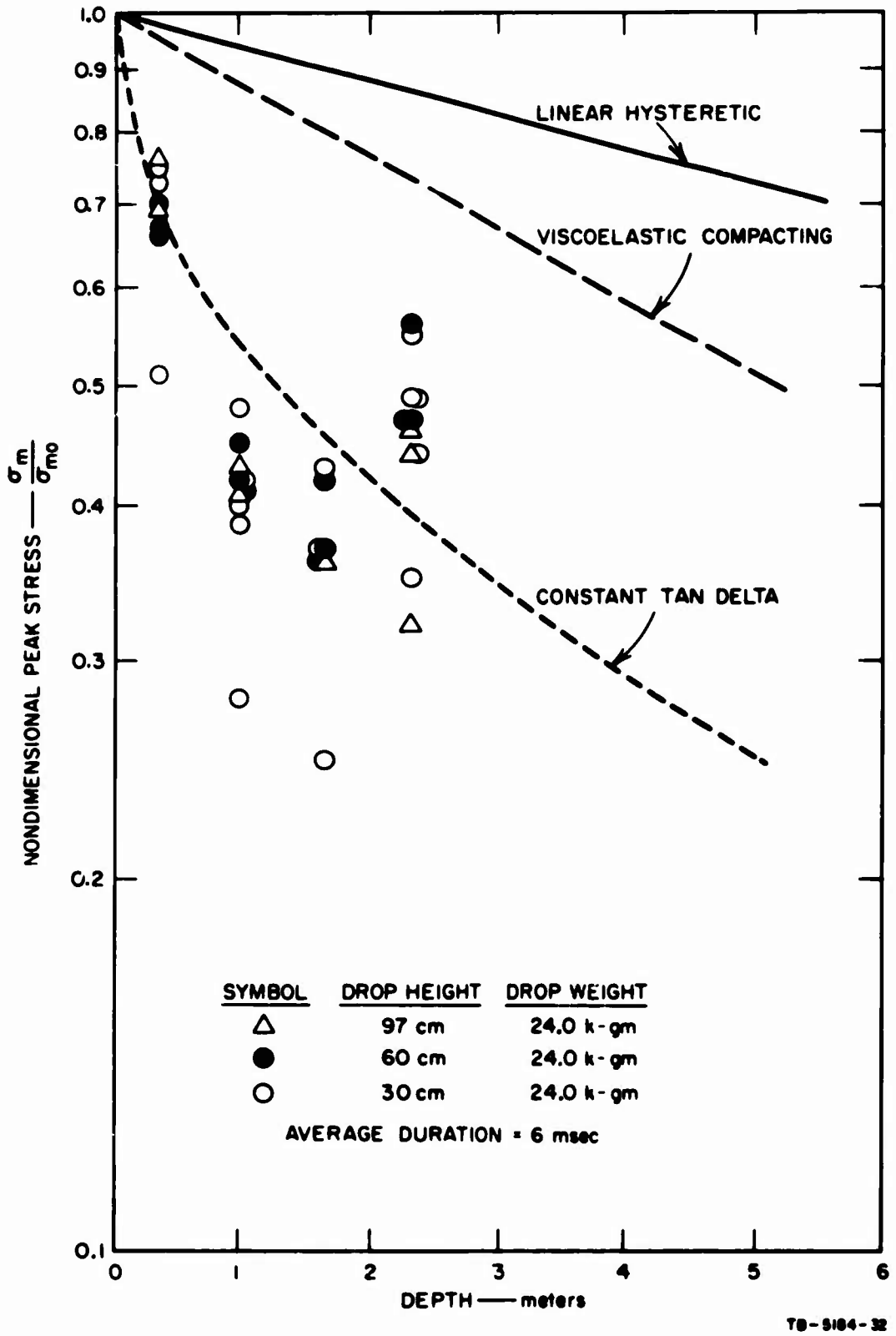

FIG. 4.8 STRESS ATTENUATION: COLUMN B, KAOLINITE (T_o = 6 msec)

Curve Parameters
Linear Hysteretic: α = 0.02
Viscoelastic Compacting: α = 0.02, E_1/E_0 = 2.0, η/E_0 = 30 msec
Constant Tan Delta: tan δ = 0.30
c = 100 m/sec, T_0 = 6 msec for all models.

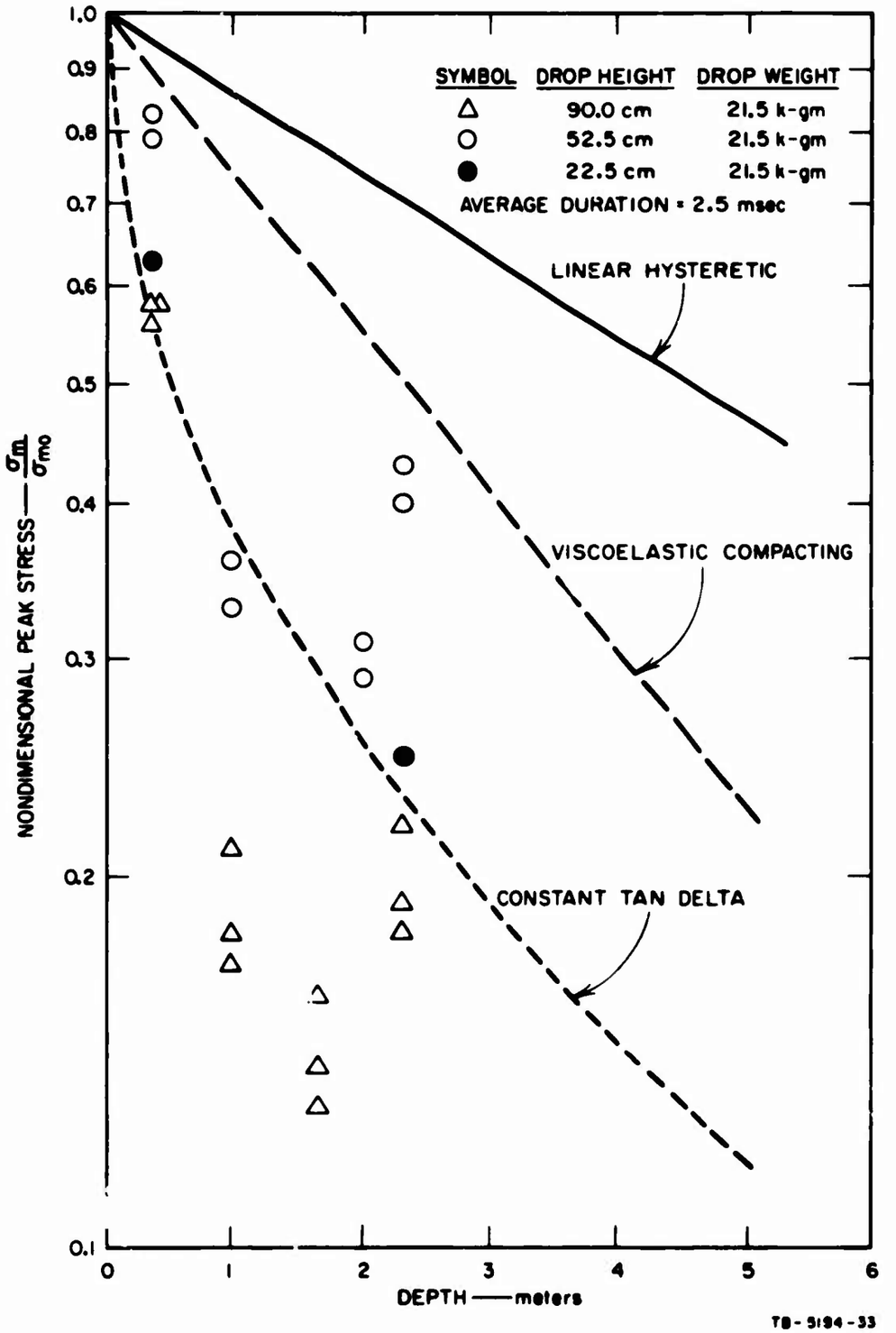

FIG. 4.9 STRESS ATTENUATION: COLUMN B, KAOLINITE (T_o = 2.5 msec)

Curve Parameters
Linear Hysteretic: α = 0.02
Viscoelastic Compacting: α = 0.02, E_1/E_0 = 2.0, η/E_0 = 30 msec
Constant Tan Delta: tan δ = 0.30
c = 100 m/sec, T_0 = 2.5 msec for all models.

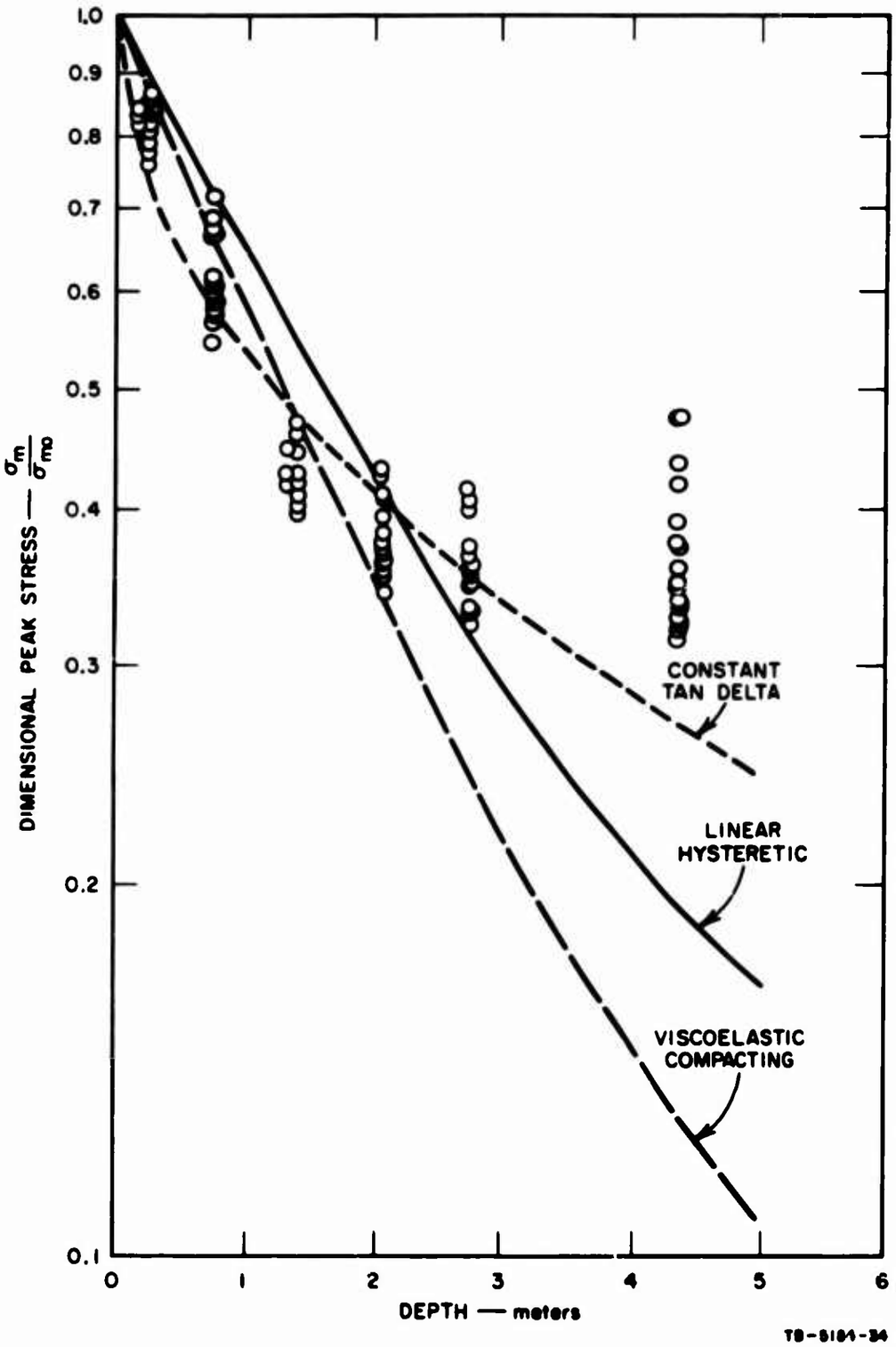

FIG. 4.10 STRESS ATTENUATION: COLUMN C, KAOLINITE

Curve Parameters
Linear Hysteretic: $\alpha = 0.15$
Viscoelastic Compacting: $\alpha = 0.15$, $E_1/E_0 = 2.0$, $\eta/E_0 = 15$ msec
Constant Tan Delta: $\tan \delta = 0.30$
$c = 240$ m/sec for all models.

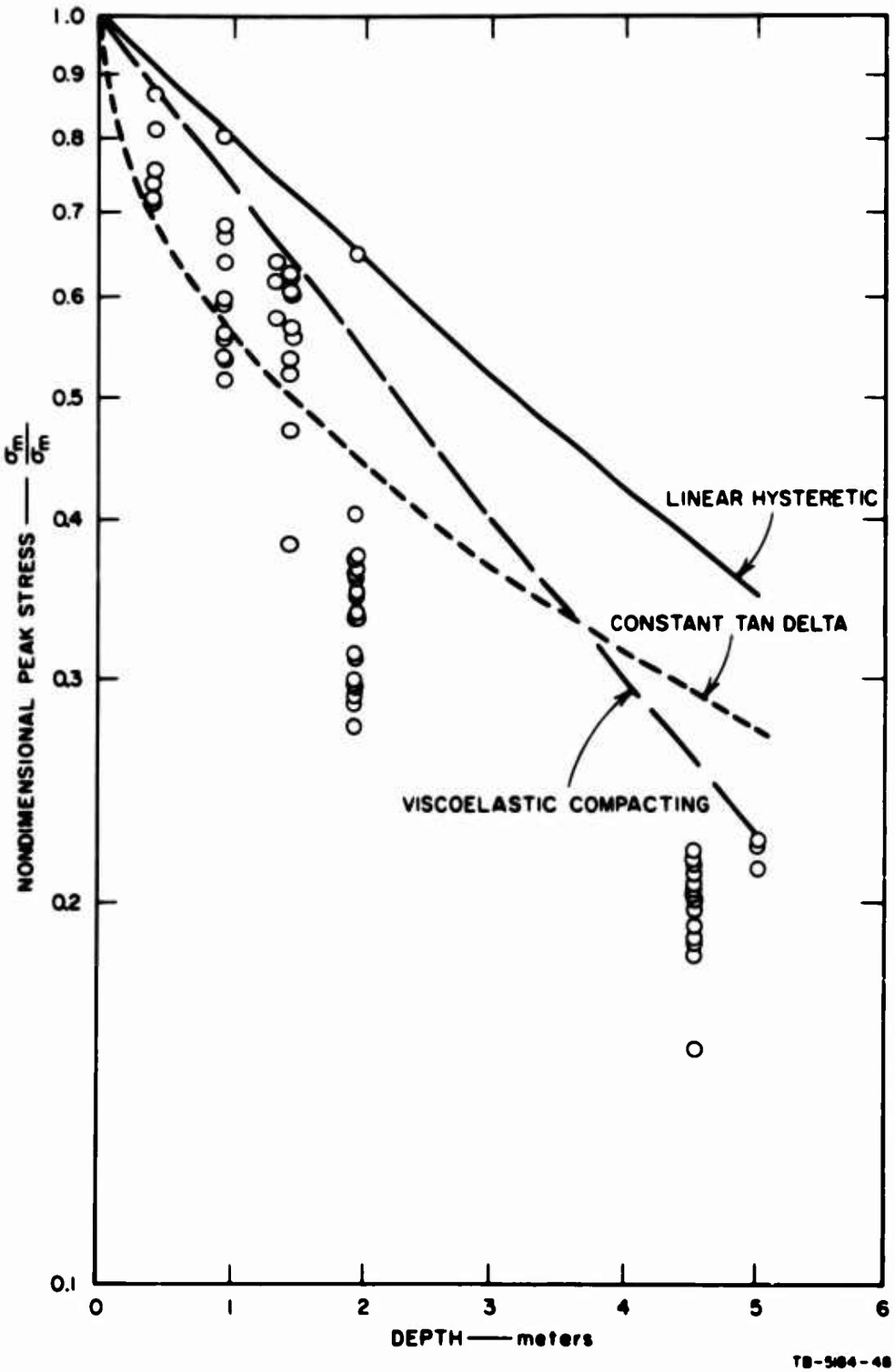

FIG. 4.11 STRESS ATTENUATION: COLUMN D, VICKSBURG CLAY

Curve Parameters
Linear Hysteretic: $\alpha = 0.09$
Viscoelastic Compacting: $\alpha = 0.09$, $E_1/E_0 = 1.7$, $\eta/E_0 = 20$ msec
Constant Tan Delta: $\tan \delta = 0.30$
$c = 340$ m/sec for all models.

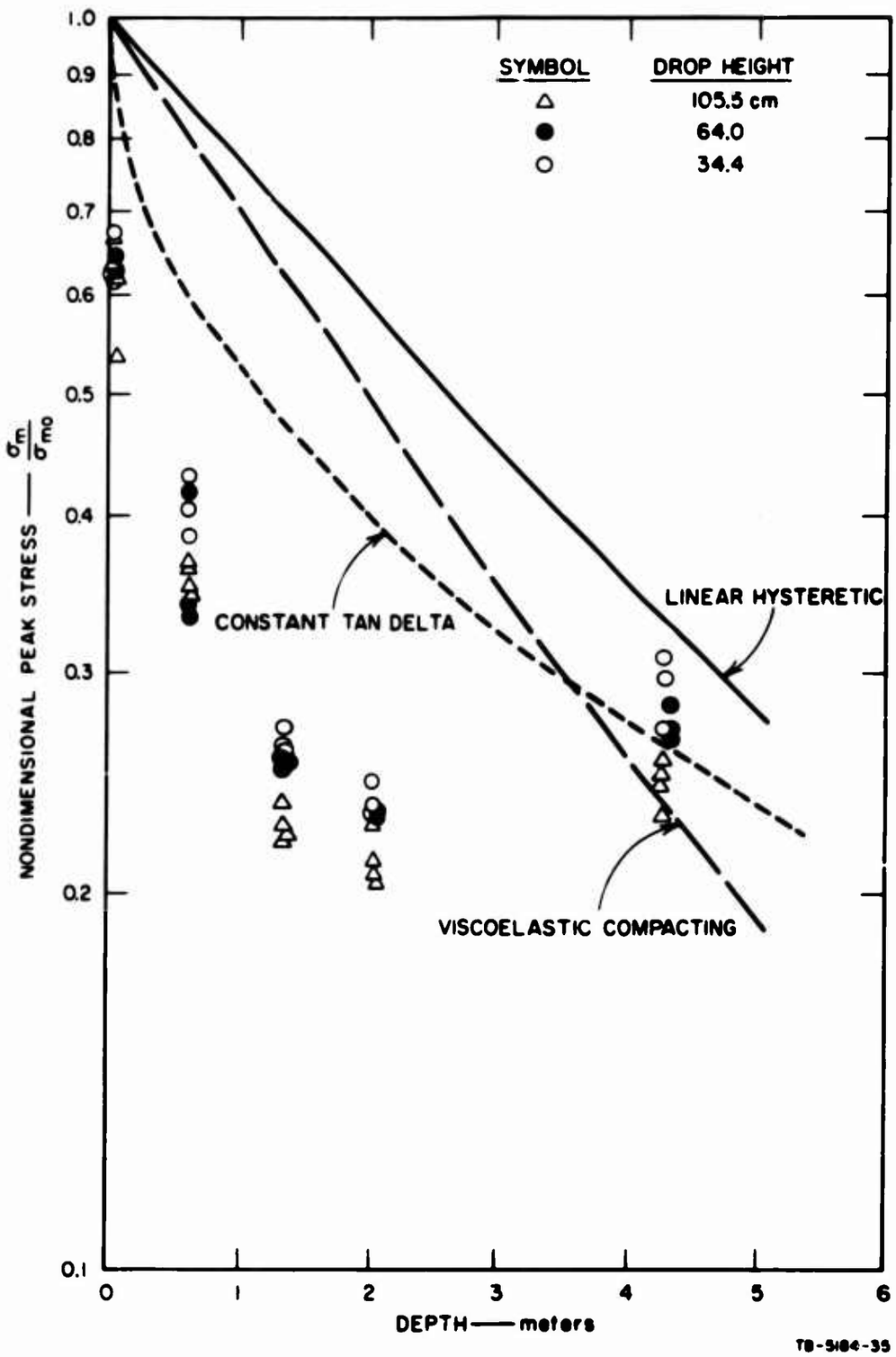

FIG. 4.12 STRESS ATTENUATION: COLUMN F, VICKSBURG CLAY

Curve Parameters
Linear Hysteretic: $\alpha = 0.09$
Viscoelastic Compacting: $\alpha = 0.09$, $E_1/E_0 = 1.7$, $\eta/E_0 = 20$ msec
Constant Tan Delta: $\tan\delta = 0.30$
$c = 340$ m/sec for all models.

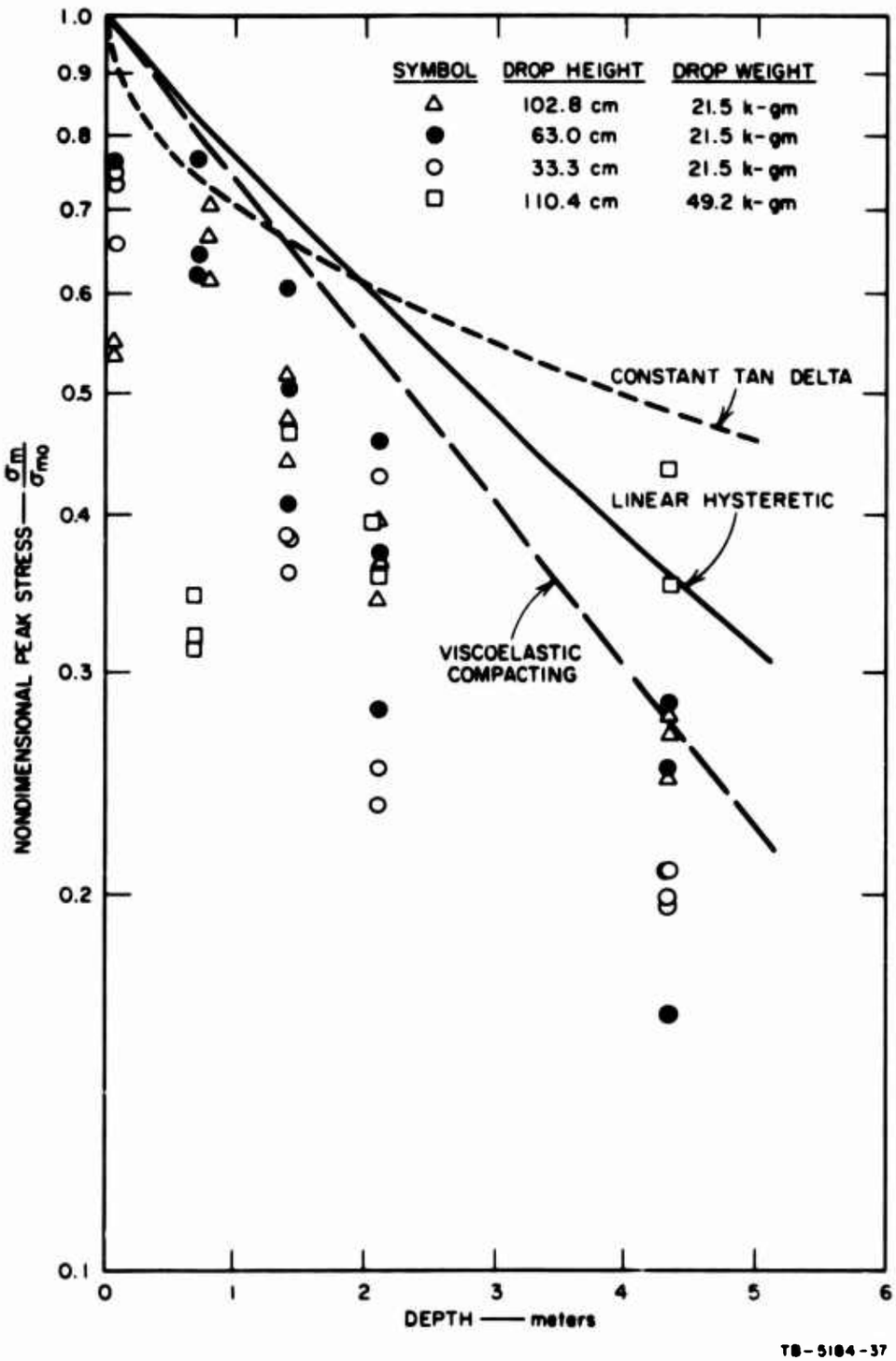

FIG. 4.13 STRESS ATTENUATION: COLUMN E, MONTEREY SAND

Curve Parameters
Linear Hysteretic: $\alpha = 0.12$
Viscoelastic Compacting: $\alpha = 0.12$, $E_1/E_0 = 5.0$, $\eta/E_0 = 22$ msec
Constant Tan Delta: $\tan\delta = 0.12$
$c = 500$ m/sec for all models.

The somewhat loose soil of Column D showed a faster attenuation of stress than predicted (Fig. 4.11). The form of the attenuation is similar to the curve from the viscoelastic compacting model but not unlike that from the constant tan delta model. For Column F (Fig. 4.12), the stress attenuation was also faster than predicted. Here, the form of the experimental attenuation curve is similar to that from the constant tan delta model. For Column F the data at 4.25 meters are definitely out of line with the other data. This same discontinuity occurs in the other figures but is less noticeable. This discontinuity is probably caused by difference in the reduction system used for the base force gage and the other gages (stress gages). The data points at the column base as well as those at the top were obtained from force gages, the intermediate points from stress gages. The stress gage data were based strictly on static calibrations. The force gage data were based on both static calibrations and the impulse ratio mentioned above. No conclusions have been reached as to which groups of data may be more reliable.

The large scatter of data in Fig. 4.13 is at least partially due to the range in stress levels and durations. Both of these factors vary with drop height. Prediction curves based on the average values of the parameters indicate that the viscoelastic compacting model is the best approximation for the sand. This result contrasts with the conclusion in Reference 4 that the attenuation in sand was well represented by the linear hysteretic model. The present experimental results were similar to those from Reference 4 but the procedure for evaluating the dissipation parameter α had changed. The parameter α is a function of the slopes of the loading and unloading stress-strain curves obtained in a compression test on the soil. In Reference 4 these slopes were measured on static stress-strain curves at a point "near" the peak stress of the compression test. This evaluation has the disadvantage of being based on static tests and of depending on the choice of a point for making the evaluation. The present values of α were derived from an analysis in which the slopes at midheight of the stress-strain curves were used. This analysis (see Appendix C) also takes into account the time-dependent nature of the soil.

The next feature to be considered is the duration of the stress wave. As the peak attenuates, the duration increases. The time between the arrival of the peak and the time at which the stress has decayed to 0.368 of the peak has been taken as the duration of the wave. The non-dimensional duration (duration divided by the duration of the applied stress) is shown in Figs. 4.14 to 4.18 for Columns B through F. The arrival of the wave reflected from the base made it impossible to determine a duration for the stresses in Column A.

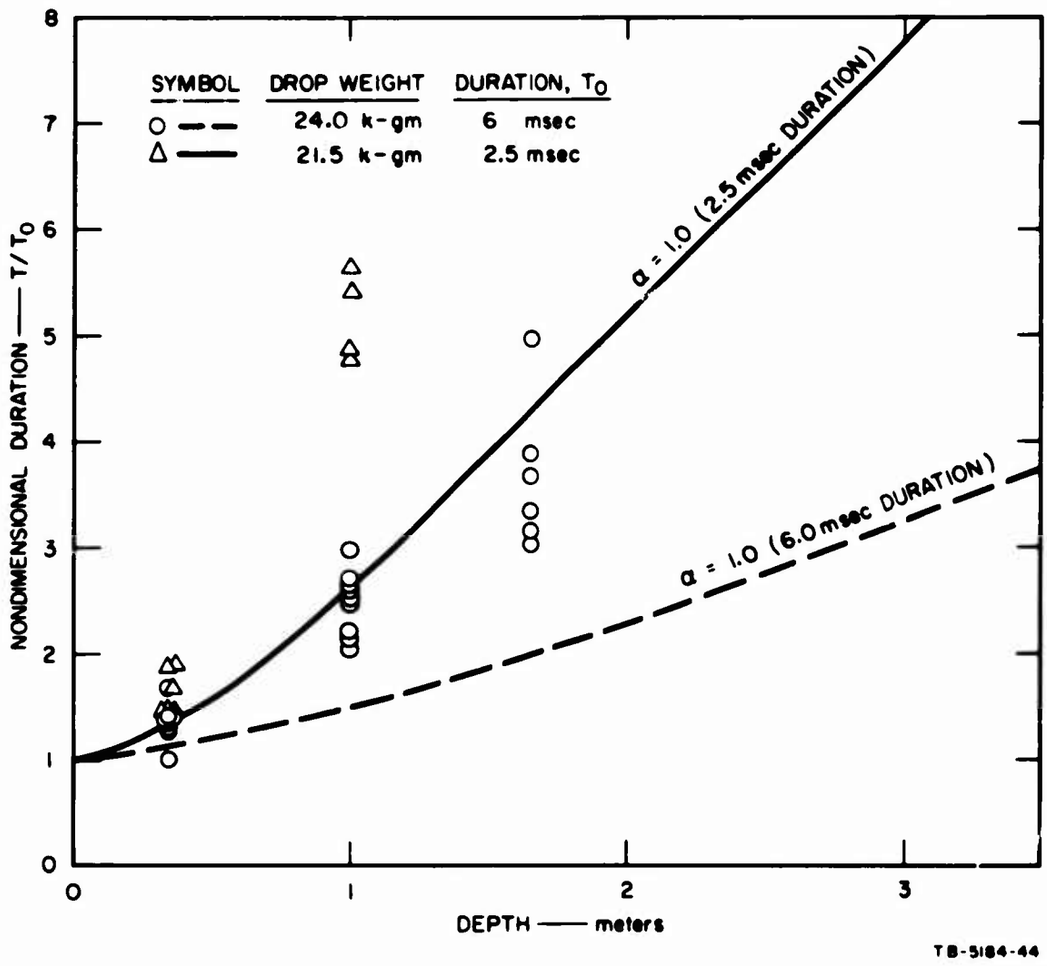

FIG. 4.14 STRESS WAVE DURATION: COLUMN B, KAOLINITE

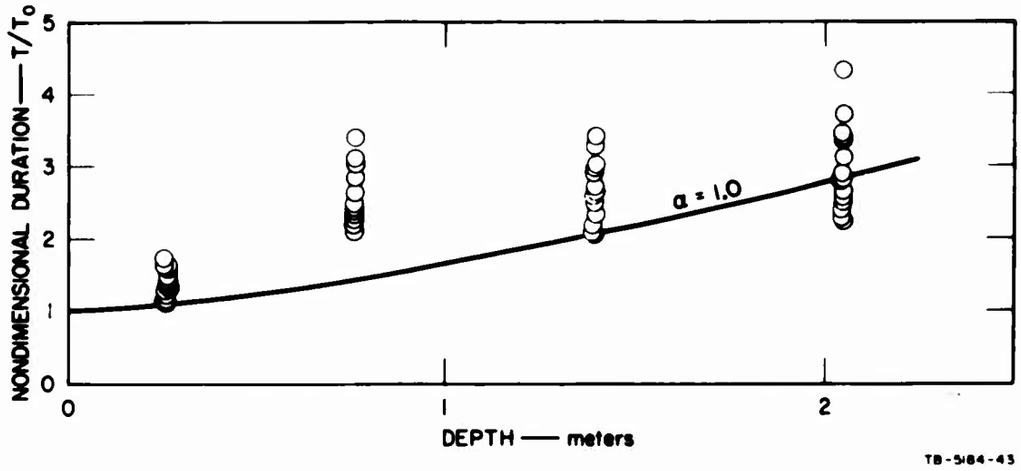

FIG. 4.15 STRESS WAVE DURATION: COLUMN C, KAOLINITE

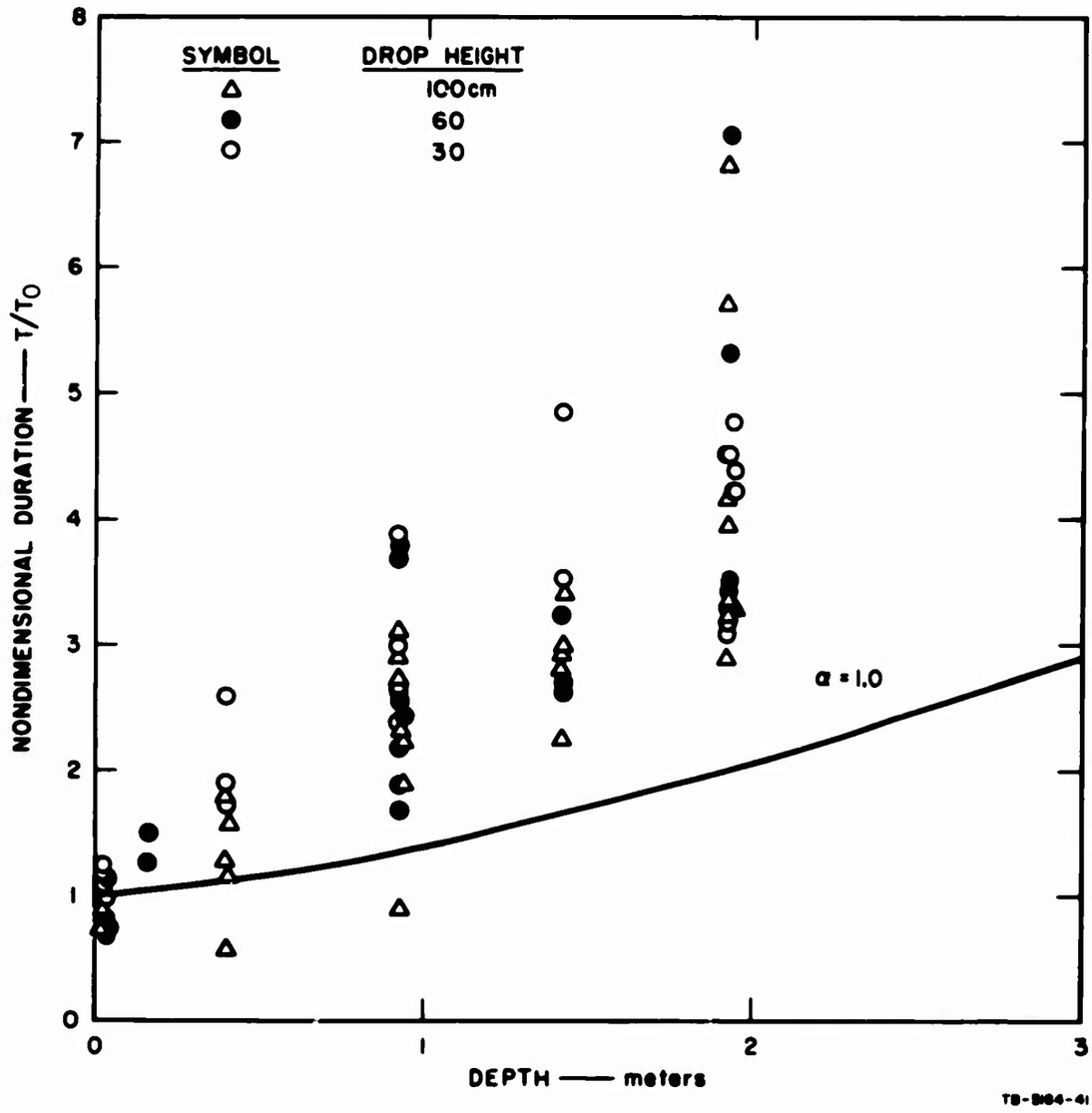

FIG. 4.16 STRESS WAVE DURATION: COLUMN D, VICKSBURG CLAY

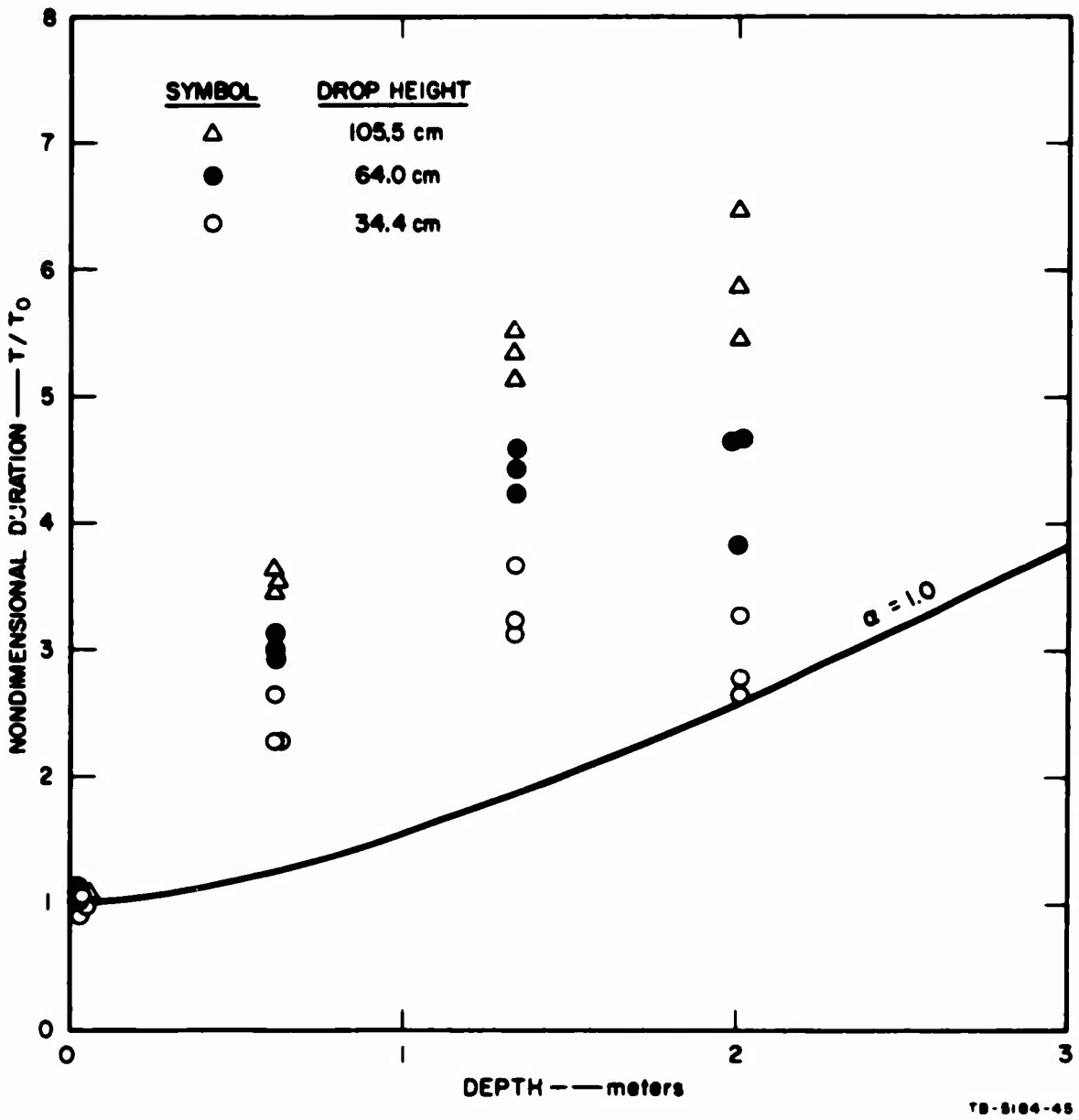

FIG. 4.17 STRESS WAVE DURATION: COLUMN F, VICKSBURG CLAY

No theoretical prediction is given for comparison with the data on duration. The duration prediction has not been worked out for the constant tan delta model or for the viscoelastic compacting model, and the prediction from the linear hysteretic model is inadequate in all

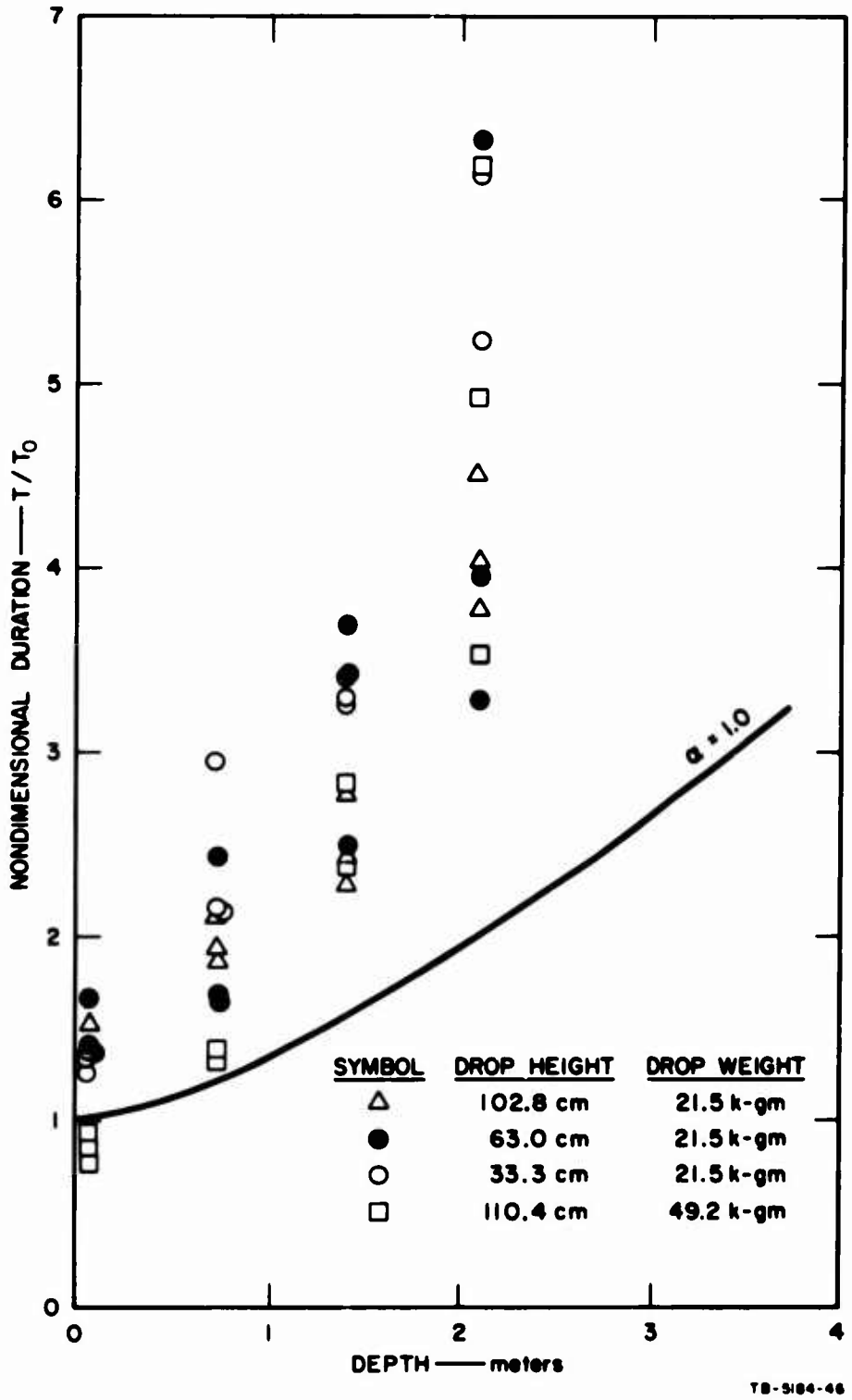

FIG. 4.18 STRESS WAVE DURATION: COLUMN E, MONTEREY SAND

cases. Instead, a curve for $\alpha = 1.0$ from the linear hysteretic model is given to provide a basis for comparing the data from one test with that from another. This curve shows a much faster change in duration than that for the value of α, which is appropriate for each soil.

For Column B, there are two theoretical curves corresponding to the two ranges of duration observed. It may be noted from the disparity between these curves that the rate of change of duration with depth is strongly dependent on the magnitude of the duration at the surface. The data tend to lie considerably above the relevant curves in both cases. The durations for Column C are also above the theoretical curve, although not markedly so. For Columns D, F, and E, the points are all well above the theoretical curve. This rapid change in duration of the stress wave is associated with the rapid attenuation of the peak. The observed durations are probably larger than the actual duration because of the nonlinear unloading response of the embedded stress gages. In Ref. 4, it was observed that the nonlinearity could cause an apparent increase of up to 60% in wave duration. This point is discussed further in Section 4.4.

Wave velocities were obtained from the slopes between points on plots of arrival time versus depth. A typical time-depth plot from Column C is shown in Fig. 4.19. The wave velocities associated with the arrival of the initial stress, of the peak stress, one-half peak stress, and one-tenth the peak stress are shown. This plot indicates that the time between the first arrival of stress and the arrival of the peak increased gradually with depth. For these tests, the wave velocity associated with the peak stress was essentially a constant; for the other columns it increased somewhat with depth.

Plots of the wave velocity (of the peak stress) as a function of depth are shown in Fig. 4.20. The velocities were determined from the difference in arrival times at gages at two depths, and the velocities are, therefore, plotted as a line between those two depths. The prediction lines were derived from an evaluation of the tangent modulus from compression tests described in Appendix B. Both the overburden

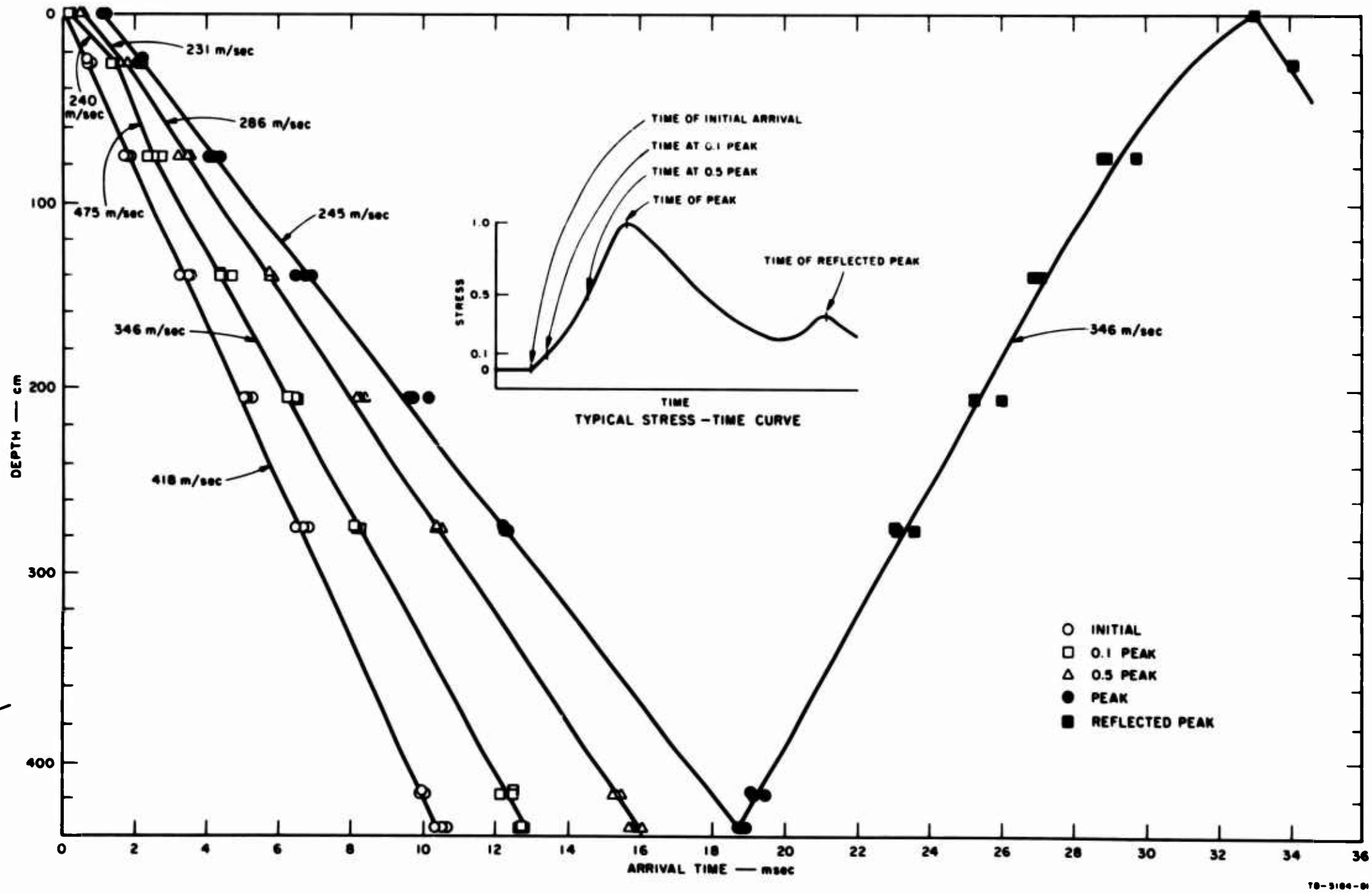

FIG. 4.19 ARRIVAL TIME-DEPTH PLOT: COLUMN C

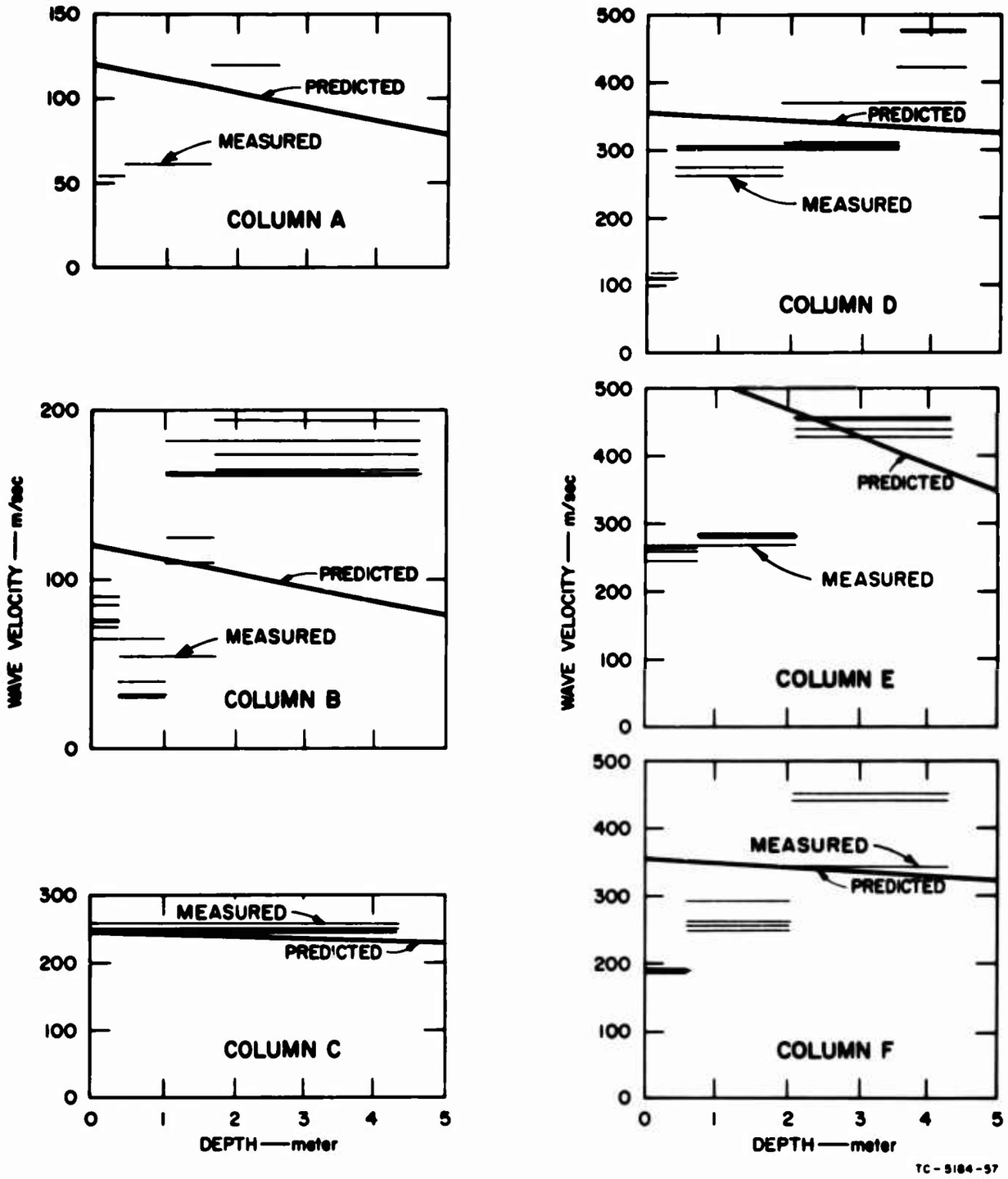

FIG. 4.20 WAVE VELOCITY OF THE PEAK STRESS

Predictions from Tangent Modulus Data, Appendix B

stresses and the peak dynamic stress levels were considered in developing the prediction. In each case, the predicted wave velocity decreased with depth, whereas the measured velocity increased with depth. However, the magnitudes of the predicted and measured velocities were similar. For all the clay columns, the predicted arrival time at the base (using the predictions of wave velocity as shown) were within 10% of the actual arrival times. The best correlation between experiment and prediction is clearly with Column C. This rather dry clay material had a nearly linear stress-strain relation, which was unaffected by preload or peak stress, and, therefore, it behaved much like a linearly elastic material during loading.

The predicted wave velocity for the sand was somewhat higher than the measured velocities. The predicted arrival time at the base was only 75% of the measured arrival time. If the secant modulus from the compression tests were used to obtain the wave velocity, then the arrival times would agree within 10% for the sand. It may be noted here that a disagreement between the actual and predicted wave velocities leads to disagreement in other predictions, such as that for stress attenuation. The predicted attenuation rate is directly dependent on the wave velocity. Since the wave velocity varies with depth in most cases, it should not be expected that a prediction based on a constant velocity would coincide with the experimental data.

Acceleration records were obtained from tests on Columns C through F. The peak accelerations are shown as a function or arrival time of the peak in Fig. 4.21. No prediction was made for acceleration. The lines on these plots indicate merely the trend of the data. In general, the acceleration attenuates with the square of the arrival time, and the magnitude of the peak is proportional to the magnitude of the applied stress. The softest soil of this group (Column D) gave the most rapid attenuation (proportional to time to the 2.7 power) as would be expected. However, the peak accelerations at the surface were highest for this column in contrast to what would have been expected. This latter discrepancy may be attributed to the fact that for different

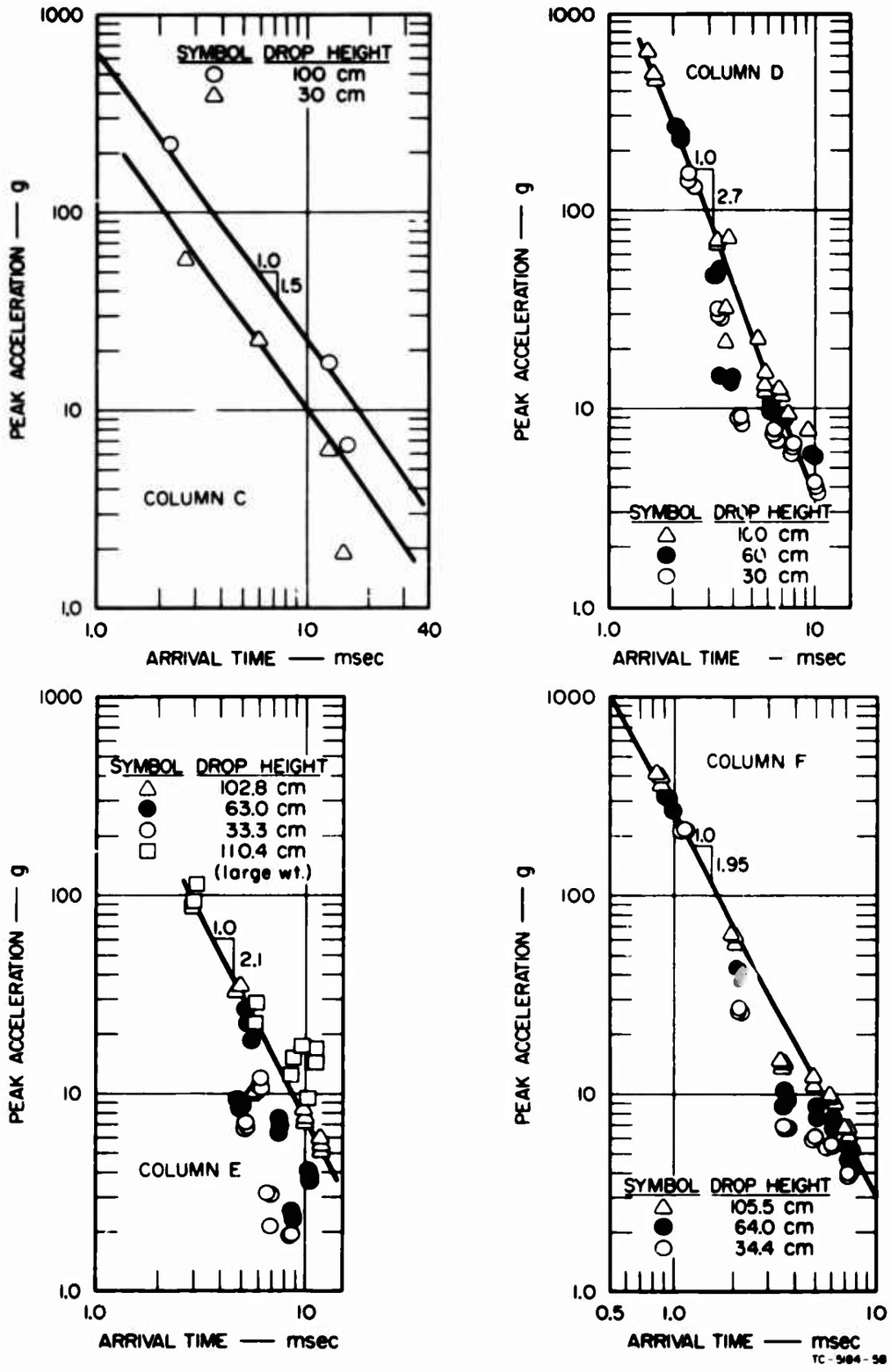

FIG. 4.21 PEAK ACCELERATION

series of tests there were different amounts and types of damping material placed on top of the column to reduce oscillations in the stress wave.

Particle velocity was determined by integration of the accelerometer response. For Column B, the acceleration signal was integrated electronically, and a velocity-time trace was displayed on the oscilloscopes. This particle velocity trace has a shape similar to that of the critical stress wave. For Columns C through F, the acceleration signal was recorded, and the area under the acceleration trace was integrated manually to obtain peak particle velocity. The experimental values of peak particle velocity are shown in Figs. 4.22 to 4.26. Along with the points are curves from the three theoretical models used to predict stress attenuation. The particle velocity at the surface was determined from the equation

$$v_{mo} = \frac{\sigma_{mo}}{\rho c_o} \tag{4.1}$$

where v_{mo} is the peak particle velocity at the surface,

σ_{mo} is the peak stress at the surface,

ρ is the gross density of the soil, and

c_o is the wave velocity at the surface, as predicted from compression test data.

The peak particle velocity was calculated only for the stress level obtained from the drop height of about 100 cm. Therefore, the theoretical predictions are directly applicable only to points obtained using that drop height.

The few points available from the Column B tests indicate that the constant tan delta model represents the attenuation reasonably well. The particle velocity at the surface appears to agree quite well with the prediction. The accelerometer at the next depth beyond those plotted 1.65 m, recorded a much lower particle velocity, below 10 cm/sec. This very sharp decrease in particle velocity coincides with the sudden increase in wave velocity that occurred at about 1.5 m (see Fig. 4.20). The particle velocity at the surface of Column C was also well predicted by Eq. (4.1). Down to three meters, the points lie near the theoretical

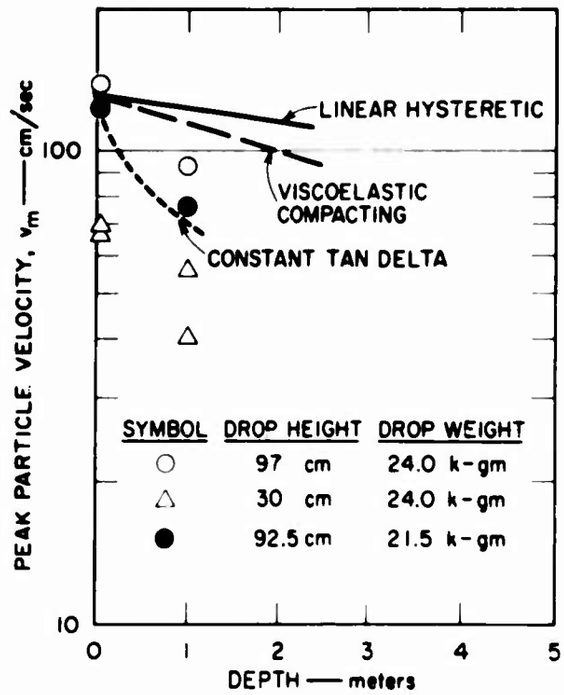

FIG. 4.22 PEAK PARTICLE VELOCITY: COLUMN B

Same Curve Parameters as for Fig. 4.8

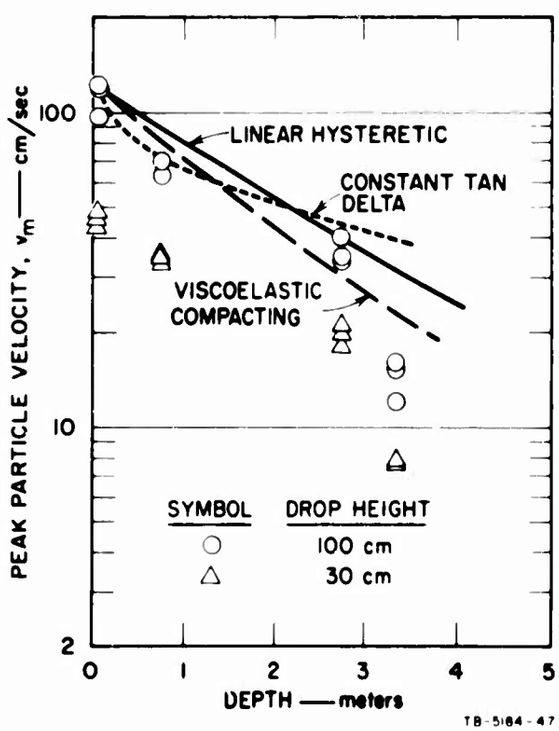

FIG. 4.23 PEAK PARTICLE VELOCITY: COLUMN C

Same Curve Parameters as for Fig. 4.10

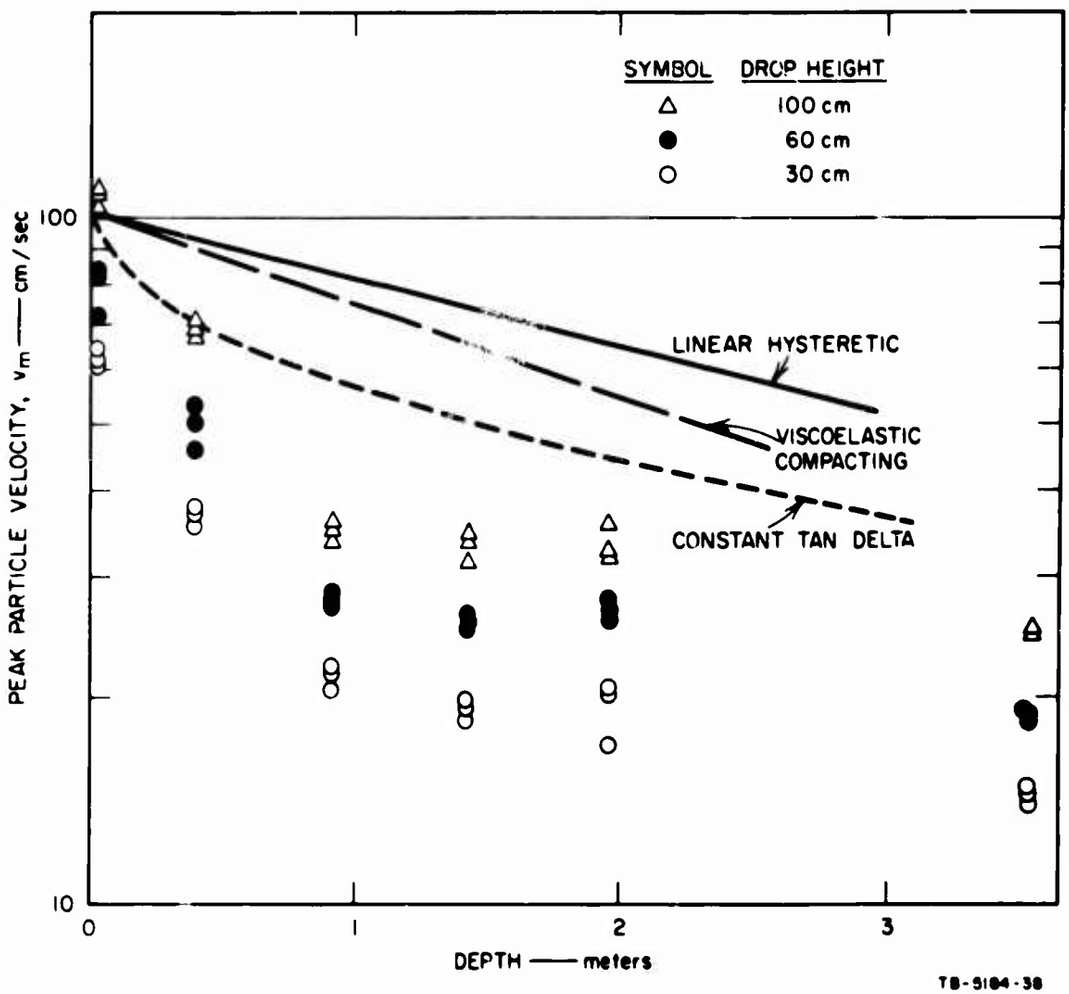

FIG. 4.24 PEAK PARTICLE VELOCITY: COLUMN D

Same Curve Parameters as for Fig. 4.11

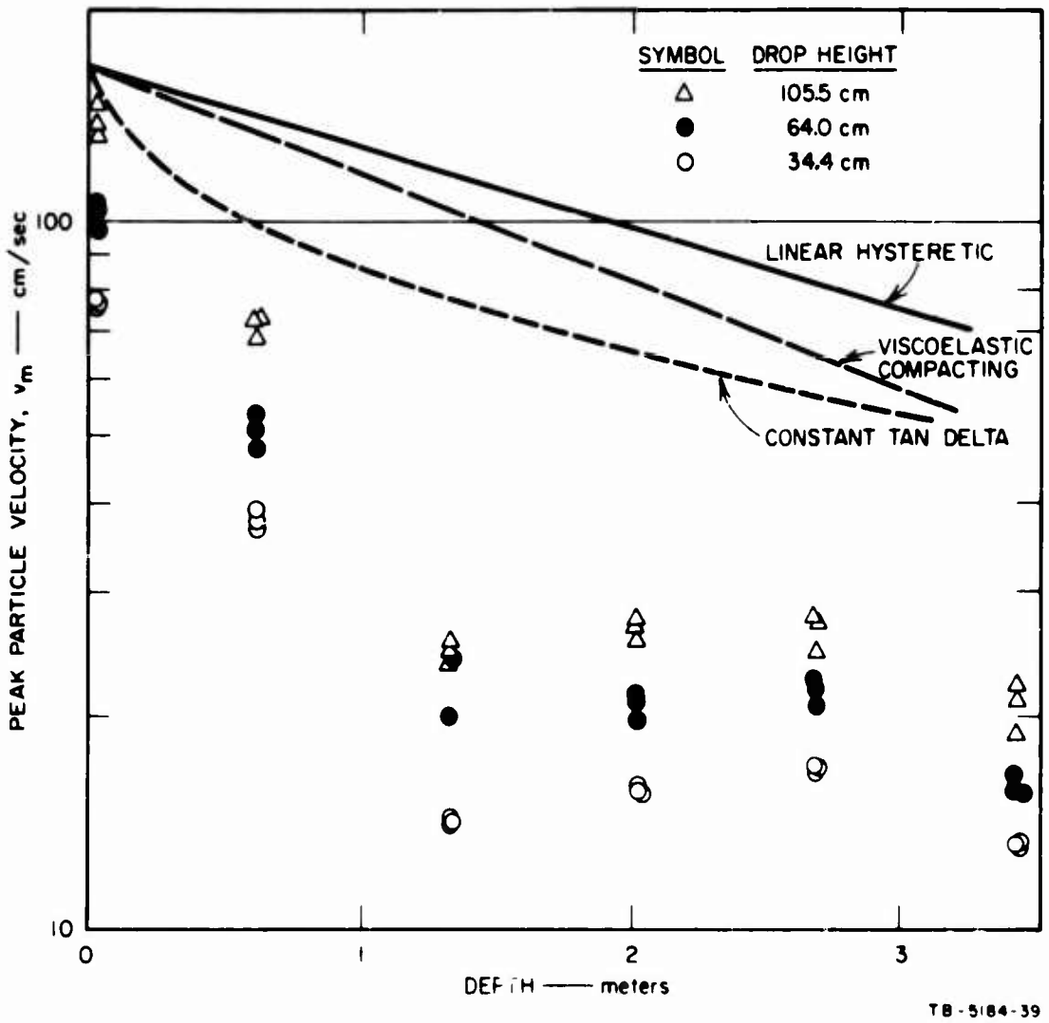

FIG. 4.25 PEAK PARTICLE VELOCITY: COLUMN F

Same Curve Parameters as for Fig. 4.12

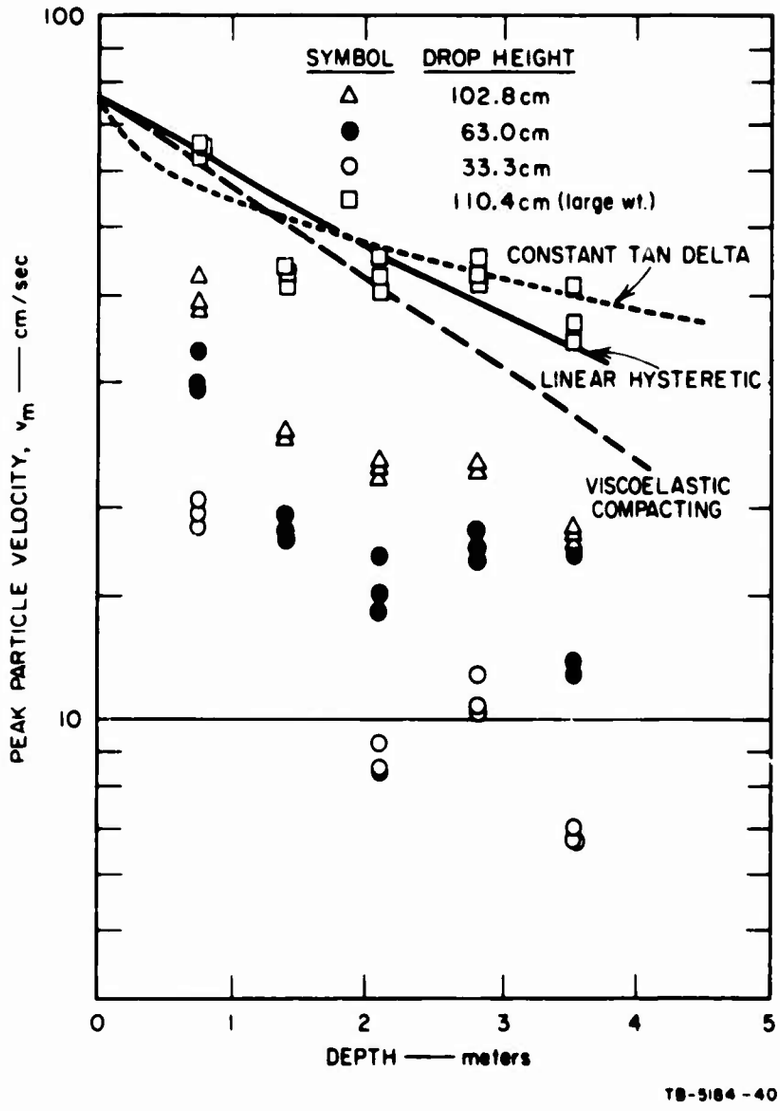

FIG. 4.26 PEAK PARTICLE VELOCITY: COLUMN E

Same Curve Parameters as for Fig. 4.13

curve for the constant tan delta model. There is a sudden decrease in particle velocity beyond that depth, caused by the coincidence of the reflected wave from the base with the initial wave. The particle velocity in the initial wave is downward while the reflected wave has an upward velocity; hence, the partial coincidence of the waves tends to reduce the peak value.

In both Columns D and F, the particle velocity appears to have attenuated much faster than predicted. Actually, the attenuation is initially high, down to 1 meter, and from there on it is quite gradual. This trend is similar to that indicated by the constant tan delta model. Again, the predicted velocity at the surface is quite close to the measured values.

4.4 Discussion

These one-dimensional wave propagation tests on clays and sands indicated that the wave transmission properties of the two types of soil were very similar. In fact, stress and acceleration records obtained from tests on the two materials were identical qualitatively and only slightly different quantitatively.

Stress attenuation is of most interest and so it will be discussed in detail first. The discussion will then turn to the stress wave duration, the stress measurement methods, and the wave front and wave velocity.

4.4.1 Stress Attenuation. Stress attenuation is used here to mean the decrease of the peak stress as a function of distance from the point where the load is applied. For all the tests made the stress attenuated 60 to 80% through the length of the 5-meter column. The curve of stress attenuation versus depth were all quite similar: nothing distinguished those for sand from those for the clays.

These data in combination with the theoretical models provide an initial basis for predicting attenuation caused by material dissipation. In each of the three models used in Section 4.3, attenuation in a given soil is a function only of $z/(cT_0)$. Thus, if the attenuation is known

for $z = 2$ meters, $T_0 = 2$ msec, it can be assumed to be the same for $z = 200$ meters and $T_0 = 0.2$ sec.

There is considerable scatter in the experimental results for stress attenuation. This dispersion of the data can be attributed to several causes, which should be considered in any future test program:

1. Plotting procedure. The peak stress data were plotted versus depth for the convenience of other investigators who might desire to evaluate the data. With this method there is no way to account for differences in wave duration or wave velocity. An alternate abscissa, which partially accounts for these factors, is discussed later.
2. Irregularity of the wave shape. The theory for all three of the models considered indicates that attenuation is directly dependent on the rate of decay of the applied stress. The applied stress wave form varied from test to test so that it is not surprising that the attenuation rate also varied.
3. Variation in stress gage calibration. The stress gage calibration changes slightly from test to test. Hence, the value of peak stress is only known within about 20%. This will be discussed later.

The correlation between theory and experiment is rather poor. The theoretical prediction requires a knowledge of the wave velocity, one or two attenuation parameters, and the duration of the applied stress. If any of these is off, the prediction will be inaccurate. Thus, the correspondence between experimental and theoretical attenuation is not a very sensitive measure of the applicability of any model. Particular problems that lead to differences between theory and experiment are

1. Varying wave velocity. In the experiments, the velocity often varied considerably with depth; however, all the models (including the nonlinear model of Appendix D) showed a constant or nearly constant wave velocity. The varying velocity tends to distort the attenuation pattern so that the theoretical and experimental curves cannot be expected to coincide.

2. Incompleteness of the models. None of the models fully represents soil that shows a nonlinear stress-strain relation, rate-dependence, and a compacting character. Each model studied represents only one or two of these factors.
3. Improper evaluation of parameters. Because none of the models actually represents in detail the behavior of soil, the model parameters must be evaluated on some fairly arbitrary basis. For instance, tan δ of the constant tan delta model could be evaluated by the experimental lag time, width of the hysteresis loop, area of the hysteresis loop, from a creep curve, from the damping observed during oscillatory loading, from the variation of modulus with frequency, etc. Because the soil is not precisely represented by the constant tan delta model, all of these bases for evaluation will give different values for tan δ. Hence, a model may give a poor prediction because its parameters were improperly evaluated, not because the model is inappropriate. Thus, it is very important to choose the most suitable basis for evaluation.
4. Dependence of parameters on stress level. Each of the dissipation parameters and wave velocity depend on the stress level. Hence, in a column in which stress varies with depth, the dissipative parameters will also vary with depth. Of course, these variations were not considered in the theoretical predictions. Rather, parameters were chosen appropriate to the maximum applied stress (the stress obtained with the drop height of about 100 cm).
5. Form of the applied stress. The applied stress assumed for all the theoretical work had a shock front and an exponential decay after the front. The stress pulse applied by the drop weight had a finite rise time of 0.3 to 1.0 msec, a rounded peak and a decay thereafter. This difference between theoretical and experimental applied stress should affect attenuation significantly near the top of the column.

The main value of these tests and related theory may be to point out the variables involved. Unfortunately, the quantitative significance of each variable cannot be assessed from our test results.

Stress attenuation graphs are the easiest to use for predictions for a particular soil and applied stress if they are plotted as peak stress versus depth. However, the natural coordinates from the theoretical standpoint appear to be nondimensional peak stress versus a nondimensionalized arrival time or depth. This depth abscissa is

$$\tau_p = \frac{t_p}{T_o} = \frac{1}{T_o} \int_0^z \frac{dz}{c_p}$$

where τ_p is the nondimensional arrival time of the peak, or the nondimensional depth of the measurement point,

t_p is the time difference between the arrival of the peak at the surface and the arrival at the depth of interest,

T_o is the duration of the wave at the surface,

z is the depth, and

c_p is the wave velocity associated with the peak stress.

This definition of nondimensional depth as the logical abscissa agrees with the analyses of the constant tan delta, linear hysteretic, nonlinear hysteretic, and viscoelastic compacting models. An example of the use of this abscissa with the soils data is shown in Fig. 4.27. This figure contains all the stress attenuation data points from Column B (wet kaolinite). The applied stress in these tests varied from 0.58 to 2.5 bars and the duration of the wave was 2.5 or 6 msec. These data are also shown in Figs. 4.8 and 4.9 with depth as the abscissa. The two figures were required because of the variation in time constants from 2.5 to 6.0 msec. The data can be combined in Fig. 4.27 because the nondimensional abscissa accounts for the variation in time constant. The scatter of data in Figs. 4.8, 4.9 and 4.27 should be compared to get an idea of the value of nondimensional depth as the abscissa.

The use of this nondimensional abscissa minimizes the importance of variations in the wave velocity. The stress attenuation data

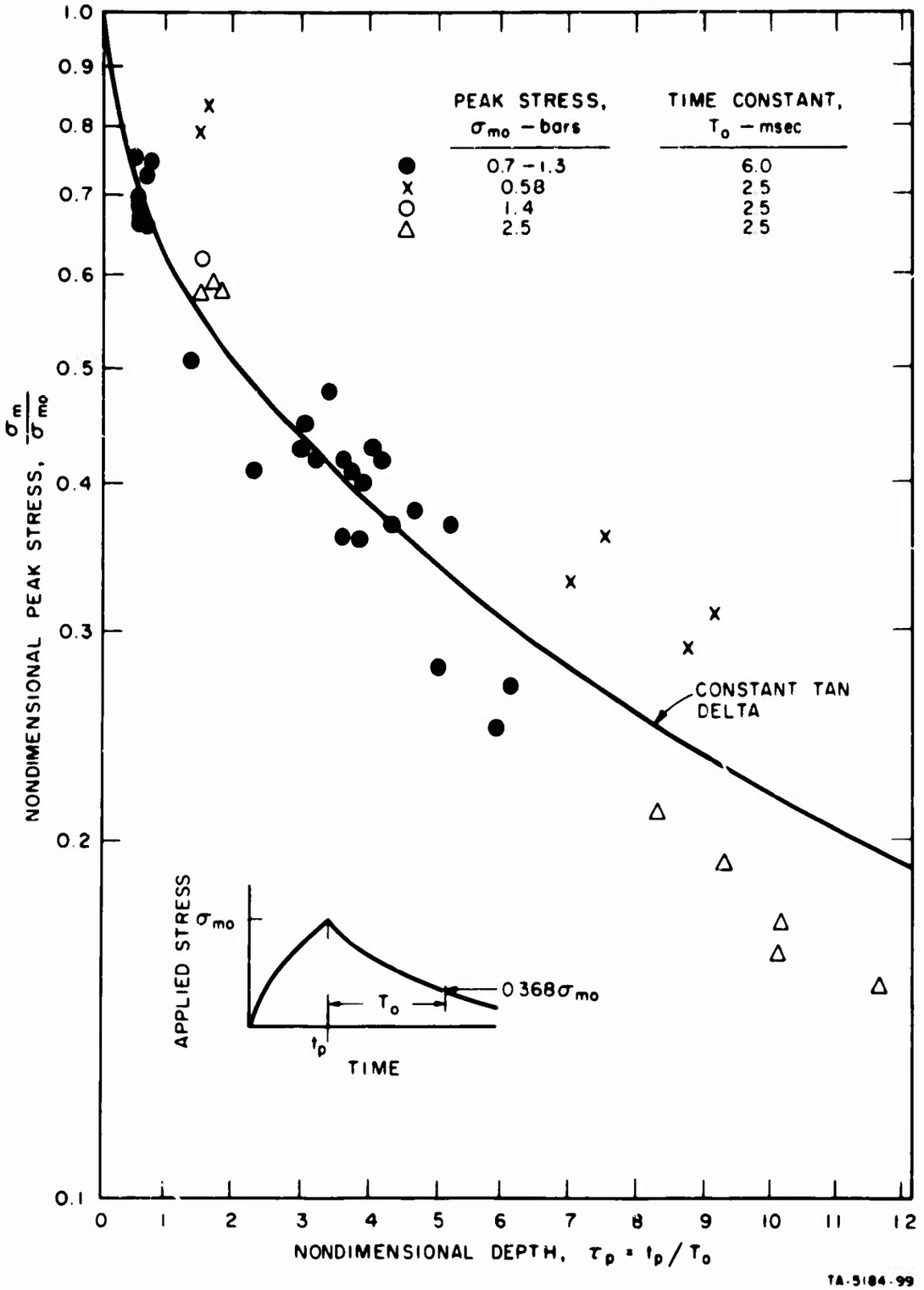

FIG. 4.27 STRESS ATTENUATION WITH NONDIMENSIONAL DEPTH: COLUMN B

Tan δ = 0.30

presented earlier (Fig. 4.7-4.12) show, in most cases, an extremely rapid attenuation initially and then a more gradual decay thereafter. This pattern is directly related to the fact that the abscissa is depth and that the wave velocity is low at the surface and increases with depth. If the arrival time were used as the abscissa, the attenuation rate would be considerably more uniform and would correspond more closely to theoretical predictions. All models used in the predictions exhibit a constant wave velocity; hence, they cannot be expected to predict accurately phenomena that depend on wide variations in wave velocity.

Even if the nondimensional depth were used as the abscissa, the attenuation curves would not be linear on the semilog plots. There would still be a rapid attenuation at high stress levels and a more gradual attenuation later. This pattern contrasts with the curves of the linear hysteretic and viscoelastic compacting models, which are nearly linear in the range of present interest. The constant tan delta model gives the desired pattern, but it is not unique in this respect. The nonlinear hysteretic model, which is analyzed in Appendix D, also gives the desired attenuation pattern. The latter model has a rate-independent stress-strain relation, which is concave to the stress axis. The particular attenuation pattern obtained is caused by the introduction of geostatic stress, a factor that does not enter the analyses of the other models. Hence, no firm conclusion can be reached concerning the suitability of any one of the models for attenuation predictions.

4.4.2 Stress Wave Duration. The stress wave duration is not a quantity that needs to be known precisely to predict the behavior of a structure buried in the soil. However, the concern here is to know why the theoretical predictions are so different from the measured values. At all depths, the durations are much longer than predicted. There are several possible explanations for this difference and probably all of them have some validity. One explanation is that the models are based on too small a dissipation parameter. A larger amount of dissipation would increase the predicted rate of increase of duration and it would

also increase the predicted rate of stress attenuation. Both effects would put the predicted values closer to the experimental ones but would still not account for the large change in duration. A second possibility is that the models are not adequately representing some important feature of the soil. This is a possibility, although it is doubtful that a model could predict stress attenuation but not the lengthening of the stress wave. A third explanation is that the stress records are consistently in error. Such an error in the record has been alluded to in Ref. 4, where it was noted that the unloading calibration of the stress gages could be markedly different from the loading calibration. An example is given in Fig. 4.28 for three gages buried a few centimeters below the surface in a container of sand. It should be noted that the gage always reads the same under a given stress on its sensitive surface. Hence, the disagreement between loading and unloading calibration means that the average stress applied by the soil to the gage is not equal to the average stress in the soil sample. The calibration information of Fig. 4.28 was replotted in Fig. 4.29 to show the nature of the unloading nonlinearity. Surprisingly, the ratio of unloading to loading response is a simple linear function of the average applied stress. What effect does this calibration anomaly have on the stress records? Suppose that this static calibration is applicable during a wave propagation test. Then, an exponential stress wave will be distorted as shown in Fig. 4.30. In this example, the duration of the recorded stress is 47% longer than that of the average stress on the soil.

The difference between loading and unloading calibration is caused by stress redistributions about the gage. Such redistributions require some time to occur as shown by Mason, et al[17], so that the unloading calibrations will depend on the rate at which unloading occurs as well as on how soon it begins after the peak load is reached. For a quasi-static loading, the redistribution will be complete so that the difference between loading and unloading curves will be maximum. Therefore, the stress waves measured during wave propagation tests are distorted less than shown in Fig. 4.29, but the amount of distortion will vary with

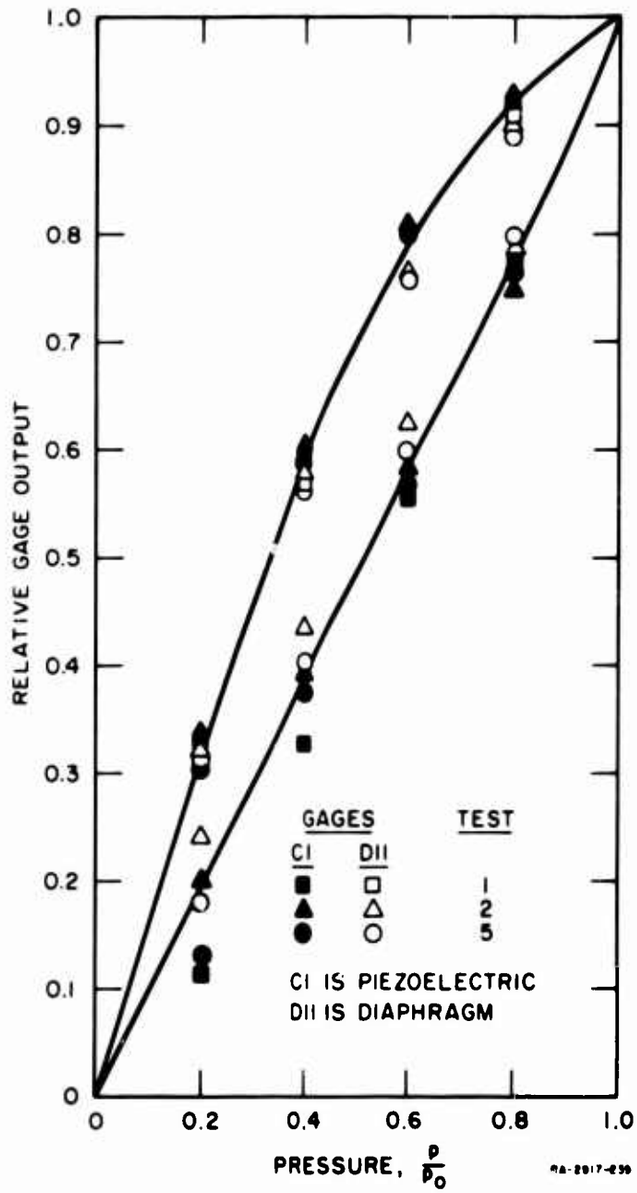

FIG. 4.28 RESPONSE OF EMBEDDED STRESS GAGE TO UNLOADING

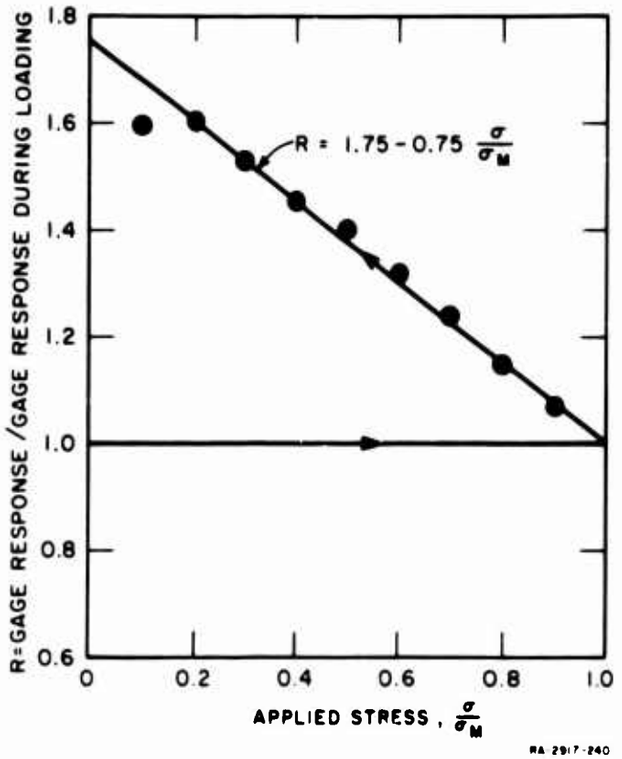

FIG. 4.29 STATIC UNLOAD CALIBRATION FOR EMBEDDED STRESS GAGES

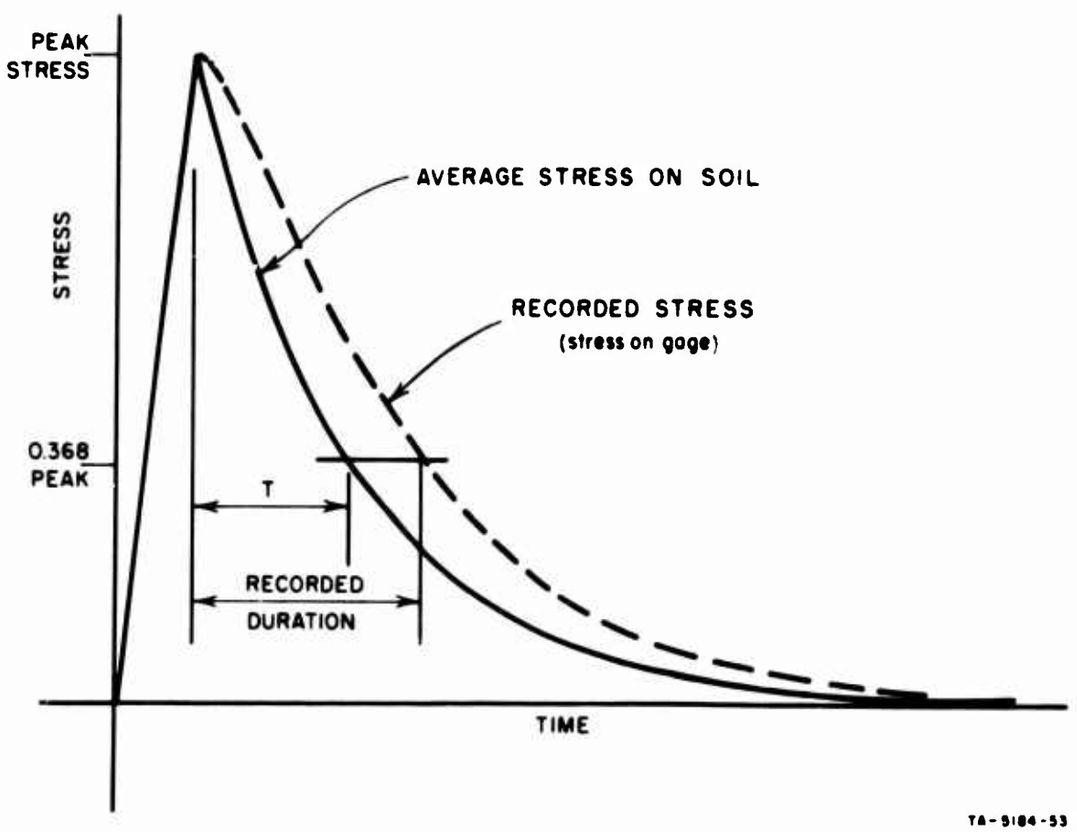

FIG. 4.30 MODIFICATION OF STRESS RECORD FOR NONLINEAR UNLOADING RELATION OF STRESS GAGE

stress decay rate and from soil to soil. Because the stress decay rate decreases with depth, the distortion probably increases with depth.

Variables, such as soil type, density, and moisture, which affect the relaxation time of a soil, will also influence the amount by which recorded stress waves will be distorted (because the stress redistributions that cause the distortion are time-dependent).

4.4.3 Stress Gage Calibration. The stress gage calibration was a static procedure. It was based on the assumption that the stress wil be distributed on the gage in the same way under static and dynamic conditions. This method is simple and repeatable but not completely justifiable. There are at least two factors to indicate that static and dynamic calibrations should differ.

The calibration depends on the manner in which the soil distributes the stress over the gage. As the stress is applied to the soil, the stress distribution changes. This change requires time (several milliseconds in sand) so that for a given average applied pressure, different stresses will be applied to the gage by the soil for different loading rates. Because the stress redistribution is a time-dependent affair, it would be expected that highly time-dependent soils would lead to large differences between the static and dynamic calibrations and that time-independent soils would show no difference. This expectation is hinted at by the nicely repeatable data from the stiff soil of Column C.

The stress distribution in the vicinity of the gage is greatly influenced by the radial stress of the tube on the soil. The radial stress is caused by a Poisson effect when axial stress is applied to the soil. When the axial stress is decreased, the radial stress also decreases but much less than the axial stress. Plastic equilibrium of the soil requires that the radial stress not exceed four or five times the axial stress and that it not fall below zero. However, the magnitude of the radial stress within that range cannot be defined by statics. Hence, it may vary from test to test in a fairly arbitrary manner. Thus, the static calibrations were made with a different radial stress acting than that during the dynamic test.

From discrepancies between the response of adjacent stress and force gages, we concluded that the stress gage calibrations err by ±20% in situations where repeated testing is done.

4.4.4 Wave Velocity. The velocity with which waves travel through the soil is not solely related to one property of the soil. Rather the wave velocity is a product of the complex interaction between the propagating wave and the soil. Wave velocity is primarily a function of the stiffness or compression modulus of the soil. But velocity is also affected by the rise time of the stress wave, the viscoelastic or time-dependent dissipation of the soil, by the variation of the soil stiffness with depth, and by the concavity or convexity of the stress-strain relation of the soil. The effects of the rise time and decay rate of the stress wave on wave velocity are shown in the time-depth plot of Fig. 4.31. This plot shows the wave interactions for a wave propagation calculation using the linear hysteretic model. The applied pressure represented by incremental steps is plotted above the coordinate line, the waves, below. The wave velocity is the slope of the lines on this diagram. When lines are drawn between the points of maximum stress, a "wave velocity" for the maximum stress can be determined. Two points may be noted concerning this "velocity": it is not the loading or unloading velocity of the material but is intermediate to these, and it is a nonlinear function of depth, although the model has only linear characteristics.

Time dependence of the soil also affects the wave velocity because it caused the soil modulus to increase as the loading rate increases. Thus a shock wave would travel faster than a gradually rising stress wave. If we add such factors as nonlinear loading and unloading relations, and properties that vary with depth, it should be clear that the "wave velocity of the peak stress" is difficult to relate to the material properties. However, this "velocity" is of most interest to the predictor. Therefore it is important to have some basis for estimating this velocity.

We have attempted to correlate the wave velocity of the peak stress with the wave velocity computed from the tangent modulus of the stress-strain curve of the soil. Such a correlation is necessarily approximate

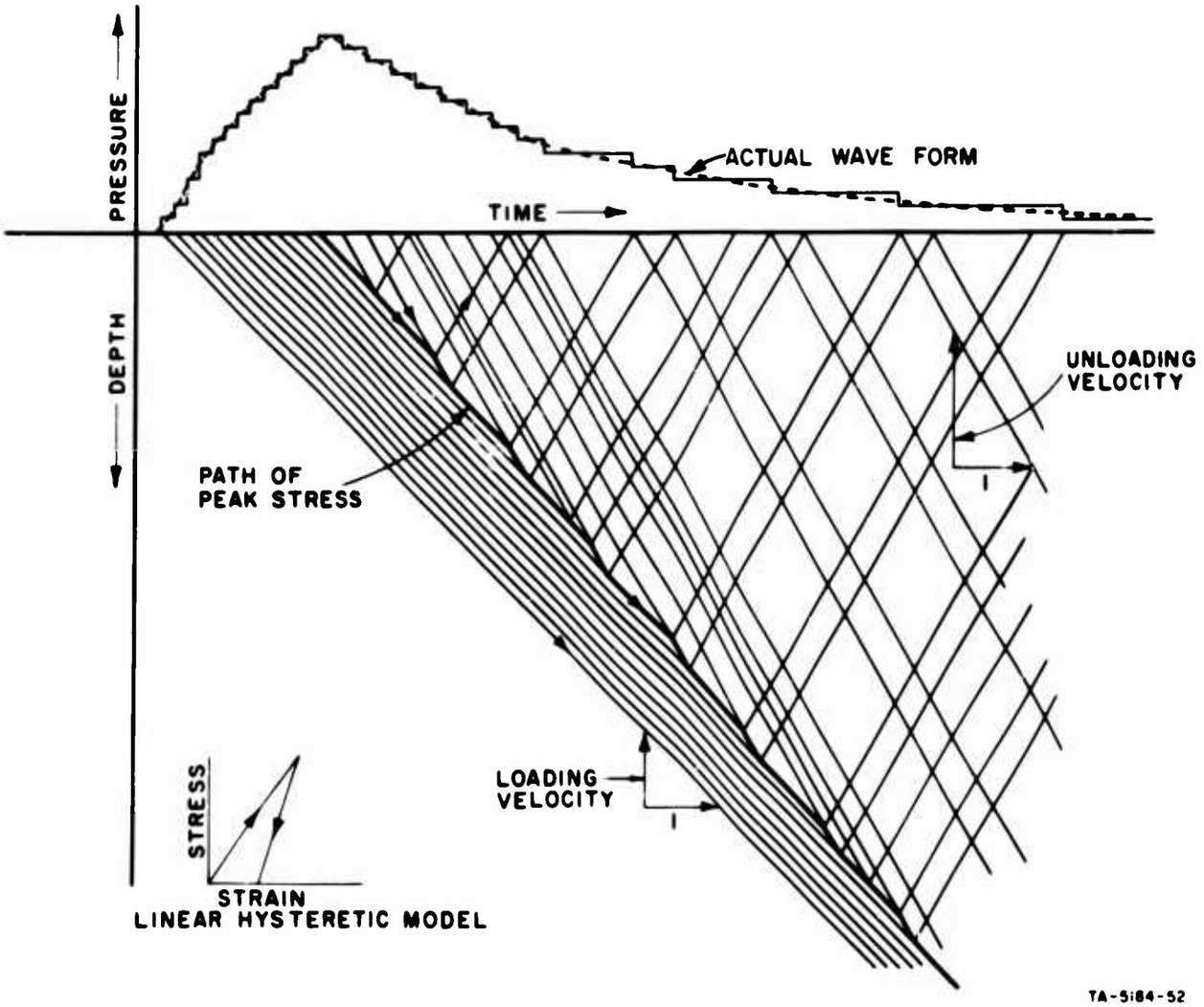

FIG. 4.31 TIME-DEPTH PLOT FOR CALCULATION WITH LINEAR HYSTERETIC MODEL

but it has indicated that a reasonable velocity estimate can be obtained from the tangent modulus. As pointed out in Section 4.3 the average wave velocity through the clay column is within about 10% of the wave velocity computed from the tangent modulus and within 25% for the sand column. And this computed wave velocity served as a good basis for calculating the peak particle velocity for all the clay tests.

It is possible that the waves recorded should be considered shock waves instead of stress waves. Normally a shock wave has a very brief rise time (fraction of a microsecond) and this rise time would remain constant at all depths; these conditions are not met by the recorded waves. Zaccor, Wallace, Durkin, and Mason[18] have suggested that a rise

time of around 100 microseconds in sand should be considered a shock front. If the wave is a shock, then the wave velocity is associated with the secant modulus of the stress-strain relation. If the wave is not a shock, the velocity would depend on the tangent modulus. The wave velocities measured in our tests are affected by many things besides the modulus. Therefore, the fact that our correlation was best with the tangent modulus is not a sufficient basis for deciding that the waves are stress waves.

The soil tube which is required to provide the one-dimensional conditions also has some effect on both wave velocity and attenuation. Whitman[4] has noted that it was necessary to account for the mass of the tube in determining the wave velocity, c, from $c^2 = M/\rho$, where M is the soil modulus and ρ is the combined density of the soil and tube. That is, the tube tends to reduce the wave velocity.

The tube may also increase the attenuation rate of high frequency components in the wave. This increased attenuation could be caused in two ways: by the radial acceleration of the soil and by friction against the wall of the tube. Both of these effects would be more effective in attenuating high-frequency than low frequency components of the stress wave. These two effects might remove very little energy from the pulse but contribute significantly to reducing the steepness of the wave front.

CHAPTER 5

DISCUSSION OF THEORETICAL MODELS

5.1 Introduction

Theoretical models are the needed link between soil behavior in compression tests and soil behavior during wave propagation. The models show the relation between compression modulus and wave velocity, between hysteresis loop (of a stress-strain curve) and attenuation, and between strain lag and attenuation. Thus, the models are the basis of a method whereby one can observe phenomena in a compression test and then predict the wave propagation behavior. The models can be used either for theoretical analyses of wave propagation or to provide the scaling laws for relating the soil behavior under different test conditions.

No complete model for soil has been developed. Rather we have studied models which exhibit some of the main features of soil. The organization of the study can be seen in Table 5.1. In this table the models are separated according to the type of material dissipation which they represent. Compaction means the type of dissipation in which there is a permanent deformation after a loading cycle. A linear compacting model here means a model which has a linear stress-strain relation during loading and a linear relation during unloading. The second type of dissipation is time-dependent (viscous). Superposition is valid in the analysis of linear time-dependent models.

The elastic model is the simplest and exhibits no dissipation. The linear hysteretic model (see Ref. 3 and 10) shows permanent set after a loading cycle and exhibits the same behavior at all loading rates. The S-hysteretic model (Appendix D) has an S-shaped stress-strain relation during loading (first convex then concave to the stress axis) and an unloading relation which is concave to the stress axis. The standard linear viscoelastic (three-element) model and the constant tan delta

model exhibit frequency-dependent dissipation but no permanent set. The standard linear model (see Ref. 1) has a maximum dissipation at one frequency and none at zero and infinite frequencies; whereas, the constant tan delta model (see Ref. 3) has the same dissipation at all frequencies. The viscoelastic compacting model analyzed in Appendix C is the first to contain both compacting and time-dependent dissipation.

TABLE 5.1

TYPES OF SOIL MODELS

		Compaction		
		none	linear	nonlinear
Time-Dependence	None	Elastic	Linear hysteretic	S-hysteretic
	Linear	Constant tan delta, standard linear viscoelastic	Viscoelastic compacting	-
	Nonlinear	-	-	True model for soil

In the same table the true model for soil is shown as a nonlinearly time-dependent and nonlinearly compacting model. An example of the nonlinear time-dependence required to represent soil is the model developed by Kondner.[13,14] The nonlinear compaction of soil is represented by the S-hysteretic model.

5.2 Viscoelastic Compacting and S-Hysteretic Models

Two models were analyzed on the present project to determine their wave propagation response. The viscoelastic compacting model is discussed in Appendix C and the S-hysteretic model is treated in Appendix D. These two models represent logical extensions from the earlier models in the direction of a more complete representation of soil.

The viscoelastic compacting model was formulated as a combination of the linear hysteretic and standard linear viscoelastic models. This model was analyzed to ascertain the effect of combining time-dependent

and time-independent dissipation. Because soil contains both types of dissipation, it is reasonable to investigate such a model. The theoretical results of Appendix C show that the combined effects can be obtained approximately by a superposition of the separate effects of the two types of dissipation. That is, the attenuation exhibited by the viscoelastic compacting model can be found by combining the attenuation determined from the two component models, the linear hysteretic and standard linear viscoelastic. The wave front variations are also merely a combination of the behavior of the component models.

The analysis developed in Appendix C for the viscoelastic compacting model is based on a known solution of the wave propagation problem in the linear hysteretic medium. Through the use of the correspondence principle the known solution was altered to form the solution for the viscoelastic problem. Because of the generality of the approach, the analysis is applicable to any model constructed by the introduction of linear viscoelasticity to the linear hysteretic model. Therefore, the analysis could be used for a model built by combining the linear hysteretic model with the constant tan delta model. The S-hysteretic (or nonlinear hysteretic) model was analyzed to study the effects of geostatic stress on attenuation and to investigate the development of the wave front. For these purposes the model was constituted as a strain-rate-independent model with nonlinear loading and unloading relations. The loading relation is convex to the stress axis at low stresses and concave at high stresses. This initial convex portion, which has been observed in dynamic compression tests, is a function of the preload or geostatic stress. Its presence helps to explain the fact that seismic waves (zero stress level disturbances) travel at much higher velocities than large amplitude stress waves. It also explains the existence of small precursors in wave propagation tests: hence, it is associated with modifications of the wave front. The remainder of the loading curve and all the unloading curve are concave to the stress axis: this behavior corresponds to that observed in dynamic compression tests on soil. With these loading relations it was possible to study the effects brought about by the curvature of the stress-strain relation and the geostatic stress. The

analysis of the S-hysteretic model was completed only for the case of purely concave loading and unloading relations. With these relations a shock front remains a shock at all depths--no precursors occur. Hence, no information was obtained on wave front formation. However, the analytical results did provide information about the effect on stress attenuation of geostatic stress, curvature of the stress-strain relations, decay rate of the applied stress, and stress level. The most significant finding was that the combination of geostatic stress with a curved loading relation decreased the attenuation rate markedly. The predictions from this model were not used to compare with the experimental data of Chapter 4. For attenuation the predictions in all cases would show less attenuation than those of the linear hysteretic model.

5.3 Suitability for Use in Predictions

To be readily usable for wave propagation predictions a model must be tractable analytically. The elastic model is the easiest to analyze because it is linear and elastic and has but one parameter, a wave velocity. The linear hysteretic model is piecewise linear so that a restricted superposition is valid. The time required for an analysis of this model is comparable to that required for the linear viscoelastic models. Because the viscoelastic compacting model is based on linear and piecewise linear components, it can be analyzed using a restricted superposition and is thus only slightly more complex than the piecewise models. The S-hysteretic and nonlinear time-dependent models are considerably more difficult to analyze because superposition cannot be used. It is possible to analyze the true soil model for wave propagation behavior. However, for practical use in predictions, the most complicated model required will probably be the viscoelastic compacting.

Let us now survey the models for the suitability of their wave propagation predictions.

Attenuation. Only the elastic model does not exhibit any attenuation of peak stress or particle velocity. The standard linear viscoelastic model shows attenuation which is a function of arrival time but is independent of the decay rate of the applied pressure (in the depths which have

been studied). The other models all show attenuation as a function of arrival time and pressure decay rate. The experimental results show that attenuation is a function of the pressure decay rate and arrival time.

Wave Front. The constant tan delta model and the S-hysteretic model exhibit a rise time which increases with depth; this behavior is also shown in the experiments. The other models all show an initial shock front which does not vary with depth. (If the viscoelastic compacting model were formulated as a combination of the constant tan delta model and the linear hysteretic model, then the rise time of the stress wave in this model would increase with depth.)

Duration. Only the elastic model provides for no change in duration of the stress wave as it travels through the material. All the others show some lengthening of the stress wave with depth. The experimental data also show considerable lengthening of the wave with depth.

Compression Test Data. If a model is to be useful for wave propagation predictions, its parameters must be derivable from other soil test data such as that from compression tests. The time-dependence, the compaction, and the nonlinearities are all exhibited in these tests One of the main features of test results is a loop (closed or open) between loading and unloading stress-strain curves. Such a loop is exhibited by all but the elastic model. The experimentally observed lag between peak strain and peak stress is present only in the time-dependent models The concave upward nonlinearities of the stress-strain curve are observed only in the S-hysteretic model. Hence, none of the models exhibits all the main features which are noticed in compression data.

The previous discussion has considered only the potentialities of the models, not their actualities or the quantitative correctness of their predictions. The importance of such a survey is the following: if we wish to predict the increasing rise time of the stress wave, we need consider only the S-hysteretic and the constant tan delta models.

A model with potential value in predictions is a viscoelastic compacting model composed of constant tan delta and linear hysteretic elements. This model could be analyzed readily (the method has been worked out in

Appendix C) and would exhibit attenuation, and changes of wave front and duration similar to those seen in wave propagation experiments. It also would show both the time-dependent and compacting type of dissipation seen in compression tests. Its drawbacks are that it provides for a constant wave velocity at all depths, has the same time-dependent dissipation at all frequencies, and shows no variation of dissipation with stress level.

APPENDICES

A WAVE PROPAGATION TESTS

B SOIL PROPERTIES

C VISCOELASTIC COMPACTING MEDIUM

D NONLINEAR HYSTERETIC MEDIUM

BLANK PAGE

NOTATION FOR APPENDIX A

A = area (cm^2)

g = acceleration of gravity

h = height of drop

I = impulse per unit area of soil cross-section (bar-msec)

M = mass of the drop weight (kgm), or mass of isolated soil element shown in Fig. A.10.

t = time

v = particle velocity (cm/sec)

σ = stress (bars), subscripts refer to depth in the column

Appendix A

WAVE PROPAGATION TESTS

A.1 Introduction

Details of the wave propagation tests with six columns of soil are given in this appendix. Information on the construction of the column and test apparatus, the gages used, calibration procedure, and data reduction procedures is included. The most important results from these tests--the attenuation of peak stress, the attenuation of particle velocity and acceleration, variation of wave velocity with depth, and a discussion of the variation of the stress wave with depth--are found in Chapter 4.

A.2 Test Facility and Gages

Unidimensional wave propagation testing required the construction of a test facility in which essentially one-dimensional waves could propagate. The soil tube that was constructed was described in Ref. 3. One-dimensionality imposed the following requirements on the design of the tube:

(1) High radial stiffness to inhibit radial motion of the soil, and

(2) Low axial stiffness to allow the tube wall to move with the adjacent soil and not to retard the axial soil motion.

The tube was constructed of alternate rings of aluminum and neoprene rubber (Fig. A.1). The soil tube is composed of segments, each approximately 0.7 meters long. The segments were added on as the tube was filled with soil. In Fig. A.2, the column is shown at full height with its associated support structure. Buckling of the soil column is prevented by the "A" rings, which provide intermediate support to the column.

The capabilities and limitations of the soil column were discussed in Ref. 3 and 4. Specific points are:

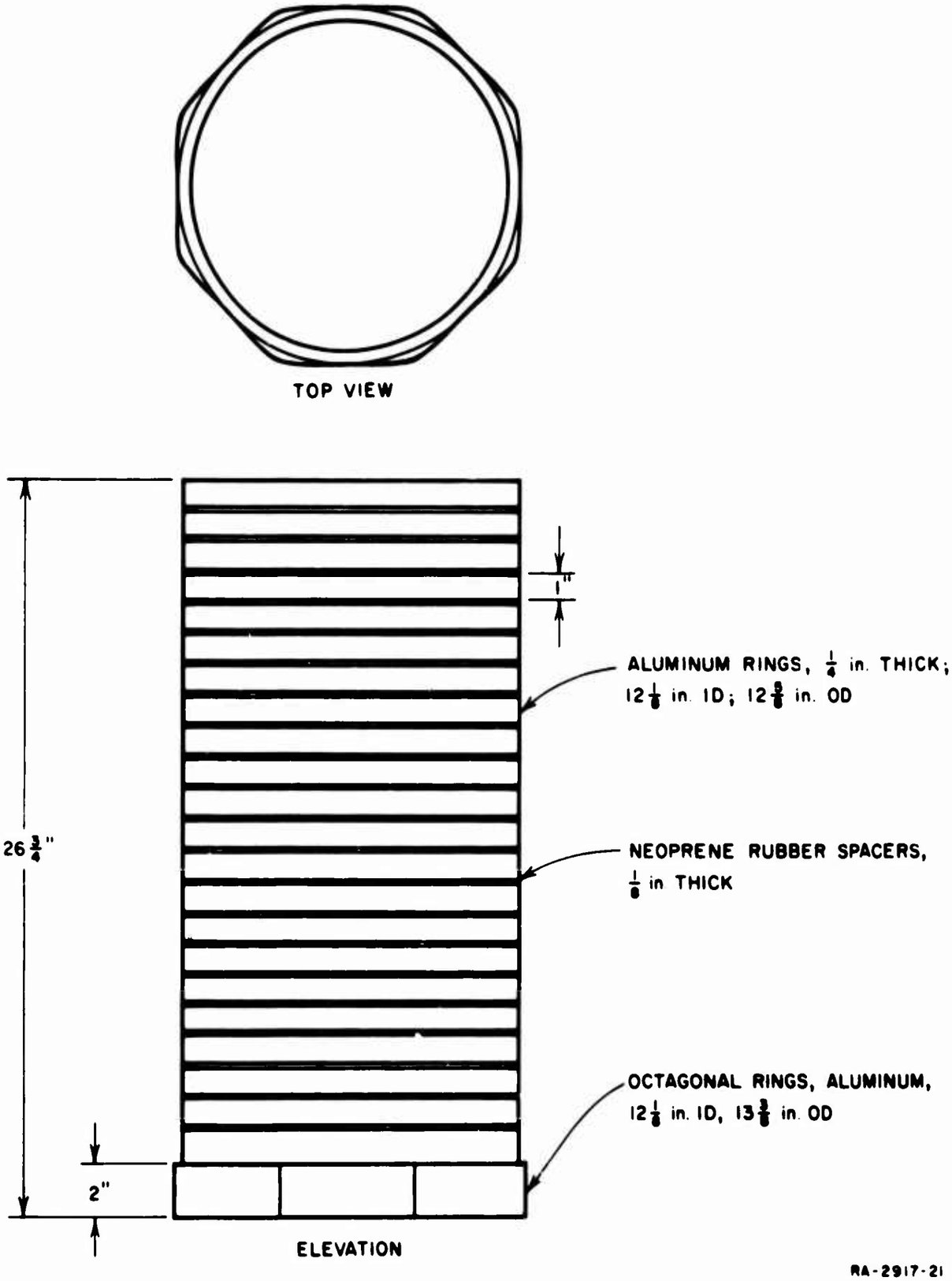

FIG. A.1 SOIL TUBE DESIGN

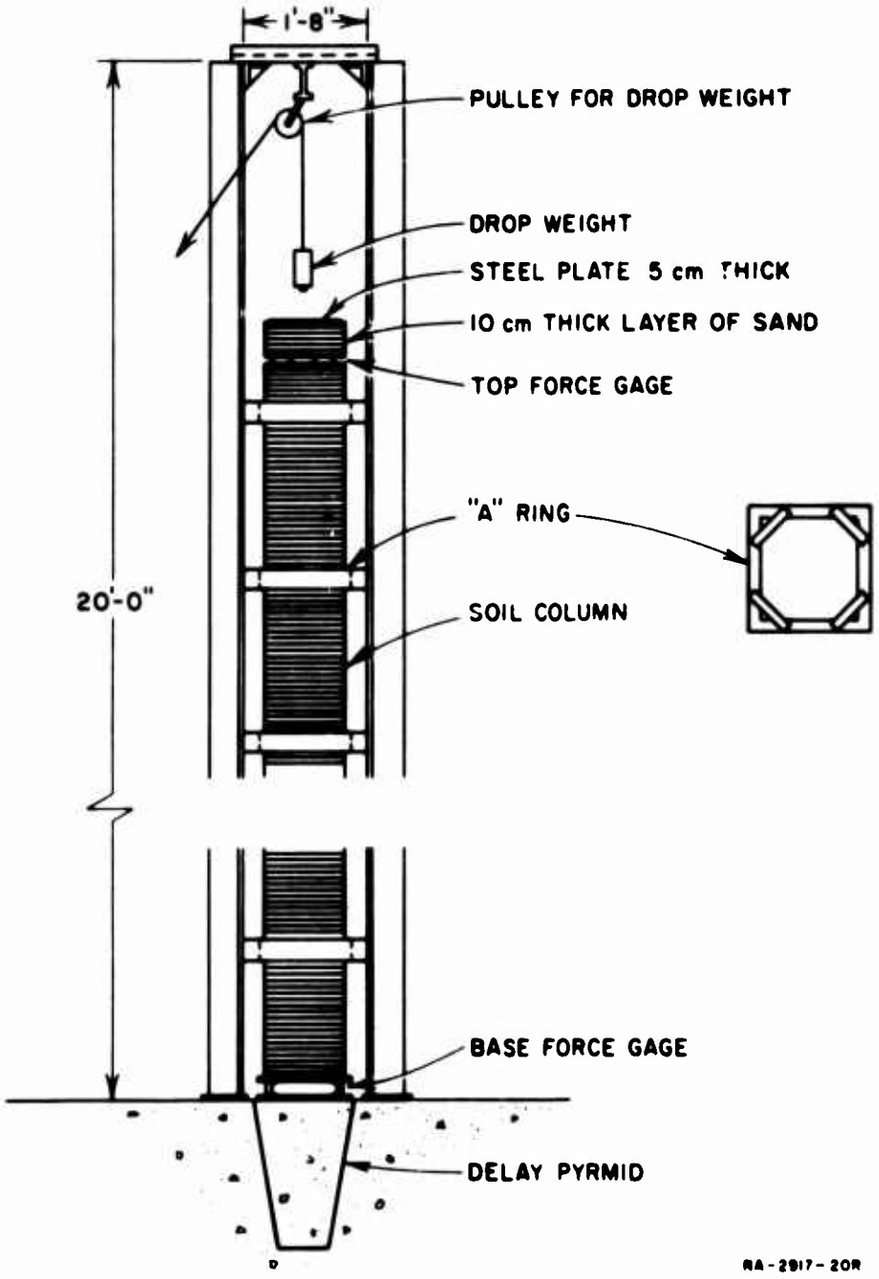

FIG. A.2 SOIL COLUMN SUPPORT STRUCTURE

(1) The radial stiffness of the tube is adequate to simulate a zero radial strain condition. With an axial pressure of 7 bars, the radial strain was only 100 microstrain (microinches/inch).

(2) The axial stiffness of the tube is about 56 bars and is thus small enough so that the tube absorbs less than 1% of the total applied force when the soil is a dense sand. For soil that is less stiff than the dense sand, the tube probably takes more than 1% of the total force.

Two types of stress gages, two types of force gages, and two types of accelerometers were used. The stress gages had been developed earlier and are described in Part IV. Drawings of these gages appear as Figs. A.3 and A.4.

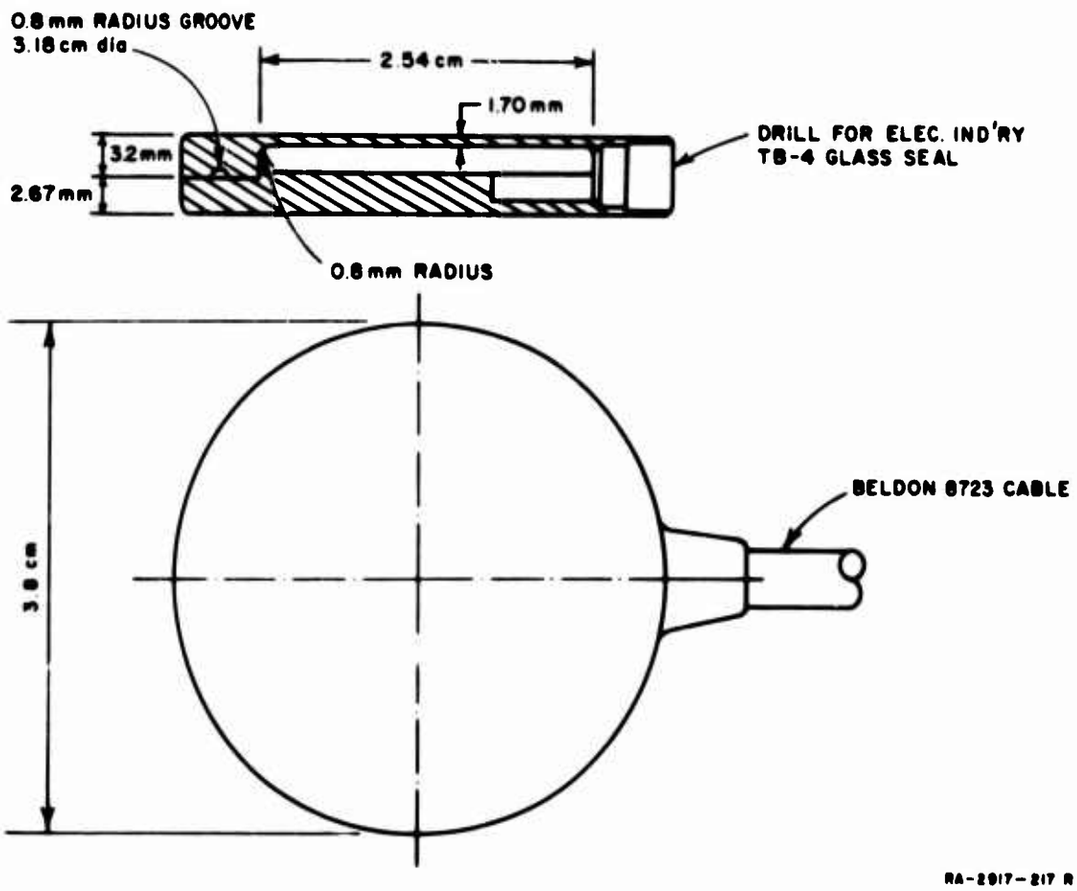

FIG. A.3 DIAPHRAGM STRESS GAGE

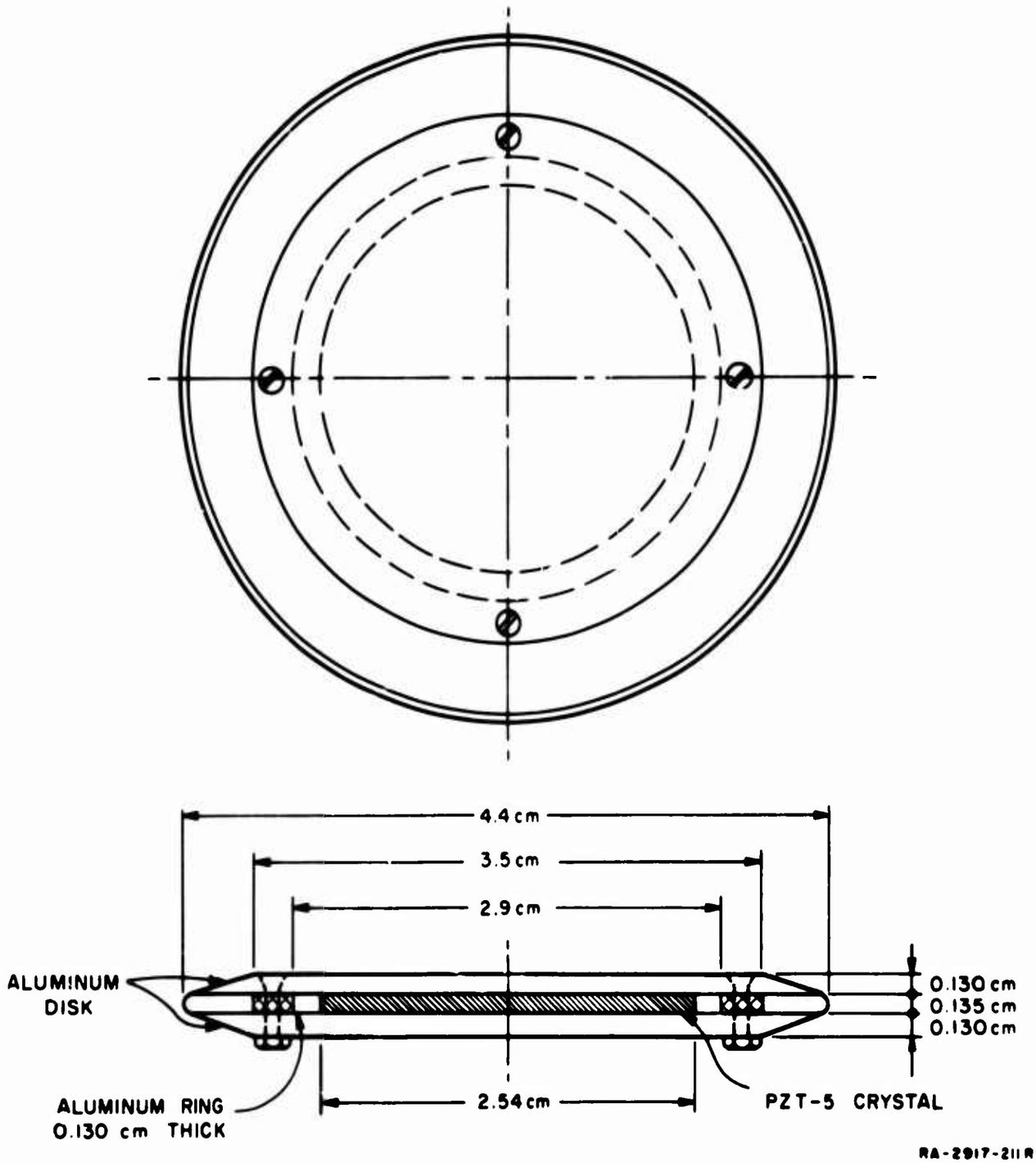

FIG. A.4 PIEZOELECTRIC STRESS GAGE

Of these two, the D gage is a hollow disk with a thin diaphragm on one side. This diaphragm was instrumented with four strain gages that formed a complete electrical resistance bridge. These gages were found to be very reliable and gave repeatable results. The other stress gage, the C gage, consists of a disk of piezoelectric material (PZT-5) sandwiched between two aluminum covering disks.

Two types of accelerometers were used, both made by Endevco. The type used near the top of the column is type 2261, which has a piezoresistive bridge as the sensing element. The other accelerometers were type 2221C and are piezoelectric. The piezoelectric gages were found to suffer significant zero shifts if they were shocked above 100 g; therefore, these gages were used deep in the column where the acceleration level was less than 100 g.

A force gage, which had been constructed for DASA at SRI under Contract 49-146-XZ-024, was used at the base of the column. This gage, designated S1, was designed as a surface shear gage but it also worked well as a total force gage. A photo of the gage appears as Fig. A.5 and is described more fully in Ref. 19.

The second type of force gage was constructed on the project for use at the top of the column and was numbered G1. This gage consists of three short columns between two aluminum disks (see Fig. A.6). The columns are aluminum tubes instrumented with four strain gages each to measure the force transmitted through the columns. Miscellaneous data on all six gage types are given in Table A.1.

The stress wave for all the tests was caused by dropping a large weight onto the top of the soil column. The stress waves produced by this mechanism closely resemble those from blasts--rapid rise to a peak and then a nearly exponential decrease. The drop-weights used are shown in Fig. A.7. The 21.5 and 49.2 kg weights had a steel striker ball that struck the heavy steel plate resting on the soil. The 21.5 kg weight was used for most of the tests. The 24.0 kg weight had a large curved plate on the base, and it was dropped directly onto the sand. The impact with this weight was much softer than the impact of the other weights

FIG. A.5 SURFACE SHEAR GAGE USED AS A FORCE GAGE

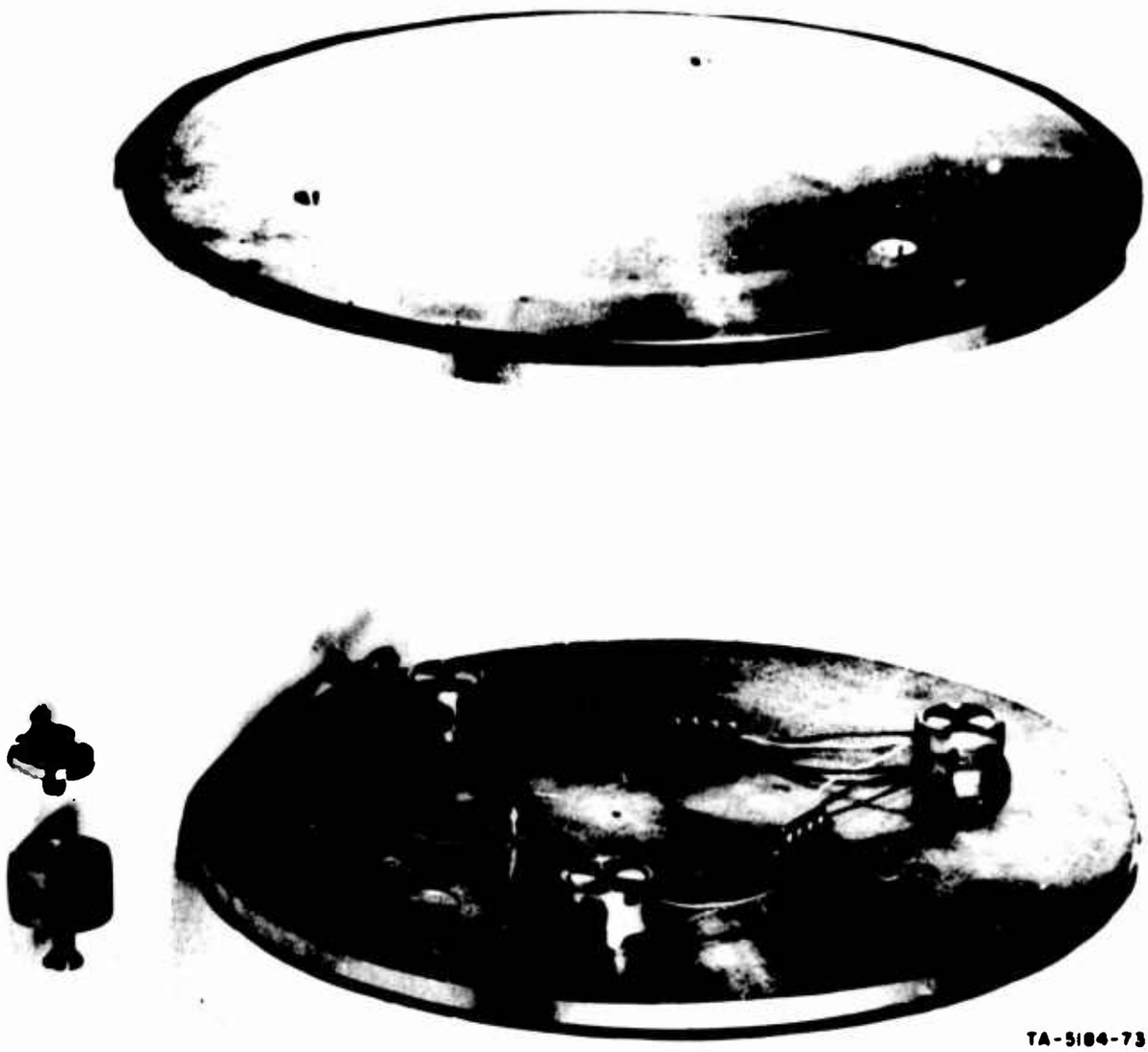

FIG. A.6 FORCE GAGE G1 WITH UPPER DISK REMOVED

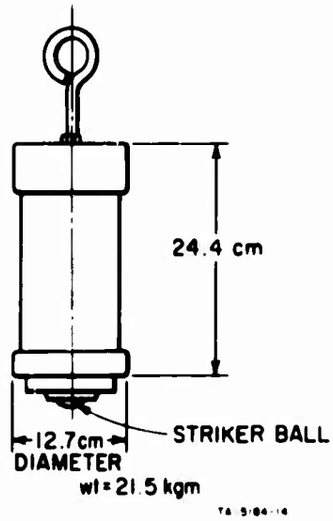

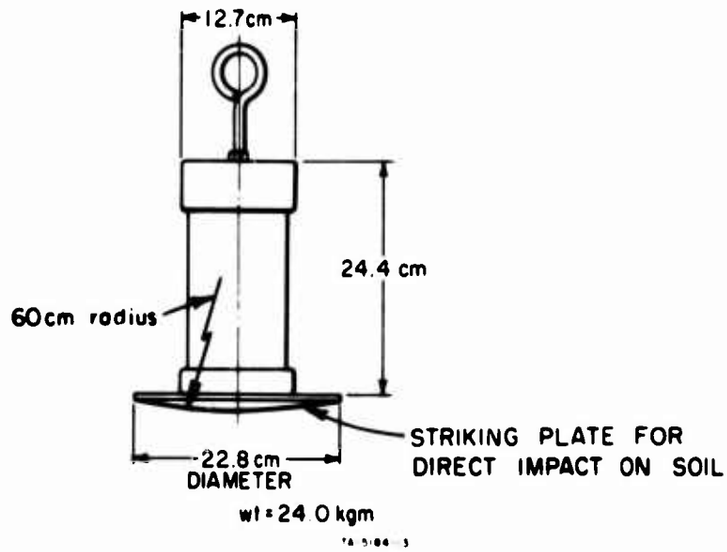

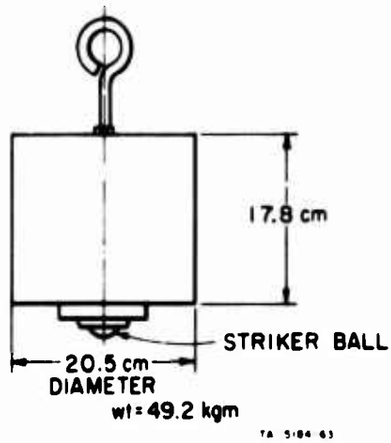

FIG. A.7 DROP-WEIGHTS

Table A.1

GAGE CHARACTERISTICS

Designation	Measurement	Sensor Type	Height x Diameter	Natural Freq.	Sensitivity[b]	Position during use
D	Stress	Strain Gage Bridge	0.59 cm x 3.8 cm	27 kc	1 mv/bar	upper half of column
C	Stress	Piezoelectric crystal	0.40 cm x 4.4 cm	[a]	1 v/bar	lower part of column
2261	Acceleration	Strain Gage Bridge	2.3 cm x 1.5 cm	40 kc	0.1 mv/g	upper half of column
2221C	Acceleration	Piezoelectric	0.8 cm x 1.5 cm	30 kc	14 mv/g	lower half of column
S1	Force	Strain Gage Bridge	7.6 cm x 30 cm (square)	2.6 kc	2 mv/# metric ton	base of column
G1	Force	Strain Gage Bridge	4.4 cm x 32.0 cm	[a]	2 mv/# metric ton	top of column

NOTES: [a] Natural frequency was not determined since it was well above the range of interest.

[b] Sensitivity for the strain gage bridge is listed on the basis of a 10-volt excitation.

and, consequently, the stress level was lower and the wave durations were longer. The weights did not appear to rebound on contact; therefore, the applied impulse was taken as the change in momentum that would just stop the weight. This impulse was computed as

$$I = \frac{M}{A}\sqrt{2gh}$$

where I is the impulse per unit area of the soil cross section,

M is the mass of the drop-weight,

A is the cross-sectional area of the soil column, and

h is the height of the drop.

The units of this impulse are bar-msec, the same as the area under the curve on a stress-time record. Hence, this impulse can be readily compared to the impulse measured at each force or stress gage.

A.3 Soil and Test Conditions

Soils used for the tests were a kaolinite clay, Vicksburg backswamp clay, and Monterey beach sand. Properties of these soils are given in Appendix B. Table A.2 lists the conditions of these soils as they were during the wave propagation tests.

Table A.2

TEST CONDITIONS

Column Designation	Soil Name[a]	Soil Placement: Compaction Method	Water[c] Content %	Dry Density gm/cm³	Saturation[d] %	Column height meters	Testing: Impulse[e] levels, bar-msec	Calibration Procedure
A	Kaolinite	Hand Tamping	34.7	1.29	88	2.58	14.0	Fluid
B	Kaolinite	Hand Tamping	31.7	1.34	88	4.62	6.1 to 14.1	Fluid
C	Kaolinite	Static[b] Pressure	18.8	1.42	60	4.35	7.0,10.0, 12.8	Static, Impulse
D	Vicksburg Clay	Pneumatic Tamper	26.8	1.34	71	4.48	7.0,9.9, 12.8	Static, Impulse
E	Monterey Sand	Sprinkle through Funnels	-	1.63	-	4.33	7.4,10.2, 13.0,30.8	Static, Impulse
F	Vicksburg Clay	Static[b] Pressure	24.4	1.52	81	4.27	7.5,10.2 13.1	Static, Impulse

[a] Kaolinite was purchased as a dry powder from L. H. Butcher Co., San Francisco. Vicksburg backswamp clay was provided by the U.S. Army Waterways Experiment Station, Vicksburg, Mississippi.

[b] Static compaction pressure was 17.0 bars for Column C and 5.7 bars for Column F.

[c] Average water content from samples taken during placement and during removal. The water content on removal was normally 1 to 2% less than the content at placement.

[d] Saturation calculations are based on a specific gravity of 2.60 for kaolinite and 2.70 for buckshot clay.

[e] The impulse of the dropped weight was calculated as in Equation A.1.

The clay used for the first three columns was a pure white kaolinite obtained commercially in an air dry condition. For Column A, the dry powdered clay was mixed with water to a water content of about 35%. This same clay was used in Column B in addition to some freshly mixed clay of about 33% water content. The soil for Column C was produced by mixing dry clay with the wet clay from Column B, producing a moisture content around 19%. The clay for Columns A and B was quite soft and so it was compacted by tamping it into place. The dryer soil for Column C had a granular appearance and was much stiffer. It was placed in the soil tube in 10 cm lifts; each lift was compacted with a jack to a static pressure of 17.0 bars.

The Vicksburg backswamp clay used in Columns D and F was mixed to a water content of about 28% at the Waterways Experiment Station and shipped to SRI. When it arrived, it was rather soft and sticky and tended to extrude through the column walls under static compacting pressure. Therefore, it was compacted with a seven-pound pneumatic tamper. Unfortunately, the compaction was neither uniform nor sufficient to produce a density comparable to that from a Standard Proctor test. For Column F, the soil was dried in small batches to a water content of about 24% (estimated by working the clay by hand), placed in the column in 10 cm lifts, and statically compacted with a hydraulic jack.

Column E was filled by raining Monterey sand through a double funnel device. This method of compacting sand has been described in Ref. 3.

The stress wave caused by the drop-weight traversed a layer of sand before reaching the force gage. Figure A.2 shows this layer of sand between the 5-cm thick steel plate and the force gage. The sand tended to smooth out the high frequency oscillations caused by the impact on the steel plate. Apparently, the sand caused some shocking up of the stress wave so that the rise time at the force gage is shorter than that at the top of the sand. In some tests, this sand layer did not adequately exclude the high frequency oscillations and so 1/4-in. of plywood and up to 1/4-in. of soft rubber were placed immediately under the 5-cm steel plate. The addition of these latter dissipative materials increased both the rise time and duration and rounded the wave form.

The stress level is roughly proportional to the applied impulse. Therefore, the stress level was varied by changing the drop weight and drop height. The range of impulse levels used is shown in Table A.2. Tests were generally conducted at three impulse levels so that the effect of stress level on attenuation and wave velocity could be studied.

Some typical characteristics of the applied stress waves are shown in Table A.3. Data for the table are taken from tests in which the 21.5 kg weight was used to produce an impulse of 12 to 14 bar-msec. The stiffness of the column clearly determines the stress level that can be obtained at a given impulse level: the peak stress for Column A, the

soft kaolinite, is much less than that for Column C in which the kaolinite was drier and denser. The wave durations also indicate that a sharper wave is transmitted in the drier, denser soil.

Table A.3

REPRESENTATIVE TEST RESULTS

Column	Test No.	Applied Impulse (bar-msec)	Peak Stress (bar)	Rise Time (msec)	Duration (msec)
A	10, 11	14.0	1.3	0.7	4.5
B	35 - 37	12.1	2.57	0.84	2.37
C	15 - 18	12.8	5.15	1.06	1.99
D	10 - 12	12.8	5.78	0.31	1.95
E	7 - 9	13.0	6.94	0.44	1.58
F	7 - 9	13.1	11.2	0.42	1.46

A.4 Calibration of Stress Gages

The stress gages used in the wave propagation tests were calibrated by

(1) Subjecting the gage to a fluid pressure while immersed in a fluid (fluid calibration),

(2) Pressurizing the column statically before and after the drop weight tests (static calibration), and

(3) Equating the impulse measured at each stress gage to the impulse measured at the top force gage (impulse calibration).

The fluid calibration procedure is easy to apply and may be justified if the soil is soft enough to act like a fluid. In most soils, the stress field about a gage will not be as uniform as it would be in a fluid, and the gage will tend to over or under-register. If all the gages over-register to the same extent, the stress level will be unknown but the rate of attenuation can be found.

For the static calibration, a force was applied to the top of the soil column with the same jack with which some of the soils were compacted. The calibration was made before and after testing, and the

average was used as the static calibration. Samples of these results are shown in Fig. A.8, along with the fluid calibrations of the gages. The gage at the shallow depth over-registered considerably, while the deeper gage under-registered at the higher stress levels.

The impulse calibration is based on the fact that the impulse of the initial wave is the same at all depths. In this case, the calibration and the test were made simultaneously. That the impulse does not vary with depth can be shown with reference to Fig. A.9. This figure exhibits a column with a cross-sectional area of unity and an isolated mass of soil, M, between the measuring stations. When an impulse is applied to the column, forces are transmitted to M, causing it to move with velocity, v.

$$\sigma_1 - \sigma_2 = M\frac{dv}{dt} \qquad (A.2)$$

When this equation is integrated with respect to time, the result is

$$\int_{t_1}^{t_2} \sigma_1 \, dt - \int_{t_1}^{t_2} \sigma_2 \, dt = \int_{t_1}^{t_2} M\frac{dv}{dt} \, dt = M(v_2 - v_1) \qquad (A.3)$$

where v_1 and v_2 are particle velocities at times t_1 and t_2, respectively. Now, t_1 is chosen before the arrival of the stress wave and t_2 is chosen long after the passage of the wave so that all motions of the soil mass have returned to zero. For this case, v_1 and v_2 are zero, and

$$\int_{t_1}^{t_2} \sigma_1 \, dt = \int_{t_1}^{t_2} \sigma_2 \, dt \qquad (A.4)$$

These integrals define an impulse (actually, impulse divided by cross-sectional area of the column). Because of the equality (Eq. A.4), the impulses measured at all levels are equal and are equal to the impulse applied at the top.

In practice, t_2 was limited to the length of the stress-time record obtained. The particle velocity at t_2 was not known but was assumed to be approximately zero since the stress was nearly zero at that time.

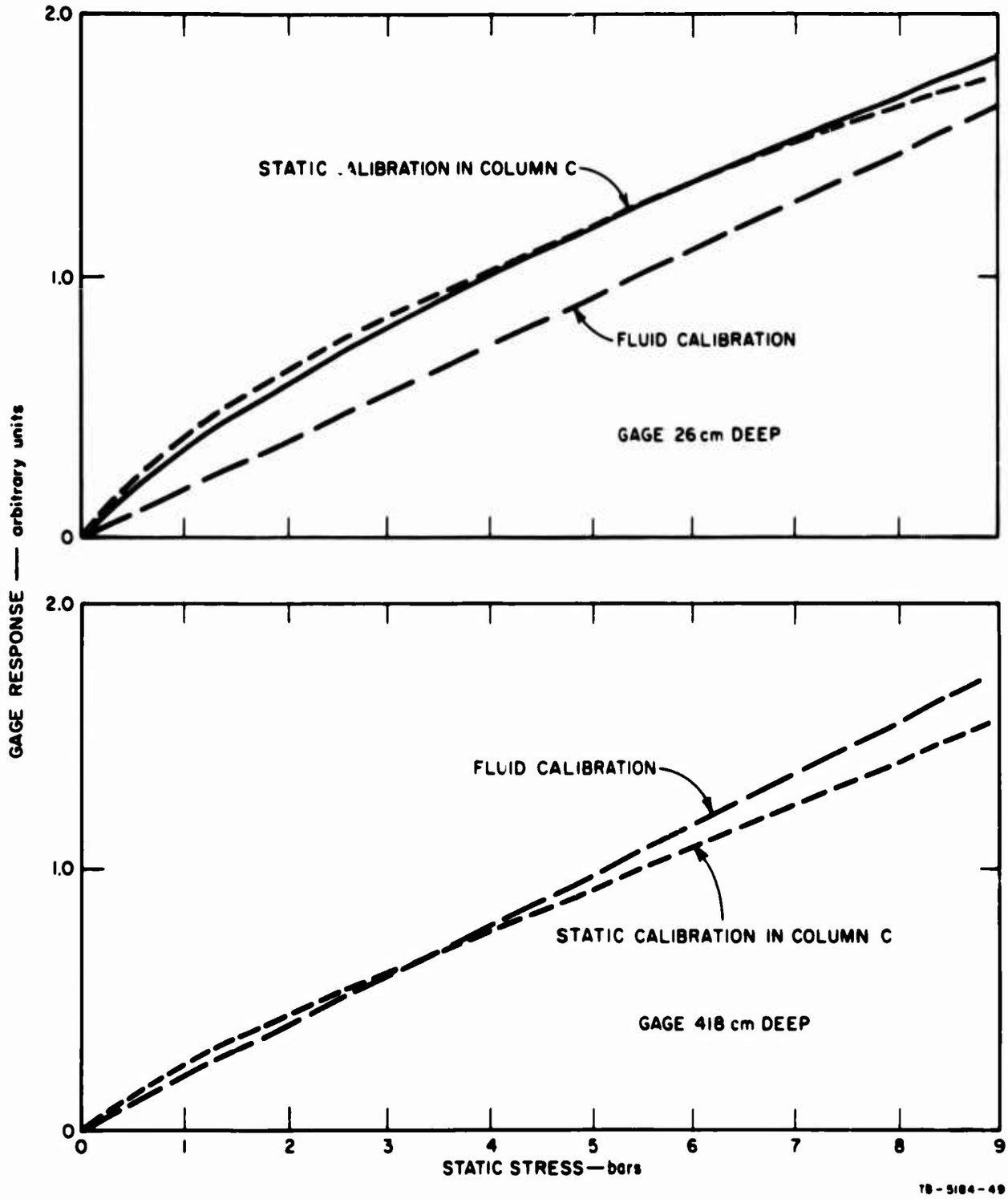

FIG. A.8 STATIC CALIBRATION OF TWO DIAPHRAGM STRESS GAGES

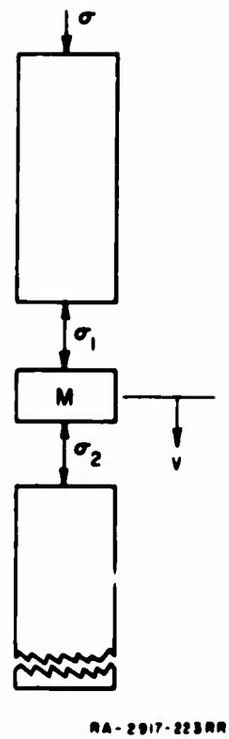

FIG. A.9 STRESSES IN THE COLUMN

The area under the stress-time curve was equated to the applied impulse in order to obtain the calibration constant for the stress record.

As shown in Table A.2, the fluid calibration procedure was used for the first two columns. Thereafter, the static calibration was used. In each of these cases, the impulse calibration was used as a check. The impulse calibration gave stresses within ±10% of those calculated with the static calibration. Therefore, the static calibration was assumed to be adequate.

BLANK PAGE

NOTATION FOR APPENDIX B

c = wave velocity (meters/sec)

E = spring constants for viscoelastic compacting models, (bars)

E_0 = spring constant of series spring, loading

E_1 = spring constant of parallel spring, loading

M = a modulus (bars)

t = time

t_ℓ = $t - \pi/\omega$, the lag time between peak stress and peak strain

t_w = half the duration of the loading pulse, see Fig. B.11

α = $(1 - E_0/E_1)/(1 + E_0/E_1)$, compacting dissipative parameter

δ = viscous dissipative parameter used with the constant tan delta model

ϵ = strain

ϵ_{1_d} = strain difference shown in Fig. B.11

ϵ_{2_d} = strain difference shown in Fig. B.11

η = viscosity of dashpot of viscoelastic compacting model, (bar-msec)

θ_1 = slope of loading stress-strain curve

θ_2 = slope of unloading stress-strain curve

ρ = density (gm/cm^3)

σ = stress, (bars)

σ_0 = peak applied stress

σ_1 = peak unloading stress, see Fig. B.13

ω = natural circular frequency (rad/sec)

Appendix B

SOIL PROPERTIES

B.1 Introduction

To generate a prediction for wave propagation phenomena, detailed information on certain soil properties is needed. In this appendix the procedure and equipment used for obtaining these properties are described and the data on the tested soils are listed. In add tion, the ordinary soil properties that are used to classify and characterize soils are given. These ordinary properties are shown in Table B.1. More data on the compaction characteristics of the Vicksburg backswamp clay were given by Jackson and Hadala.[20] The grain size distribution for the Monterey sand is shown in Fig. B.1. The sand is evidently somewhat less uniform than that previously used on this project.

Table B.1

GENERAL SOIL PROPERTIES

Type	Specific Gravity	Liquid Limit (%)	Plastic Limit (%)	Minimum Density grams/cm^3	Maximum Density grams/cm^3	Description
Kaolinite Clay	2.60	49	35	-	-	White, obtained as a dry powder, very sticky when wet.
Buckshot Clay	2.70	60	23	-	-	Brown, sticky, contains organic material.
Monterey Sand	2.62	-	-	1.41	1.66	Clean, dry, subangular sand, finer than 30 mesh.

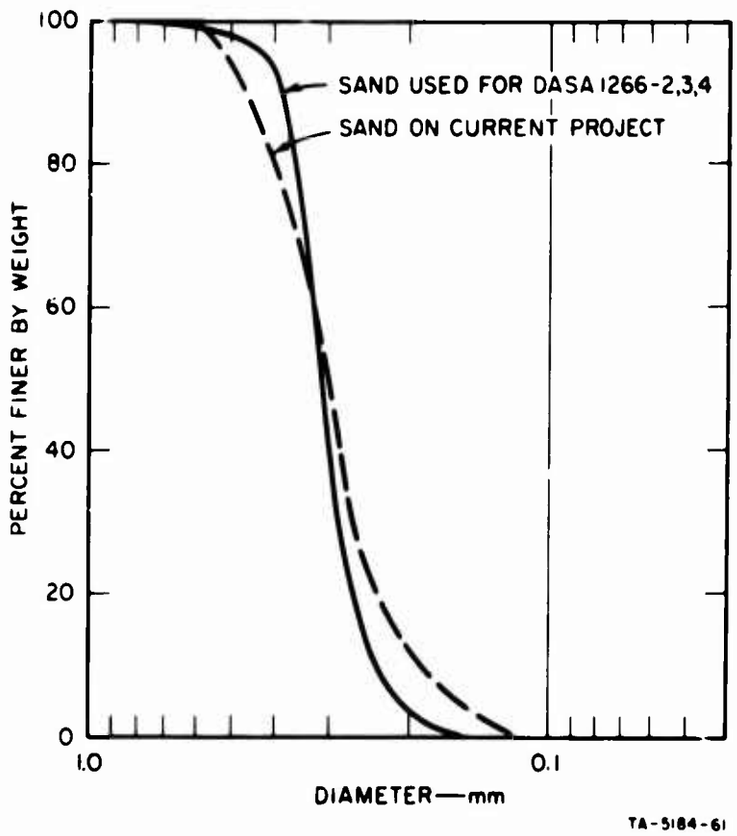

FIG. B.1 GRAIN SIZE DISTRIBUTION FOR MONTEREY SAND

B.2 The MIT One-Dimensional Soil Tester

Specific information about dynamic moduli, frictional behavior, and viscous dissipation is needed in order to predict the nature of wave propagation in a soil. These properties can all be determined from appropriate dynamic tests on small samples of the soil if the confinement conditions of the soil are the same as those which obtain during wave propagation. The type of test that was used is one in which a pressure is applied rapidly to the soil sample and then released. An appropriate loading function is shown in Fig. B.2. The primary result from the test is a plot of stress versus strain during loading and unloading (see Fig. B.3). Moduli of the soil appear as slopes of the curves and, hence, can be determined from the plot. The frictional and viscous dissipation parameters can also be determined from this plot if the proper type of dissipation mechanism is known or assumed.

UPPER TRACE: STRAIN 500 microstrain/cm
LOWER TRACE: STRESS 20 psi/cm
SWEEP: 5 msec/cm

FIG. B.2 LOADING FUNCTION FOR COMPRESSION TESTS

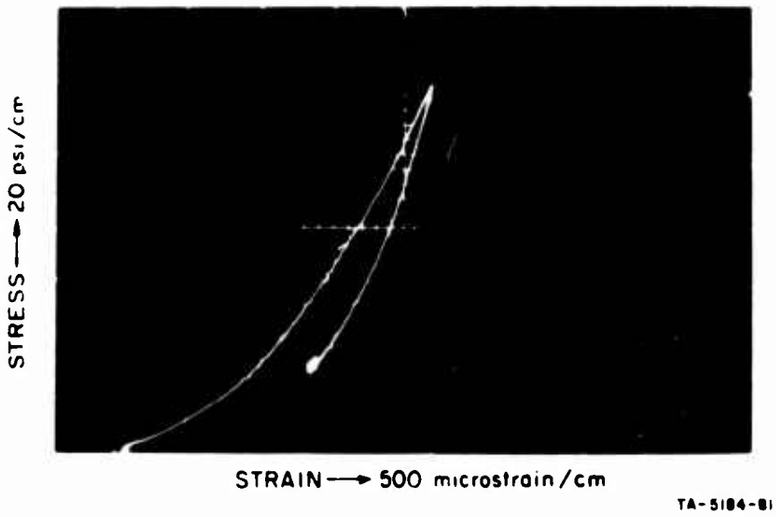

FIG. B.3 TYPICAL STRESS-STRAIN CURVE
FROM DYNAMIC COMPRESSION TESTS

A modification of a device developed at the Massachusetts Institute of Technology for making dynamic one-dimensional soil tests was used on this project. The modified tester (see Fig. B.4) is composed mainly of two heavy, stainless steel disks. The small cavity in the lower one holds the soil. The chamber above the soil, separated by a membrane from the soil is filled with a light oil. The soil is stressed by pressurizing the oil, either from an external source through the pressure port or by depressing the plunger. The follower disk lies directly atop the soil and follows the motion of the soil during testing. A rod connects the follower disk to the core of an L.V.D.T. (linear variable differential transformer), which monitors the core motion, and thus the soil strain The stress on the soil is equal to the pressure in the upper chamber; this pressure is monitored by a diaphragm-type pressure transducer.

The lateral strain of the soil during testing is quite low because of the great stiffness of the confining disks. No measurements of lateral strain were made but it was estimated that the strain was less than 2 microstrain at a pressure of 7 bars. This strain is much less than the 100 microstrain expansion of the soil column tube.

To determine the effect of expansion of the tester on the strain measurements, the tester was assembled without a sample and with the strain measuring rod screwed into the bottom of the sample chamber. Any strain measured in the configuration is a false indication of soil strain; hence, this test provided a measure of the inaccuracy of the strain obtained during soil tests. The tester was then subjected to a 150 psi pressure pulse; the resulting core motion corresponded to an apparent sample strain of 60 microstrain. This strain gives a modulus of 2.5×10^6 psi for the tester. The highest moduli measured on the clay was 1000 bars (15,000 psi) and on the sand 4800 bars (70,000 psi). Hence, the flexibility of the tester does not add a significant error to the soil modulus measurement.

B.3 Test Procedure

A soil sample was selected from the material tested in the column. For clays, the sample was trimmed so that its weight would give the required density when it was compacted into the soil chamber in the

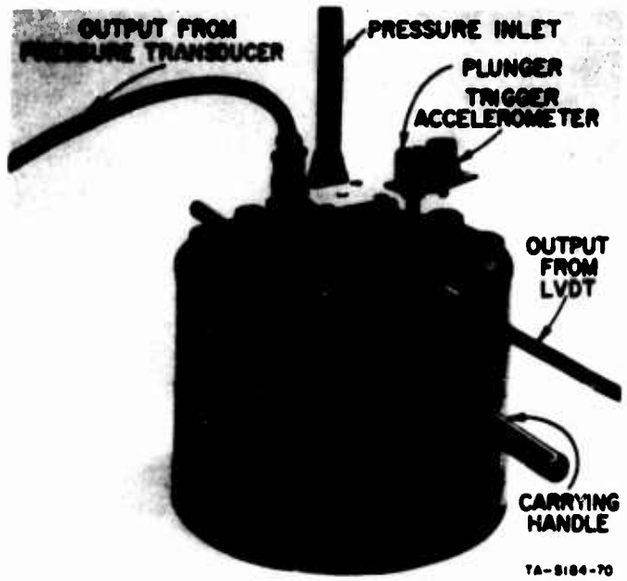

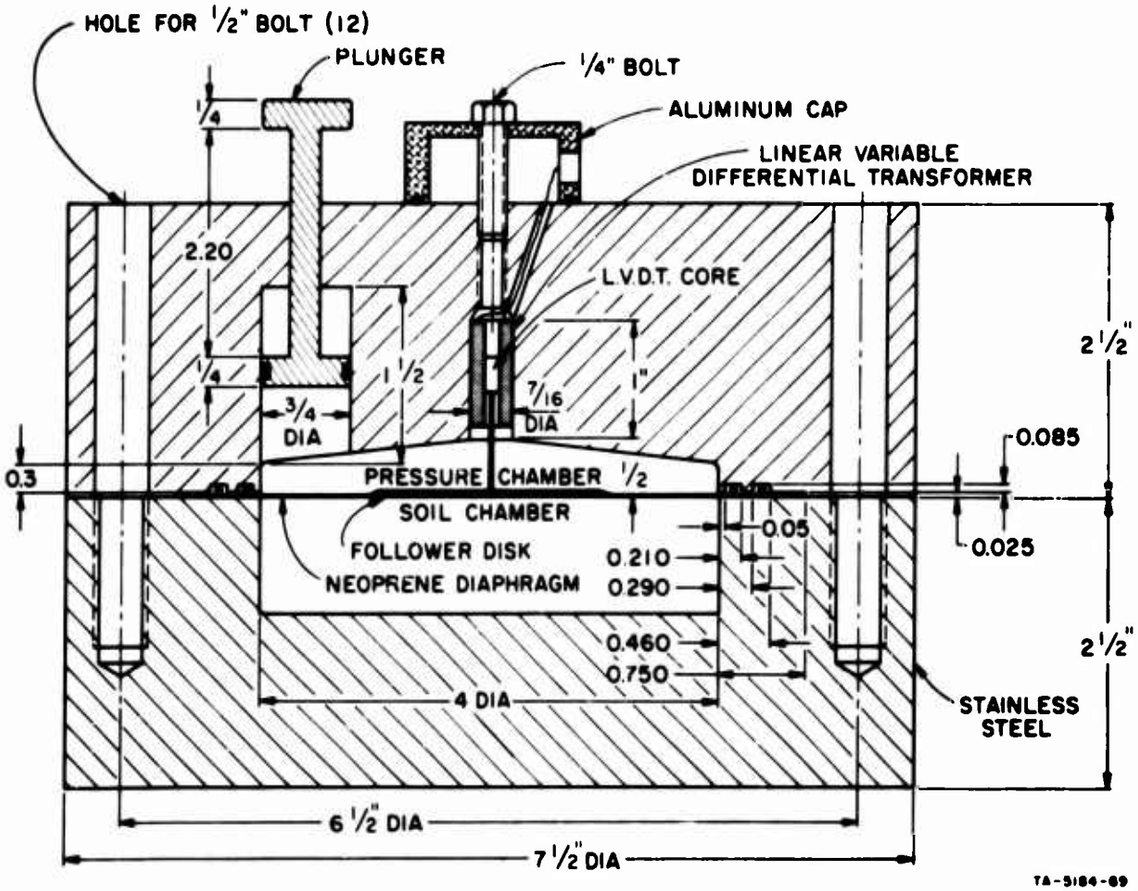

FIG. B.4 MIT DYNAMIC ONE-DIMENSIONAL SOIL TESTER

tester. It was compacted by tamping and then consolidated under a static preload of 10.5 bars. Sand samples were placed by sprinkling the sand through a series of screens from a height of about 30 cm.

The system for applying pressure to the soil is shown schematically in Fig. B.5. The dynamic pressure source is a charged accumulator, a large steel bottle with a diaphragm separating oil and air chambers. Dynamic pressures were applied by opening the dump valve suddenly. Preloads were applied with the hydraulic hand pump. The bleed valves were used to evacuate air trapped in the system, and the throttle valve was used to slow the dynamic pressure rise and, thus, to damp out oscillations.

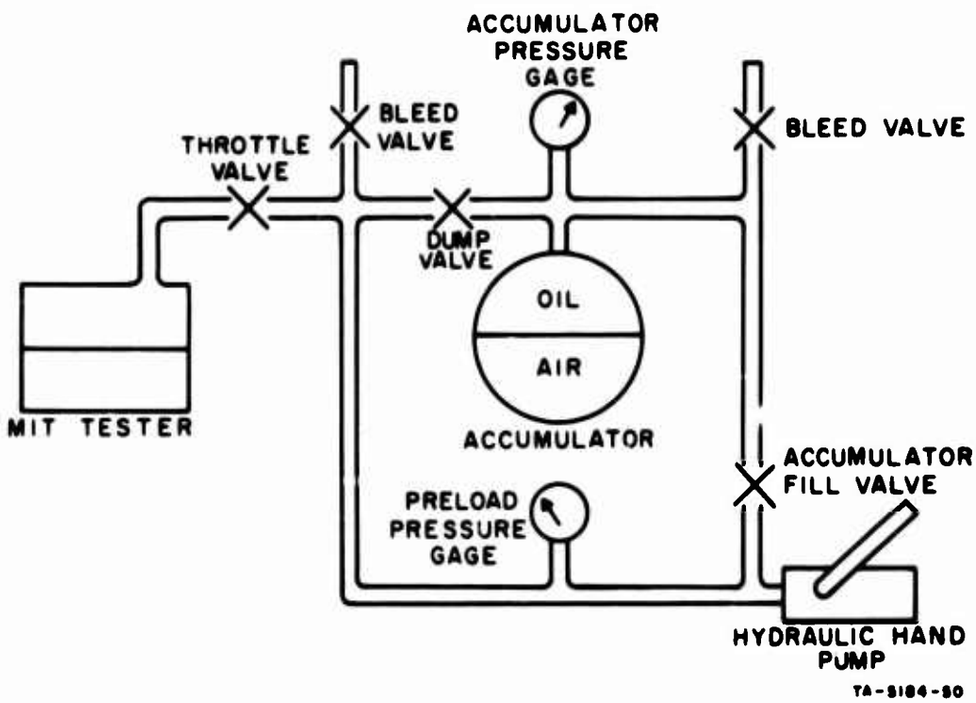

FIG. B.5 SCHEMATIC LAYOUT FOR PRESSURE SYSTEM FOR MIT TESTER

Two oscilloscopes were used to display the data from the test fixture: One displayed the stress and strain as functions of time (Tektronix 502A), and the other displayed stress versus strain (Tektronix 535). The Tektronix 535 was modified so that strain controlled the horizontal deflection of the oscilloscope beam, while the time base determined how

long the beam would be unblanked. The trigger signal went to Time Base B, was delayed, and then triggered Time Base A. The beam then became unblanked. After a time interval governed by the setting of Time Base A, the beam was blanked again. With this system, the stress-strain curve was obtained just during the time of interest: from start of loading to the completion of the first unloading.

B.4 Presentation of Data

Tests were performed at five preload levels for each of three peak stress levels in order to get a complete picture of the variation of modulus and the dissipation parameters with stress level. The stress-strain curves that were obtained are grouped in Figs. B.6 through B.10.

Several interesting features may be noted in these curves. All loading curves, except those from sample 3, are concave upward and thus appear to be stiffening with increasing stress. While the loading stress-strain curves for No. 3 are essentially linear, the unloading curves are not; therefore, no linear elastic behavior can be expected.

There are many minor irregularities in the stress-strain curves caused by oscillations in the pressure, and they should not be attributed to an anomalous soil behavior. These oscillations occurred only at low dynamic stress and at low preload levels. They may have been caused by the presence of air in the pressure chamber.

Preload seeems to have no effect on the stress-strain curve for the kaolinite samples. That is, on a plot of total stress (preload plus dynamic increment) versus total strain, all the curves would approximately coincide. For the Vicksburg clay this was not the case becuase there seemed to be a continuing compaction throughout the test program. Later tests always gave evidence of stiffer soil than earlier tests. The curves for sand show a small initial hump, which grows in importance with preload level. The hump has been noted before and studied in detail by Moore.[21]

On many of the stress-strain curves, the maximum strain does not coincide with the maximum stress. In such a case the tangent to the unloading curve at the peak stress is vertical or slightly negative.

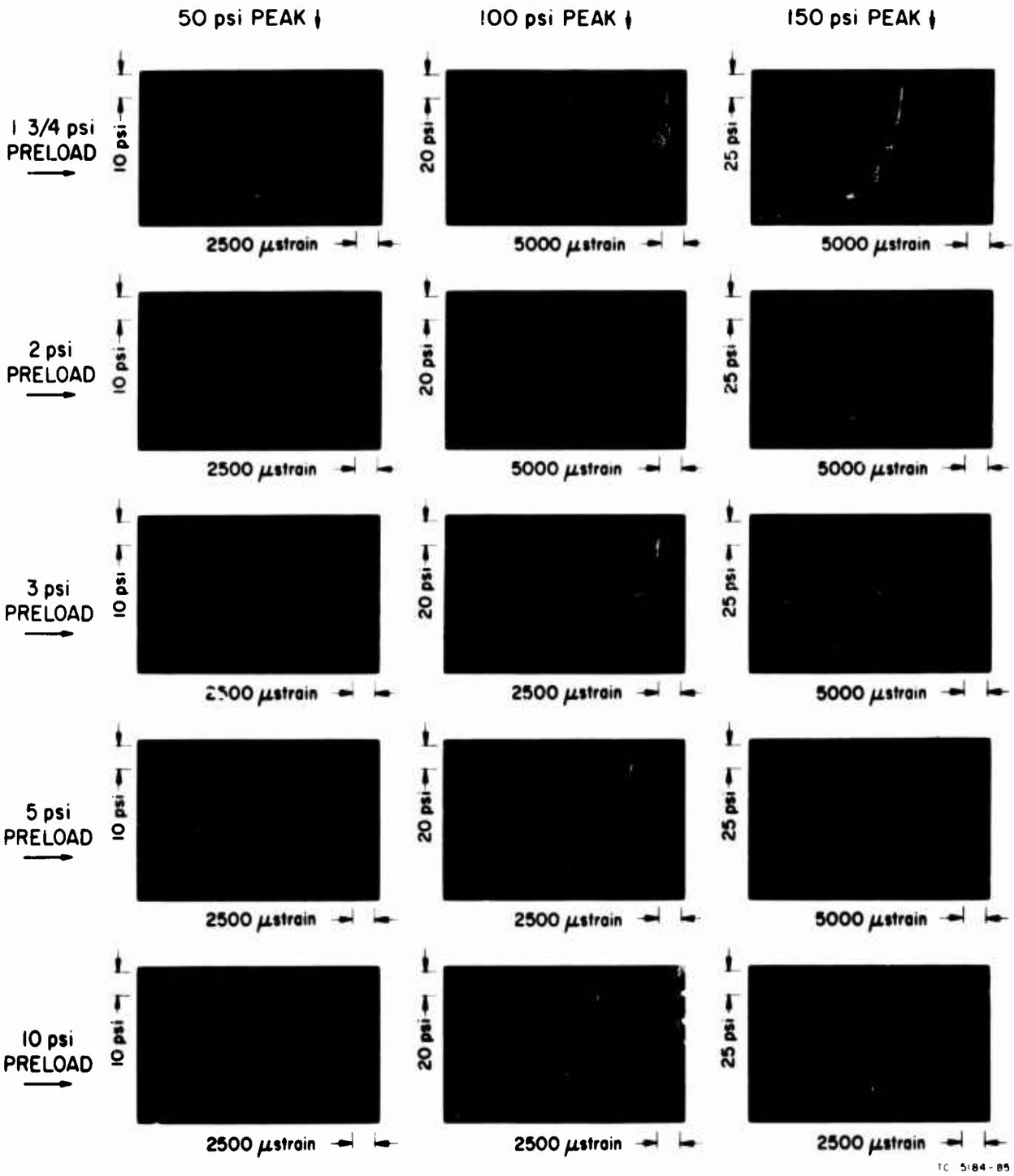

FIG. B.6 STRESS-STRAIN CURVES: SAMPLE 1, KAOLINITE

Testing Order: 150 psi peak and 10 psi preload,
150 psi peak and 5 psi preload, ...
100 psi peak and 10 psi preload, ...
50 psi peak and 1¾ psi preload.

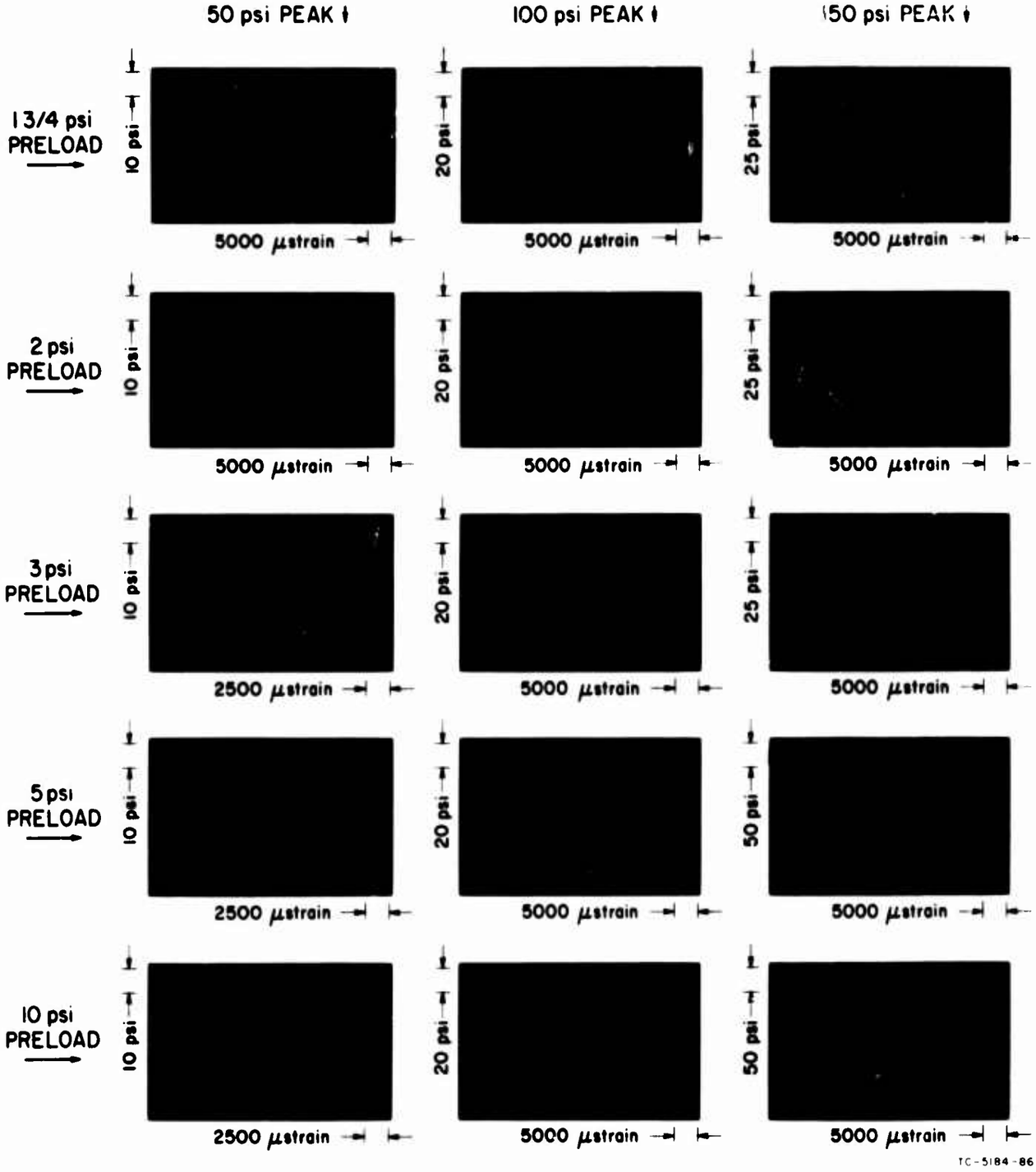

FIG. B.7 STRESS-STRAIN CURVES: SAMPLE 2, KAOLINITE

Testing order as in Fig. B.6

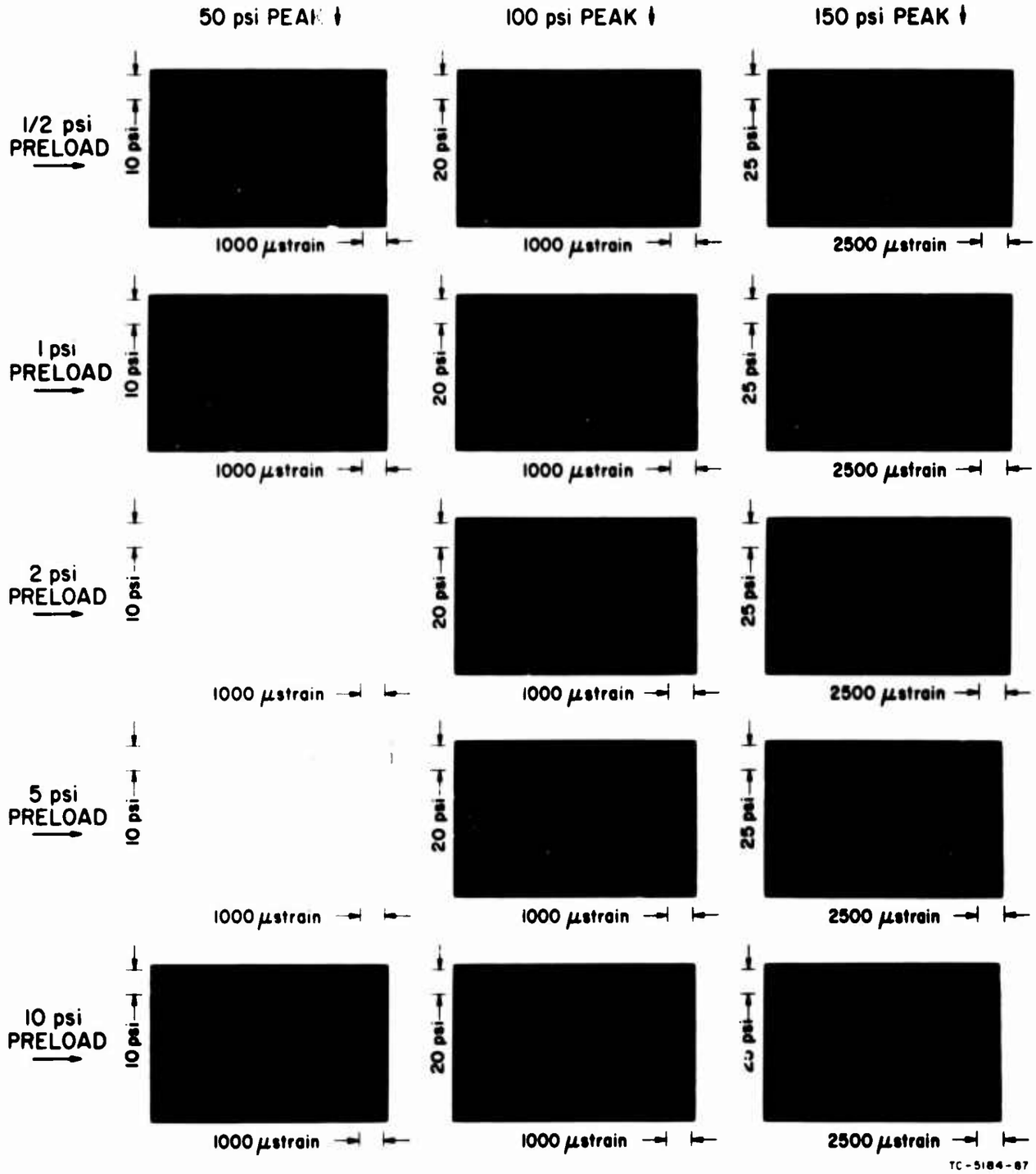

FIG. B.8 STRESS-STRAIN CURVES: SAMPLE 3, KAOLINITE

Testing order as in Fig. B.6

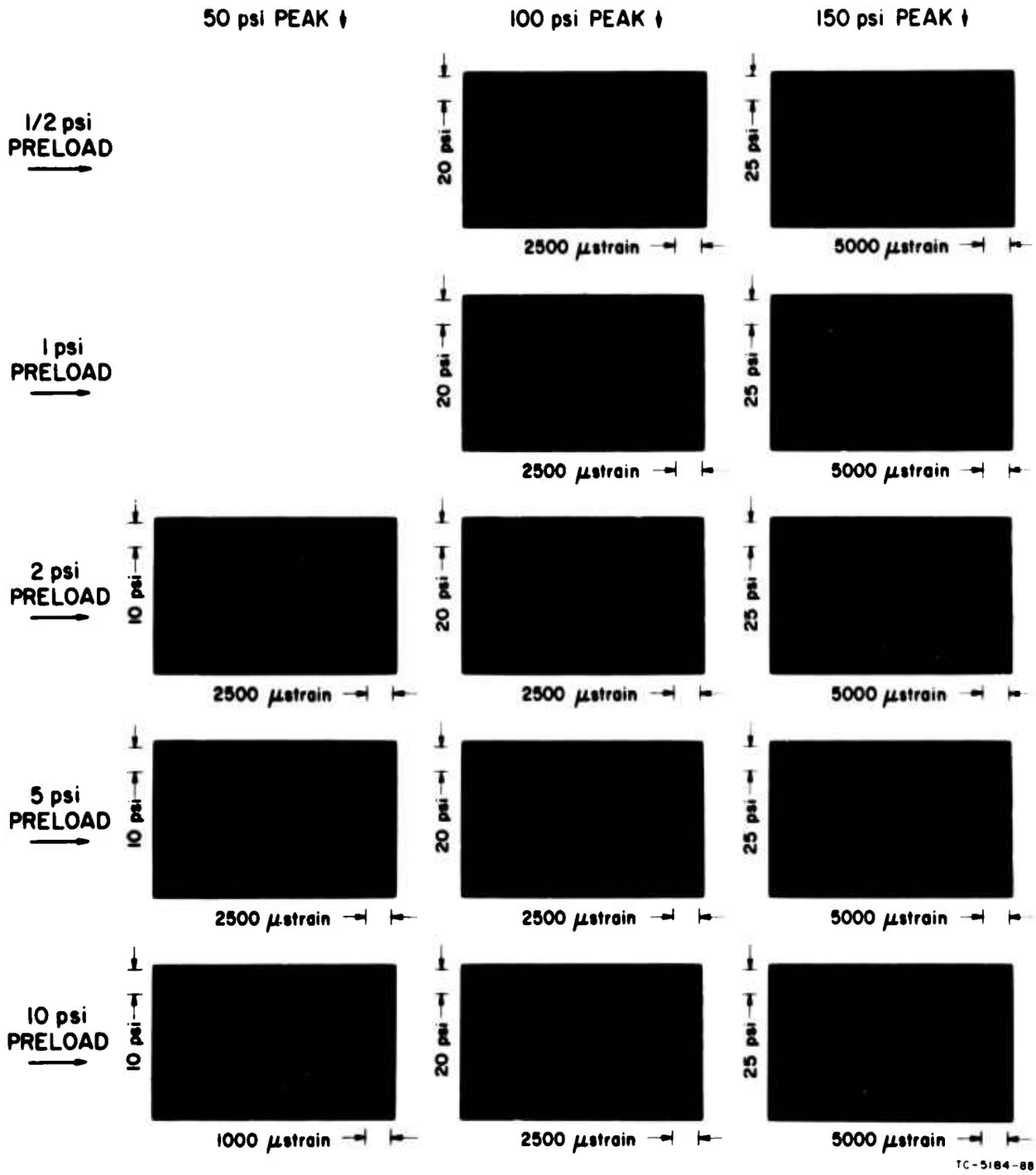

FIG. B.9 STRESS-STRAIN CURVES: SAMPLE Δ VICKSBURG CLAY

Testing order as in Fig. B.6

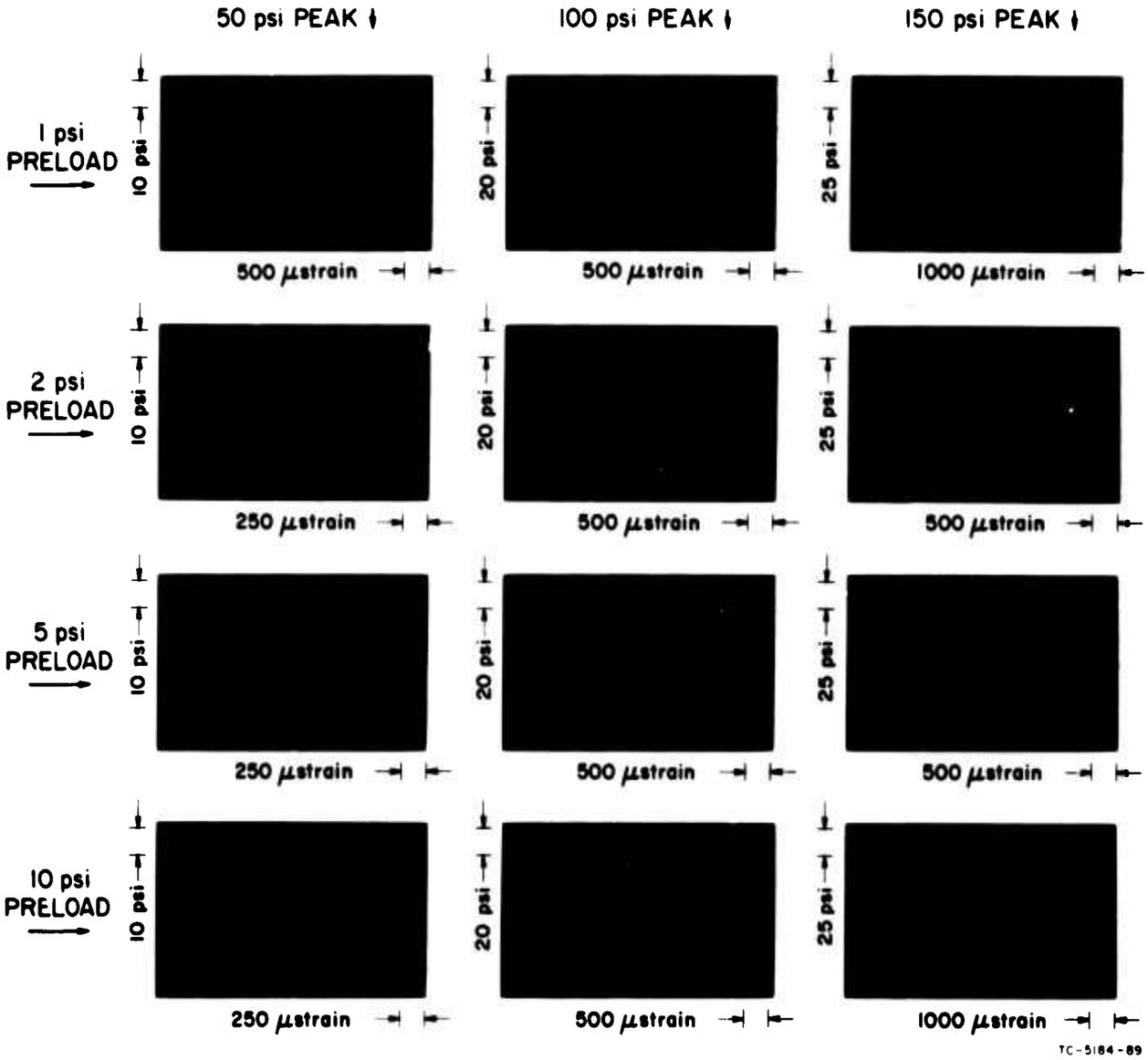

FIG. B.10 STRESS-STRAIN CURVES: SAMPLE 5, MONTEREY SAND

Testing order as in Fig. B.6

The lag of the strain behind the stress is more clearly shown in illustrations, such as Figs. B.2 and B.11 in which both stress and strain are recorded as functions of time.

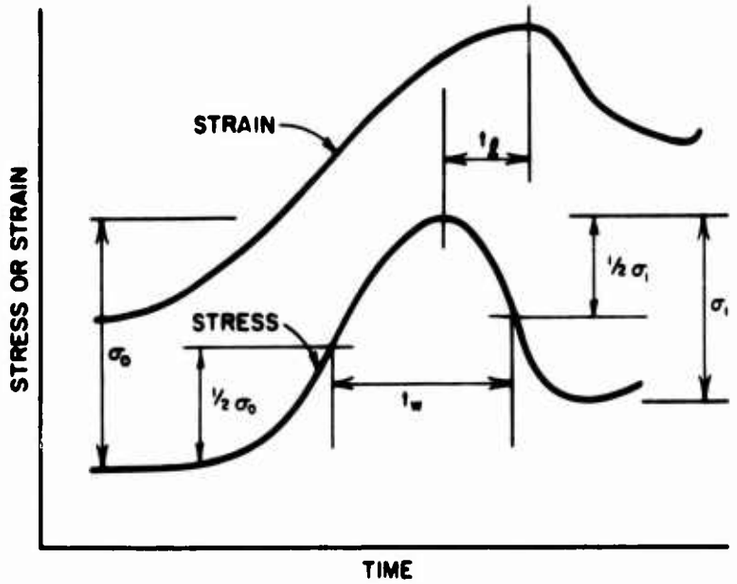

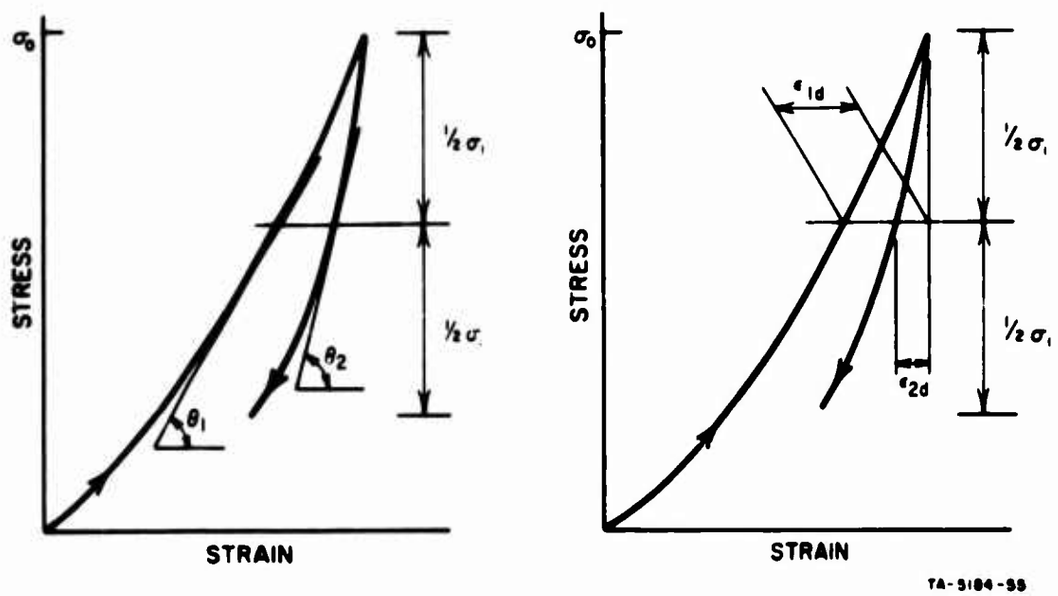

FIG. B.11 MEASURED POINTS ON THE COMPRESSION TEST DATA

B.5 Data Reduction: Dissipation Parameters

The data from the MIT tester can provide information on (1) dissipation parameters of the soil, and (2) moduli from which wave velocities are obtained. In each case, the soil data was reduced on the assumption that the soil can be approximated by the linear hysteretic model, the viscoelastic compacting model, or the constant tan delta model. No attempt was made to formulate a model that would actually duplicate the behavior of the soil during the compression test. The dissipation parameters are considered first.

The stress-strain data in Figs. B.6 to B.10 suggest that both compacting and viscous dissipation exist in the soil. Compaction here refers to the tendency of the material to show some permanent set after a loading and unloading cycle. Viscosity is exhibited when the maximum strain occurs later than the peak stress, that is, during the unloading portion of the stress-strain curve.

The dissipation parameter for the soil was determined from measurements taken from the stress-strain curves and from the stress-time and strain-time curves.

The reduction was accomplished by comparing certain features of the experimental curves with corresponding features derived from an analysis of the models. The features to be considered were (1) the slopes of the stress-strain curves at midheight, (2) the lag time between the occurrence of peak stress and peak strain, and (3) the width of the loop formed between the loading and unloading stress-strain curves (Fig. B.11).

The first measurement was used to define the viscoelastic parameter for the viscoelastic compacting model, the second, to define the compacting parameter for the viscoelastic compacting and the linear hysteretic models, and the third, to find tan δ for the constant tan delta model.

The analysis of the viscoelastic compacting model to a pressure pulse which is given in Section C.5 is the basis for the determination of the parameters for that model. The viscoelastic parameter, η, was determined graphically from Fig. C.7. Then the compacting dissipative

parameter, α, was found from an iterative solution of Eq. C.41 and then C.32. This data reduction scheme for the viscoelastic and compacting parameters was applied to the records from the soil samples tested in the MIT tester. The basic data—lag time, slopes of the curves, and natural frequency of loading—were measured on the stress-strain, stress-time and strain-time records obtained during the tests. The lag time, t_ℓ was measured as the time difference between the peaks on the stress-time and strain-time records (Fig. B.11). The slope of the stress-strain curves were measured with a drafting machine. The loading frequency, ω, was taken as π/t_w, where t_w is half the duration of the loading as shown in Fig. B.11. These measured data and the dissipative parameters obtained from the data reduction scheme are listed in Table B.2.

DISSIPATION PROPERTIES OF THE SOILS

Table B.2

Sample No.	Soil	Water Content (f)	Dry Density (gm/cm³)	Pressure Level psi	Lag Time, t_ℓ	E_1/E_0	η/E_0 (msec)	α	Tan ϕ on width of loop	Used for Predictions: Pertaining to Column	E_1/E_0	η/E_0 (msec)	α	Tan ϕ	c (m/sec)
1	Kaolinite	38.0	1.24	50	0	-	-	.045	.130	-					
				100	.240	2.13	10.9	.025	.155						
				150	.325	1.43	6.67	.038	.164						
2	Kaolinite	33.3	1.36	50	.264	2.20	31.0	.016	.162	A, B	2.0	30	.02	.30	100
				100	.292	1.77	16.0	.023	.213						
				150	.377	1.19	8.4	.056	.275						
3	Kaolinite	18.3	1.34	50	.305	1.87	15.2	.148	.388	C	2.0	15	.15	.30	240
				100	.252	2.34	13.5	.223	.385						
				150	.207	3.15	16.0	.212	.385						
4	Backswamp	26.3	-	50	.332	1.61	20.9	.083	.233	D, F	1.7	20	.09	.30	340
				100	.254	2.18	16.3	.110	.294						
				150	.313	1.37	8.0	.117	.328						
5	Sand	-	1.66	50	.139	4.62	23.3	.134	.209	E	5.0	22	.12	.12	500
				100	.103	6.48	22.2	.117	.248						
				150	.124	5.52	19.1	.092	.220						

None of the various parameters appear to be constant but rather vary with the pressure level used. Certain trends may be noted in the Table: α appears to increase with stress level for the clays but to decrease for the sand. The viscous parameter, η/E_0, appears to decrease as stress increases for the softer soils but to remain constant for the drier, stiffer soils. Whitman[16] has suggested that E_1/E_0 should be about 1 for soft clays and 4 for sands. This prediction agrees quite well with the tabulated values.

The linear hysteretic model is a special case of the viscoelastic compacting model in which there is no time-dependent dissipation. Therefore, the same values of the compacting parameter, α, were used for the

predictions of both the linear hysteretic and viscoelastic compacting models.

Tan δ is the dissipative parameter associated with the constant tan delta model. Tan delta was determined by comparing the theoretical response of the model with the soil response measured in the compression tests. Examples of theoretical stress-strain curves arising from cyclic loading of the constant tan delta model (or any linear viscoelastic model) are shown in Fig. B.12. Tan δ is the lag time between peak stress and peak strain and is related to the size of the loop formed between loading and unloading stress-strain curves. Tan δ can, therefore, be evaluated on the basis of either lag time or loop size.

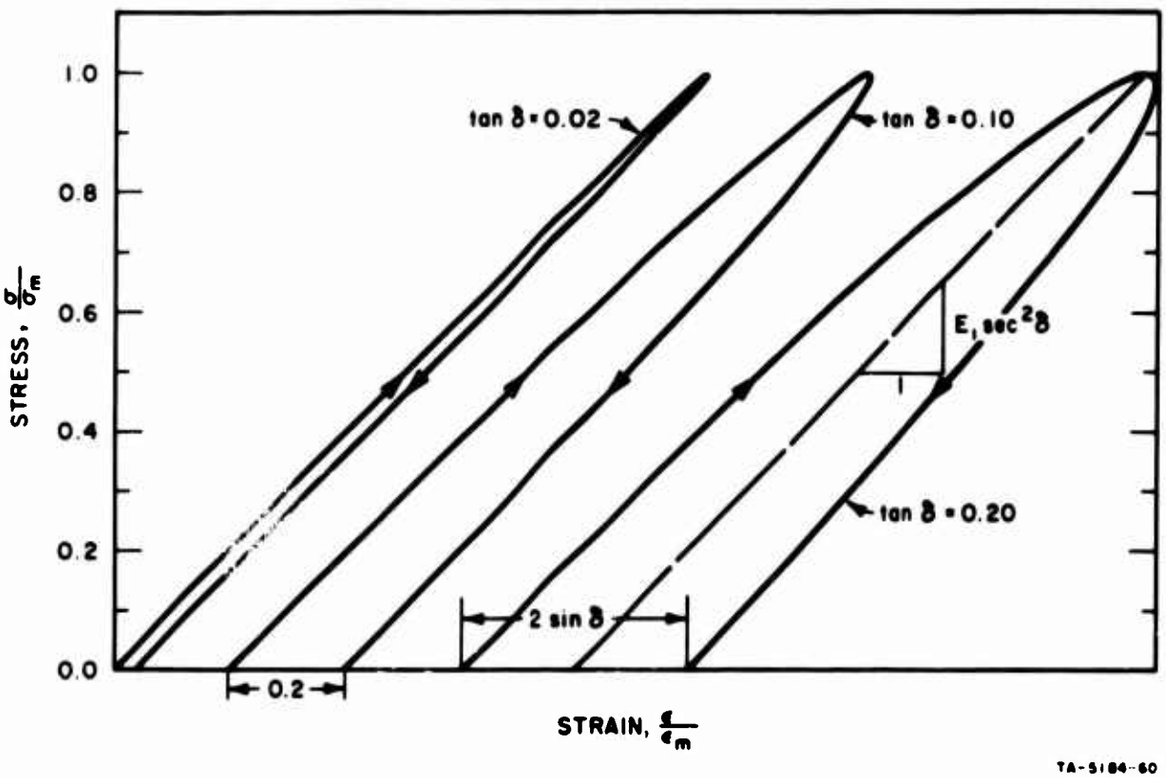

FIG. B.12 STRESS-STRAIN CURVES FROM CYCLIC LOADINGS: CONSTANT TAN DELTA MODEL

Using the lag time as an indication of tan δ gives the relation

$$\tan \delta = \omega t_l \tag{B.1}$$

for cyclic loading. If the width of the stress-strain loop at midheight is taken as the measure of tan δ, then

$$2 \sin \delta = \frac{\epsilon_{1d} - \epsilon_{2d}}{\epsilon_{1d}} \tag{B.2}$$

where ϵ_{1_d} and ϵ_{2_d} are defined in Fig. B.11. Values of tan δ derived from the two bases are listed in the sixth (ωt_ℓ) and tenth columns of Table B.2. Except for the case of soil sample 4, there is no correlation between the magnitudes of tan δ found by the two procedures. Evidently the dissipation in the soil is more complex than that in the constant tan delta model. Very precise prediction of wave propagation behavior cannot be made with this model since it is uncertain how to evaluate the basic dissipative parameter. The definition tan $\delta = \omega t_\ell$ was chosen in order to get some basis for predictions. The values of tan δ used in the wave propagation predictions are listed in Column 15 of Table B.2.

B.6 Data Reduction: Wave Velocity

Wave velocity, c, can be related to the stiffness of a material by the simple equation

$$c = \sqrt{\frac{M}{\rho}} \tag{B.3}$$

where M is an appropriate modulus, and

ρ is the density.

For soils with highly nonlinear stress-strain relations, finding an appropriate value for M is very difficult. Both the tangent modulus and the secant modulus were obtained from the test records, but the tangent modulus was used as the basis for the predictions. The basis for using the tangent modulus is the assumption that a shock wave does not occur in spite of the concave upward stress-strain curve.

The modulus data were obtained by finding the appropriate slopes of the stress-strain curves at four stress levels: 1.5, 3.0, 4.5, and 6.0 bars. The data were obtained for each peak stress level and each preload level. The resulting wave velocities that were obtained using Eq. B.3 are plotted in Figs. B.13 to B.17 as a function of depth (preload).

In general, the wave velocities appear to be fairly repeatable. They show a trend toward higher velocities for higher stress levels and preload levels. The velocities based on the tangent were used to derive the velocities used in the attenuation predictions. The prediction

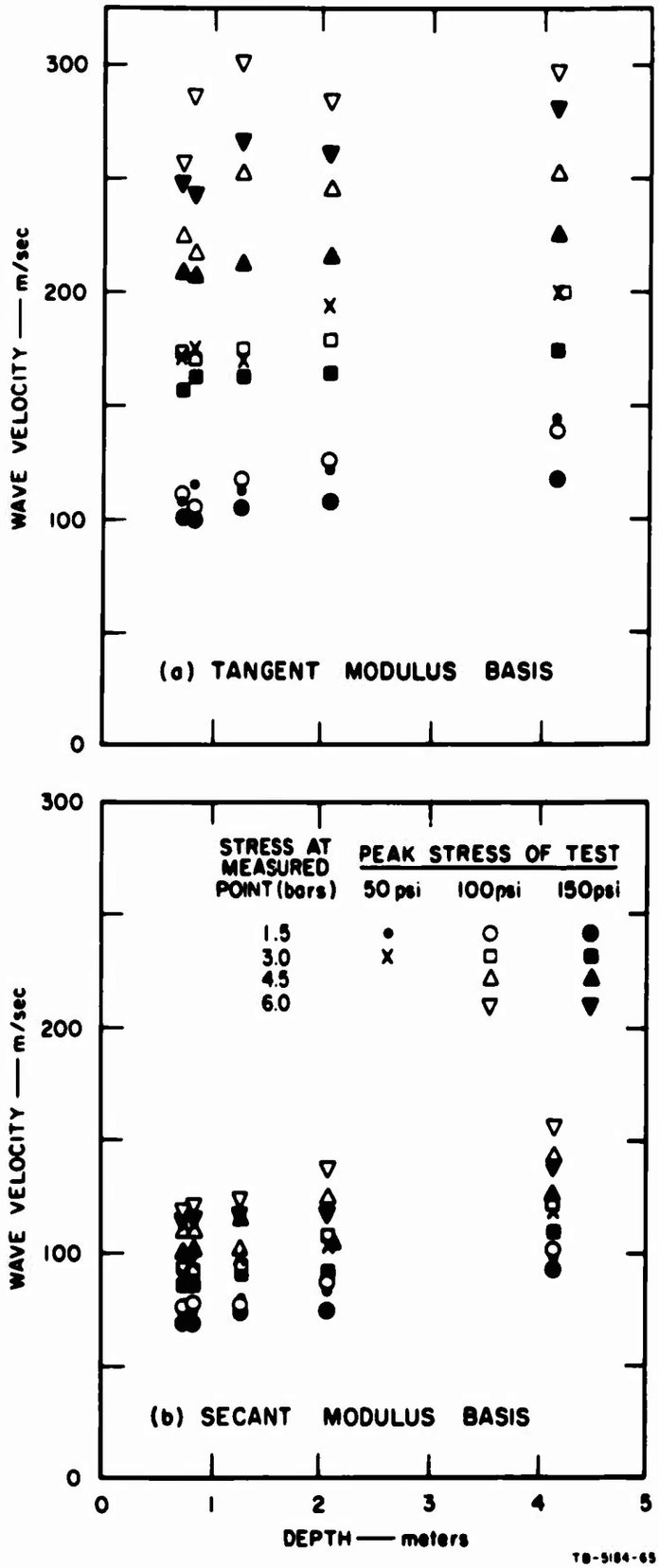

FIG. B.13 COMPUTED WAVE VELOCITIES: SAMPLE 1, KAOLINITE

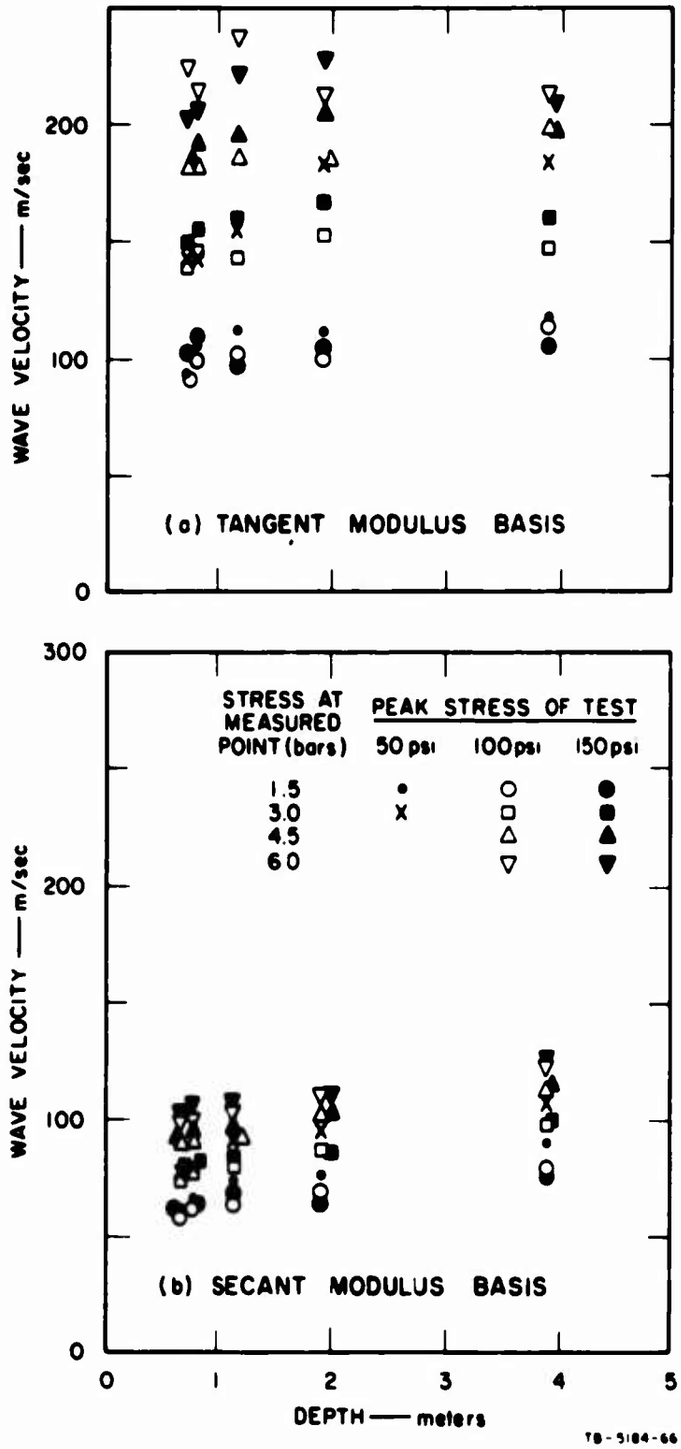

FIG. B.14 COMPUTED WAVE VELOCITIES: SAMPLE 2, KAOLINITE (Predictions for tests on column A and B)

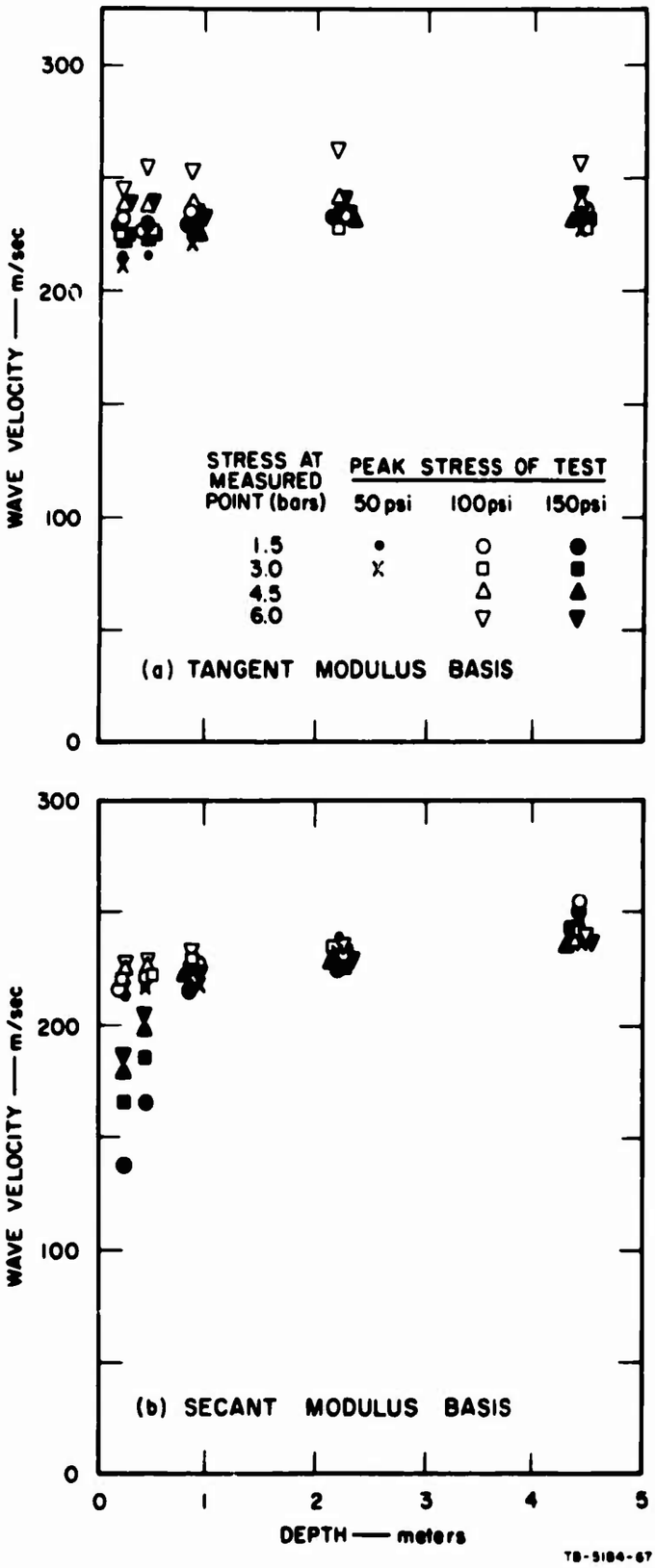

FIG. B.15 COMPUTED WAVE VELOCITIES: SAMPLE 3, KAOLINITE (Predictions for tests on column C)

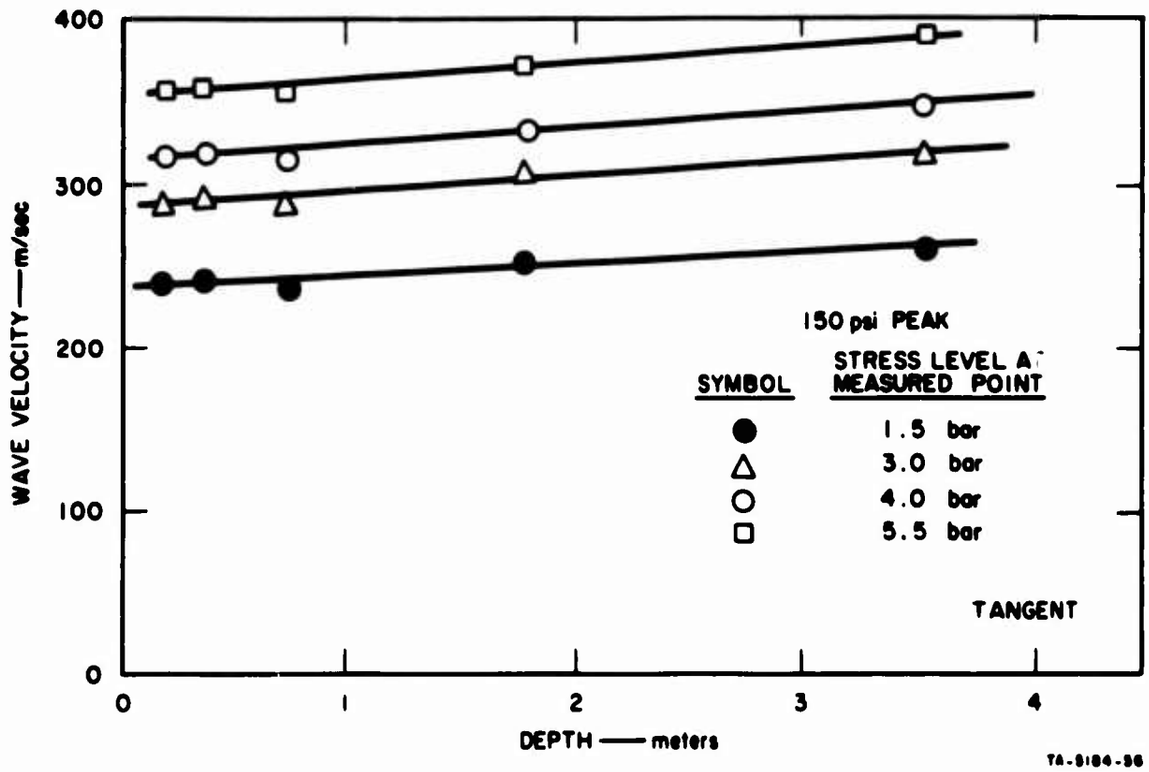

FIG. B.16 COMPUTED WAVE VELOCITIES: SAMPLE 4, VICKSBURG CLAY

(Predictions for tests on Columns D and F.)

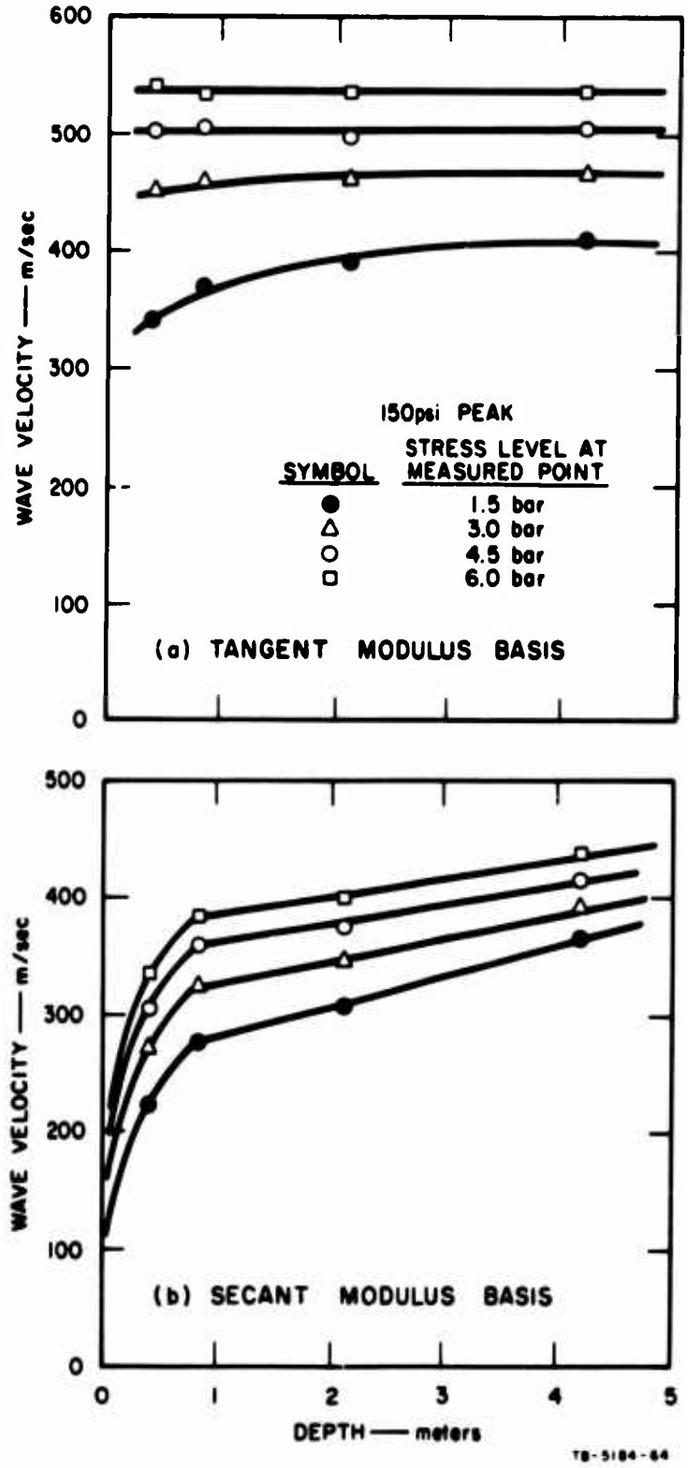

FIG. B.17 COMPUTED WAVE VELOCITIES: SAMPLE 5, MONTEREY SAND (Predictions for tests on column E)

velocity for a particular column was taken as the average of velocities determined as appropriate for conditions at the top and at the base of the column. As an example, consider the data on Vicksburg clay in Fig. B.16 In the wave propagation tests on Vicksburg clay (Column D) the peak stress at the top was 5.8 bars and that at the base was 3.0 bars. At the top (depth of zero meters) the wave velocity prediction from the figure is 360 m/sec for a dynamic stress of 5.8 bars. At the base (4.48 meters) the prediction is 320 m/sec. Then the average velocity to be used in the attenuation prediction is 340 m/sec. All the wave velocity predictions are listed in the last column of Table B.2.

NOTATION FOR APPENDIX C

b	=	α^n/T
c_0	=	wave velocity during loading
c	=	unloading wave velocity
E_0, E_1, E_2, E_3	=	moduli defined in Fig. C.2
$F(z,t,\alpha,\mu_1)$	=	correct solution to wave propagation problems
$F_1(z,t,\alpha,\mu_1)$	=	solution given by Eq. C.11
G	=	typical terms of the series of Eq. C.1
$\bar{G}$	=	one-sided Fourier transform of G
H	=	Heaviside step function
i	=	imaginary number
$J_0(i\omega)$	=	viscoelastic complex compliance for $d\sigma/dt > 0$
$J_1(i\omega)$	=	viscoelastic complex compliance for $d\sigma/dt < 0$
k_1, k_2	=	real and imaginary parts of $\sqrt{\rho J(i\omega)}$
n	=	index used in summations
p	=	applied pressure
S	=	slope of stress-strain relation
S_1	=	slope during loading (bars)
S_2	=	slope during unloading (bars)
T	=	exponential decay constant of the applied stress
t	=	time
t_a	=	arrival time of the peak stress
t_ℓ	=	lag time
t_m	=	time at which stress during loading is equal to $\sigma_0 - \frac{\sigma_1}{2}$
z	=	depth
α	=	$(c_1/c_0 - 1) / (c_1/c_0 + 1)$, dissipation parameter
β	=	c_0/c_1
δ	=	phase lag, time dependent dissipation parameter
ϵ	=	strain
ζ, ξ	=	dummy variables of Eq. C.16 and C.17
ζ	=	$E_1/(\omega\eta)$, a viscoelastic parameter used in Sect. C.5
η	=	viscosity of the dashpot

λ	=	$E_1/E_0 = E_3/E_2$
μ_1	=	η/E_0, viscoelastic time constant
ρ	=	density
Σ_1	=	summation given in Eqs. C.36 and C.37
Σ_2	=	summation given in Eqs. C.39 and C.40
σ_{LH}	=	nondimensional peak stress from linear hysteretic model
σ_{SLV}	=	nondimensional peak stress from standard linear viscoelastic model
σ_{VC}	=	nondimensional peak stress from standard linear viscoelastic compacting model
τ	=	variable defined in Eq. C.10
τ_1, τ_2	=	variables defined in Eq. C.12 and C.13
τ_p	=	t_a/T, nondimensional arrival time
ω	=	natural circular frequency

Appendix C

STRESS WAVE PROPAGATION THROUGH A VISCOELASTIC COMPACTING MEDIUM

C.1 Introduction

Dynamic compression tests show that most soils exhibit both compaction and strain-rate effects. Compaction here refers to the tendency of the material to show some permanent set after a loading and unloading cycle. Strain-rate effects refer to a group of phenomena associated with viscosity: increase in modulus with strain rate, lag of the displacement or strain behind the loading function, and smoothing of stress waves that propagate through the material. Wave propagation tests show a smoothing out of the stress wave, an indication of viscous behavior. But the attenuation of the peak stress follows roughly the prediction based on the compaction characteristics of the soil. Thus, it appeared that a more realistic prediction of wave propagation phenomena could be obtained with a model that combined viscous and compaction effects.

The mathematical model chosen here to study nondimensional stress wave propagation in soils is a combination of two models that were studied previously: the linear hysteretic (Ref. 3) and the standard linear viscoelastic models (Ref. 1). It will be referred to as the viscoelastic compacting model.

The compaction part of the mechanism is shown in Fig. C.1 as a stress-strain relation at zero rate of strain. Straight lines have been used to approximate the curved characteristics typical of most clays. On increasing the stress, the strain increases linearly along the path OA. If the stress is reversed at the point A, the strain decreases along another straight line AB. On increasing the stress again, the strain follows the path BAC. This compaction characteristic is typical of many earth materials. A stress wave propagated into such a material undergoes attenuation due to the hysteretic (compacting, frictional) nature of the medium, i.e., energy is dissipated.

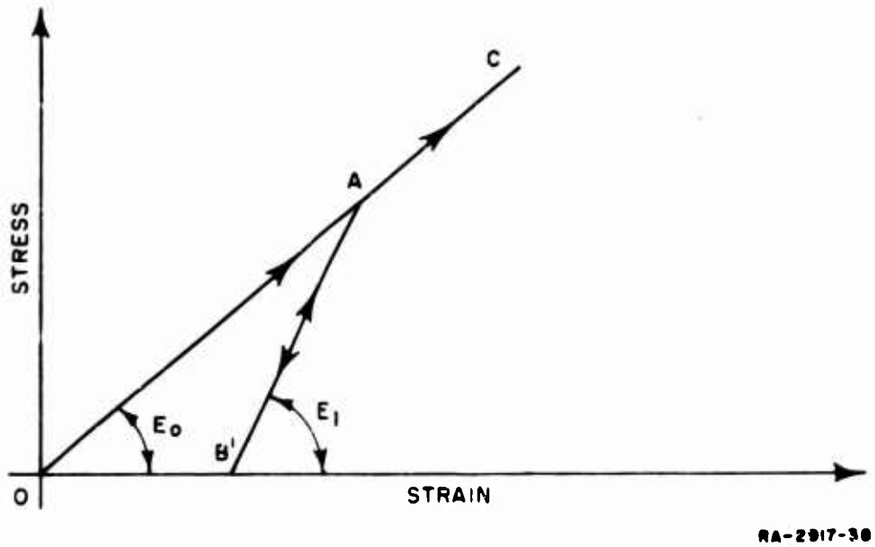

FIG. C.1 STRESS-STRAIN RELATION AT ZERO RATE OF STRAIN

In addition to this feature, we wish to introduce strain-rate effects. To do this, we assume that the material is not linearly elastic on the characteristics OA and AB but that it is linearly viscoelastic on these paths. The work of Whitman[16], Christensen and Wu[15], and Kondner and Ho[14] have indicated that the three-element standard linear viscoelastic model provides a good description of clay and sand behavior. Therefore, models of this type were chosen for both loading and unloading.

A mechanical representation of the viscoelastic compacting model is shown in Fig. C.2, labeled with the nomenclature used in the analysis. The model contains two ratchet devices which do not allow portions of the springs to expand during unloading. Thus, the spring characteristics are different during loading and unloading. During periods in which the strain rate is of constant sign, the model representation is that of a standard linear viscoelastic model. Fig. C.3 shows an example of a stress-strain relation obtained by applying to the model a pulse loading in the form of a half sine wave.

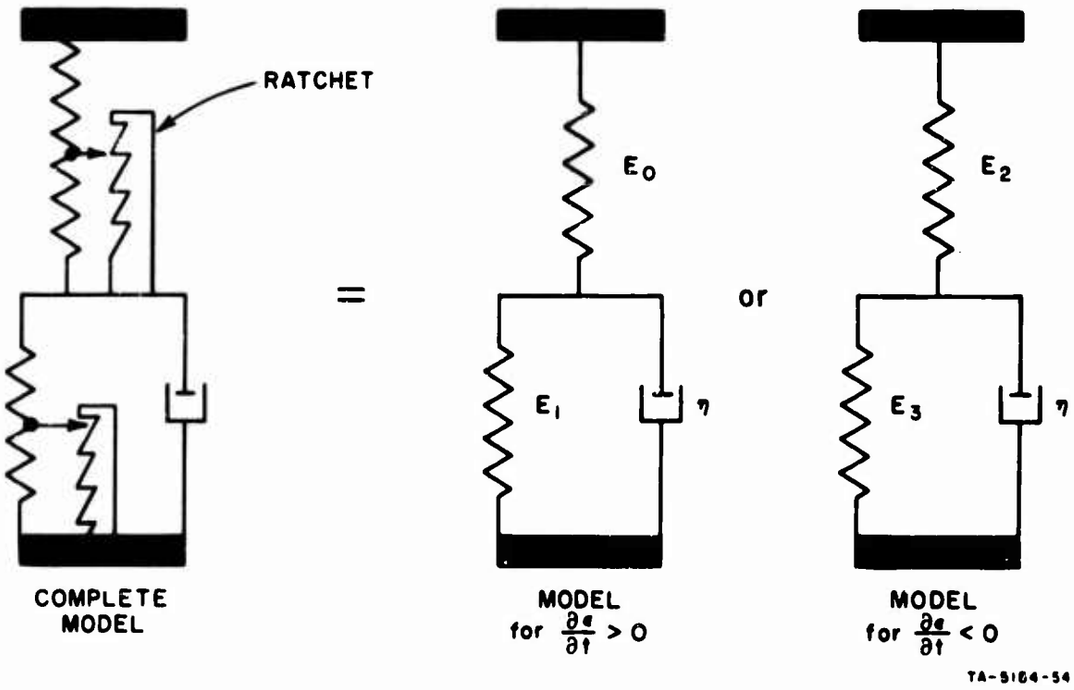

FIG. C.2 REPRESENTATION OF THE VISCOELASTIC COMPACTING MODEL

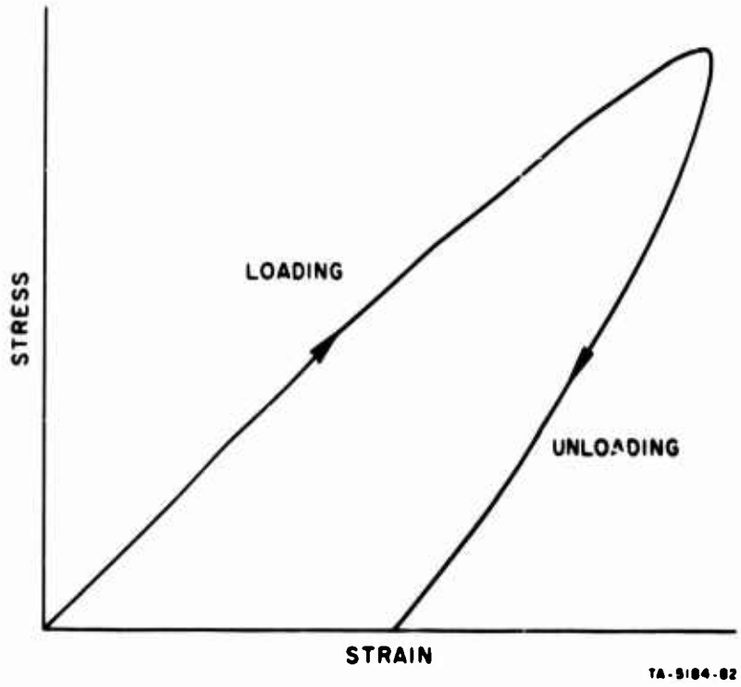

FIG. C.3 STRESS-STRAIN RELATION FOR RESPONSE OF VISCOELASTIC COMPACTING MODEL TO A HALF-SINE PRESSURE PULSE

This model was analyzed for its response during wave propagation and for its behavior during a dynamic compression test. The wave propagation results served to correlate the experimental data of Chapter 4. The compression test results provided a basis for finding the dissipative parameters of the soil (Appendix B).

C.2 Wave Propagation Analysis

An analysis was made of the response of a one-dimensional rod of a viscoelastic compacting medium subjected to a sharp pressure pulse at one end. The applied pressure pulse has a shock front and an exponential decay after the front. This wave form is similar to the pressure wave obtained from high explosives and to that produced by the drop-weight on the soil column. The wave propagation analysis was conducted to determine the stress history at several depths in the one-dimensional medium. Such stress histories are directly comparable with records of stress gages in the column of soil used on this project.

A solution for the wave propagation problem was formed, using the "correspondence principle." This was more feasible than a transform technique, which would involve the difficulty of incorporating the moving boundary between the two states of the compaction characteristic. The "correspondence principle" states that the solution to a viscoelastic problem may be obtained from the solution to the elastic case by taking the one-sided Fourier transform of the elastic solution, replacing the elastic moduli by the complex viscoelastic moduli, and inverting the transform (see Bland[22]). This principle is valid when it is applied separately on the linearly loading and unloading parts of the characteristic shown in Fig. C.1. However, it is difficult to show that the correspondence principle satisfies exactly the moving boundary condition between the states of loading and unloading. A demonstration that this principle gives a reasonable approximation to the correct solution is given in Section C.3.

The first step in the solution procedure is to find the solution for the elastic case.

The solution to the wave propagation problem in a nonviscous compacting medium is given by Salvadori, Shalak and Weidlinger (1961) in the form

$$\frac{\sigma(z,t)}{p_0} = \left[e^{-(t-z/c_1)/T} + \sum_{n=1}^{\infty} \alpha^n \left\{1 - e^{-\alpha^n (t+z/c_1)/T}\right\} - \sum_{n=1}^{\infty} \alpha^n \left\{1 - e^{-\alpha^n (t-z/c_1)/T}\right\}\right] H(t - z/c_0) \qquad (C.1)$$

where $\sigma(z,t)$ stress at depth z and time t,

$p_o e^{-t/T}$ = stress input at z = 0,

p_o = peak applied stress,

c_1 = wave velocity corresponding to the portion BA in Fig. C.1,

c_0 = wave velocity corresponding to the part OA in Fig. C.1,

α = $\frac{c_1/c_0 - 1}{c_1/c_0 + 1}$,

T = exponential decay constant of the applied stress, and

H = symbol for Heaviside step function.

Equation 1 shows the stress at any point to consist of the sum of waves propagating in both directions. The front of the stress wave propagates at the velocity c_0.

Let G be a typical term in the series of Eq. C.1, i.e.,

$$G = e^{-b(t \pm z/c_1)} H(t - z/c_0) \qquad (C.2)$$

where

$$b = \frac{\alpha^n}{T} \qquad (C.3)$$

If $\bar{G}$ denotes the one-sided Fourier transform of G, then

$$\bar{G} = \int_0^{\infty} e^{-i\omega t - bt \mp bz/c_1} H(t - z/c_0)\, dt$$

$$= \frac{e^{-[i\omega z + bz(1 \pm \beta)]/c_0}}{i\omega + b} \qquad (C.4)$$

where

$$\beta = c_0/c_1 \tag{C.5}$$

To apply the correspondence principle, it is necessary to replace c_0 by $[\rho J_0(i\omega)]^{-1/2}$ and c_1 by $[\rho J_1(i\omega)]^{-1/2}$, where ρ is the density of the material and $J_0(i\omega)$ and $J_1(i\omega)$ are the viscoelastic complex compliances of the parts OA and AB of the compacting characteristic shown in Fig. C.1. To minimize the number of parameters and to simplify the analysis, it is advantageous to make

$$\left[\frac{J_0(i\omega)}{J_1(i\omega)}\right]^{1/2} = \frac{c_1}{c_0} = \frac{1}{\beta} \tag{C.6}$$

The complex compliance of the three element viscoelastic model is given by (Bland[22]).

$$J(i\omega) = \frac{1}{E_0} + \frac{E_1}{E_1^2 + \omega^2\eta^2} - \frac{i}{\omega\eta}\left(1 - \frac{E_1^2}{E_1^2 + \omega^2\eta^2}\right) \tag{C.7}$$

where E_0 and E_1 represent spring stiffnesses as shown in Fig. B.12, and η is the viscosity of the dashpot.

If one introduces the notation

$$\lambda = E_1/E_0$$

$$\mu_1 = \eta/E_0$$

then

$$\sqrt{\rho J(i\omega)} = \sqrt{\frac{\rho}{E_0}}\sqrt{1 + \frac{\lambda}{\lambda^2 + \omega^2\mu_1^2} - \frac{i\omega\mu_1}{\lambda^2 + \omega^2\mu_1^2}}$$

$$= k_1(\omega) - ik_2(\omega) \tag{C.8}$$

where $k_1(\omega)$ and $k_2(\omega)$ are the real and imaginary parts, and $k_1(\omega)$ is essentially the reciprocal of the wave velocity.

If Eq. C.8 is substituted into Eq. 4, the transform inverted, and the real part selected, one obtains

$$G = -\frac{1}{\pi}\int_0^\infty \frac{e^{-k_2(\omega)\omega z}\, e^{-k_1(\omega) b z(1\pm\beta)}\,(b\cos\omega\tau + \omega\sin\omega\tau)\,dt}{b^2+\omega^2} \tag{C.9}$$

where

$$\tau = t - zk_1(\omega) + \frac{1}{\omega}k_2(\omega)bz(1\pm\beta) \tag{C.10}$$

The expression for the general case then follows as

$$\frac{\sigma(z,t)}{p_0} = -\frac{1}{\pi}\sum_{n=0}^{\infty}\alpha^n\int_0^\infty \frac{e^{-k_2(\omega)\omega z}\, e^{-k_1(\omega)\alpha^n z(1-\beta)/T}\left(\frac{1}{T}\alpha^n\cos\omega\tau_1 + \omega\sin\omega\tau_1\right)d\omega}{\frac{\alpha^{2n}}{T^2}+\omega^2}$$

$$+\frac{1}{\pi}\sum_{n=1}^{\infty}\alpha^n\int_0^\infty \frac{e^{-k_2(\omega)\omega z}\, e^{-k_1(\omega)\alpha^n z(1+\beta)/T}\left(\frac{1}{T}\alpha^n\cos\omega\tau_2 + \omega\sin\omega\tau_2\right)d\omega}{\frac{\alpha^{2n}}{T^2}+\omega^2} \tag{C.11}$$

where

$$\tau_1 = t - zk_1(\omega) + \frac{k_2(\omega)}{\omega}\alpha^n z(1-\beta)/T \tag{C.12}$$

$$\tau_2 = t - zk_1(\omega) + \frac{k_2(\omega)}{\omega}\alpha^n z(1+\beta)/T \tag{C.13}$$

The expression in Eq. C.11 was programmed for numerical evaluation of the integrals. Results obtained using this analysis are given in Section C.4.

C.3 Justification for Use of Correspondence Principle

Maclaurin's theorem may be used to show the nature of the approximation obtained by using the correspondence principle.

Let $F(z,t,\alpha,\mu_1)$ be the correct solution to the problem and $F_1(z,\alpha,\mu_1)$ be the solution given by Eq. C.11. The parameters α and μ_1 which measure the amount of compaction and viscosity, respectively, are to be small. When either $\alpha = 0$ or $\mu_1 = 0$, Eq. C.11 is the correct solution,* i.e.,

$$F_1(z,t,0,\mu_1) = F(z,t,0,\mu_1) \tag{C.14}$$

$$F_1(z,t,\alpha,0) = F(z,t,\alpha,0) \tag{C.15}$$

Expand both $F(z,t,\alpha,\mu)$ and $F_1(z,t,\alpha,\mu)$ as a Maclaurin series, i.e.,

$$\begin{aligned} F(z,t,\alpha,\mu_1) = {} & F(z,t,0,0) \\ & + \alpha \frac{\partial F}{\partial \alpha}(z,t,0,0) \\ & + \mu_1 \frac{\partial F}{\partial \mu_1}(z,t,0,0) \\ & + \sum_{n=2}^{\infty} \frac{1}{n!} \left(\alpha \frac{\partial}{\partial \zeta} + \mu \frac{\partial}{\partial \xi}\right)^n F(z,t,\zeta,\xi)\Big|_{\zeta=\xi=0} \end{aligned} \tag{C.16}$$

* When $\mu_1 = \alpha$, Eq. C.11 also give the correct solution for any α in this model.

$$F_1(z,t,\alpha,\mu_1) = F_1(z,t,0,0)$$

$$+ \alpha \frac{\partial F_1}{\partial \alpha}(z,t,0,0)$$

$$+ \mu_1 \frac{\partial F_1}{\partial \mu_1}(z,t,0,0)$$

$$+ \sum_{n=2}^{\infty} \frac{1}{n!}\left(\alpha \frac{\partial}{\partial \zeta} + \mu \frac{\partial}{\delta \xi}\right)^n F_1(z,t,\zeta,\xi)\Big|_{\zeta=\xi=0} \qquad \text{(C.17)}$$

From Eqs. C.14 and C.15

$$F_1(z,t,0,0) = F(z,t,0,0) \qquad \text{(C.18)}$$

$$\frac{\partial F_1}{\partial \alpha}(z,t,0,0) = \frac{\partial F}{\partial \alpha}(z,t,0,0) \qquad \text{(C.19)}$$

$$\frac{\partial F_1}{\partial \mu_1}(z,t,0,0) = \frac{\partial F}{\partial \mu_1}(z,t,0,0) \qquad \text{(C.20)}$$

Thus, F_1 is a first order approximation to F.

C.4 Results and Discussion

An example of the variation of a stress wave with distance through the medium is given in Fig. C.4. The wave maintains a shock front for the depths considered and there is no rounding off of the peak of the wave. The peak stress decreases, and the wave tends to lengthen gradually with depth.

The attenuation of peak stress with depth is shown for one case in Fig. C.5. The attenuation appears to be approximately exponential. This attenuation should be compared with that obtained using the viscous and compacting dissipative components separately. For comparison, curves from the linear hysteretic and standard linear viscoelastic models have been provided. The combination of the two dissipative parameters gives a higher attenuation rate, as expected. A comparison of a number of

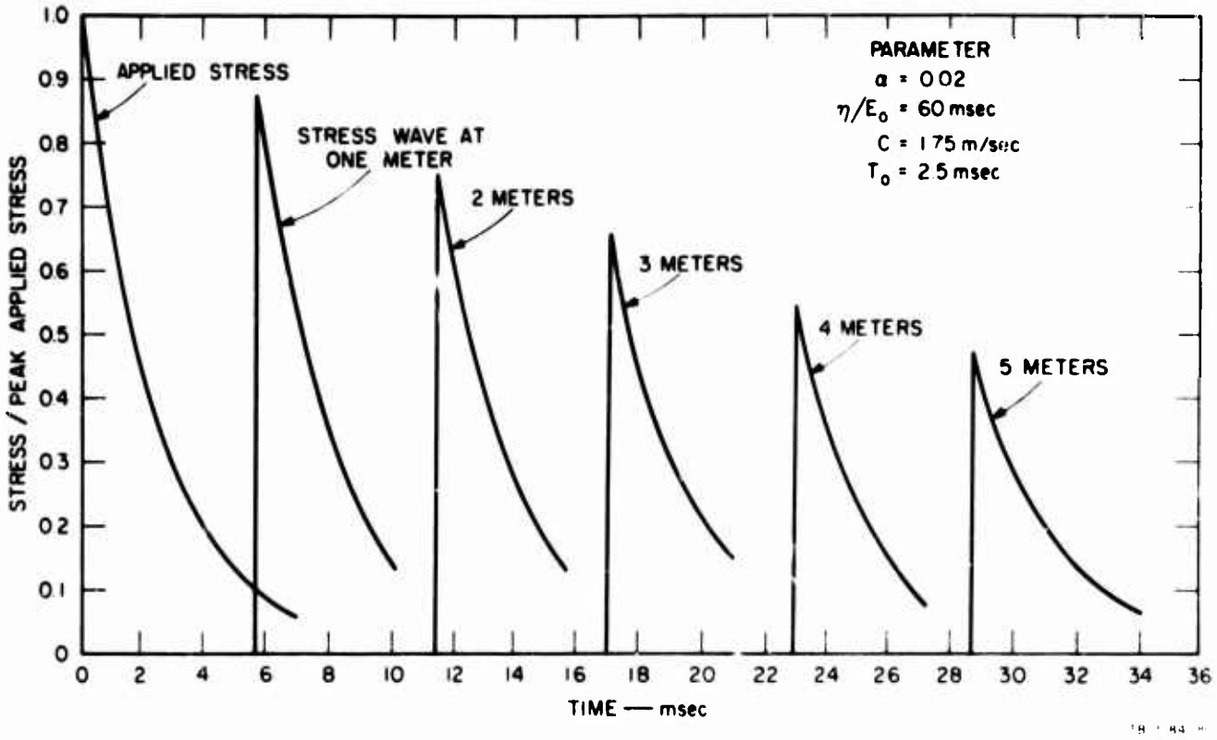

FIG. C.4 STRESS WAVES AT SEVERAL DEPTHS: VISCOELASTIC COMPACTING MODEL

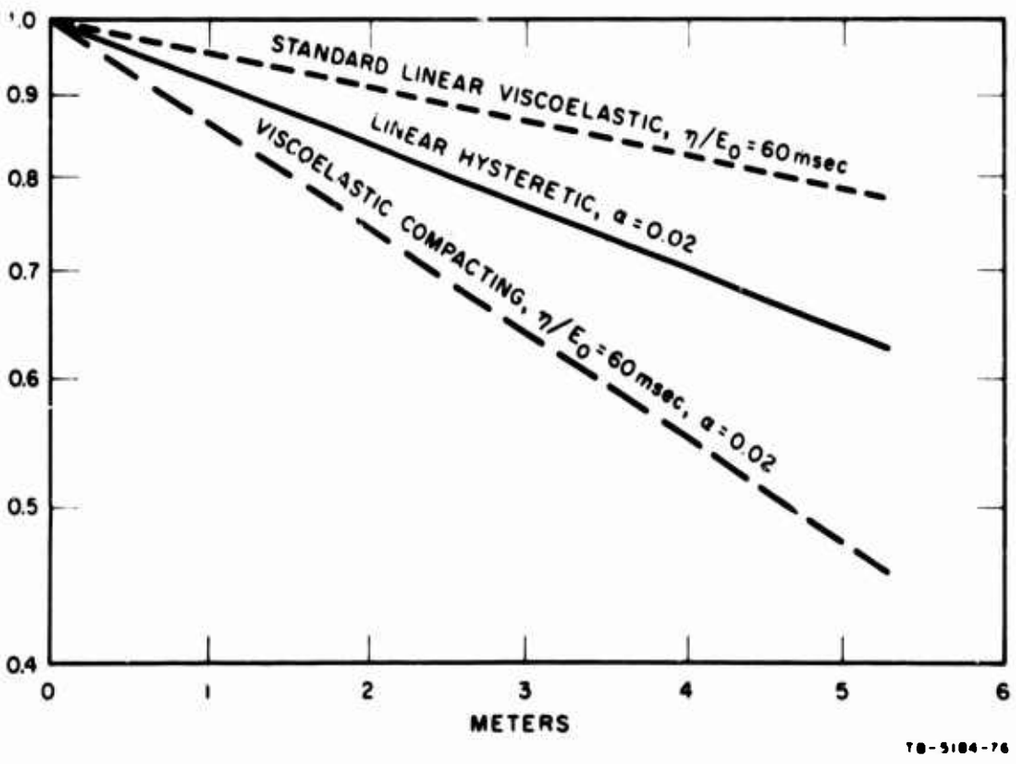

FIG. C.5 COMPARISON OF ATTENUATION BY VISCOUS, STRAIN-RATE-INDEPENDENT, AND COMBINED DISSIPATION

attenuation curves indicates that the nondimensional stress from the viscoelastic compacting model, σ_{VC}, can be predicted approximately by

$$\sigma_{VC} \approx \sigma_{LH} \times \sigma_{SLV} \tag{C.21}$$

where σ_{LH} and σ_{SLV} are the nondimensional peak stresses from the linear hysteretic and standard linear viscoelastic models. These peak stresses (see Ref 1 and 3) are given by

$$\sigma_{LH} = 1 - (1 - \alpha) \sum_{n=0}^{\infty} \alpha^n \left[1 - e^{-2\alpha^{n+1}\tau_p/(1+\alpha)}\right] \tag{C.22}$$

and

$$\sigma_{SLV} = e^{-1/2(E_0 t_a)/\eta} \tag{C.23}$$

where t_a is the arrival time of the stress wave, and

$\tau_p = t_a/T$ is the nondimensional arrival time.

Relations C.21 and C.23 are applicable in the range of depths and viscosities encountered in this study. However, to understand the behavior of the model outside this range, it is necessary to discuss some of the peculiarities of the standard linear viscoelastic model without compacting:

The first step is to introduce the loss angle, δ, for the standard linear viscoelastic model. This angle (Ref. 4) is given by

$$\tan \delta = \frac{\omega\eta/E_0}{E_1/E_0 + (E_1/E_0)^2 + (\omega\eta/E_0)^2} \tag{C.24}$$

The equation indicates how the dissipative loss is related to frequency, ω, and to viscosity, η. For infinite frequency, infinite viscosity, zero frequency, or zero viscosity, there is no viscous dissipation. Loss occurs only for some intermediate frequencies and viscosities. The maximum dissipative loss occurs at

$$\frac{\omega\eta}{E_0} = \sqrt{E_1/E_0 + (E_1/E_0)^2} \tag{C.25}$$

In wave propagation, the fact that there is no dissipation at infinite frequencies means that a shock wave front is not smoothed out but remains a shock at all depths. The magnitude of the stress associated

with the shock front decreases with depth and is given by Eq. C.23. Down to a depth, z_{cr}, this stress is the maximum stress of the wave. This critical depth (see Ref 1) is given by

$$\frac{z_{cr}}{c_0} = \frac{8}{1 + 4E_1/E_0}\left(\frac{\eta}{E_0}\right)^2 \frac{1}{p_0}\frac{dp}{dt}\bigg|_{t=0} \qquad (C.26)$$

where $\frac{dp}{dt}_{t=o}$ is the initial rate of decay of applied pressure,

p_o is the peak applied pressure.

For larger depths, the peak stress occurs at some time after the shock front. At a considerably greater depth, the wave again appears to have a sharp front and the peak stress travels at $c_0/\sqrt{E_1/E_0}$.

Similar effects can be expected to occur with the viscoelastic compacting model. For a very large and very small viscosity, all the dissipation can be attributed to α. The stress wave front maintains a shock front to all depths, but beyond some depth, the peak stress may occur sometime after the shock front. The particle velocity attenuates at the same rate as the stress for both the linear hysteretic model and for the standard linear viscoelastic model down to the depth given by C.26. Hence, it can be expected that the particle velocity and stress attenuate at the same rate in the viscoelastic compacting model down to a depth at which the peak does not occur at the shock front.

C.5 Response in a Dynamic Compression Test

An analysis was made of the response of the viscoelastic compacting model to a pressure pulse in the form of a sinusoid. This analysis was conducted to provide a means for interpreting the experimental stress-strain data obtained from compression tests on soil samples (App. B).

The whole model element is assumed to receive the loading simultaneously so that there is no wave propagation. The loading function used is

$$\sigma = \frac{\sigma_0}{2}\left[1 - \cos\omega t + \left(1 - \frac{\sigma_1}{\sigma_0}\right)(1 + \cos\omega t)H(t - \pi/\omega)\right] \qquad (C.27)$$

where σ_0 is the peak applied stress,

σ_1 is the decrease in stress after the peak,

ω is the natural circular frequency,

t is time, and

H is the Heaviside step function.

The loading (shown in Fig. C.6) approximates very well the actual loadings obtained with the MIT tester.

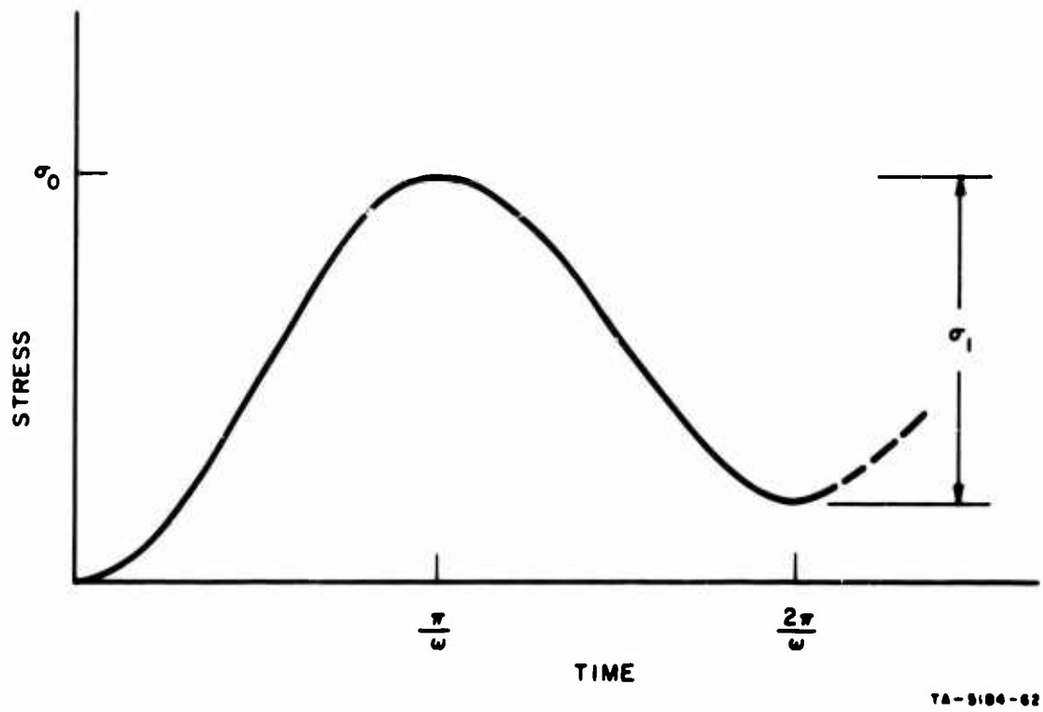

FIG. C.6 FORM OF THE ANALYTICAL LOADING

The strain response to a step function of stress on the model is

$$\epsilon = \frac{\sigma}{E_0} + \frac{\sigma}{E_1}\left(1 - e^{-\frac{E_1 t}{\eta}}\right) \qquad (C.28)$$

where σ is the stress magnitude of the step,

E_0 and E_1 are moduli defined in Fig. C.2, and

η is the viscosity associated with the dashpot in Fig. C.2.

Using the superposition integral, the strain caused by the loading in Eq. C.27 is

$$\epsilon = \sigma_0\left(\frac{1}{E_0} + \frac{1}{E_1}\right) - \frac{\sigma_0\left(1 + e^{-\frac{E_1\pi}{\omega\eta}}\right)e^{-\frac{E_1}{\omega\eta}(\omega t - \pi)}}{2E_1\left[1 + \left(\frac{E_1}{\omega\eta}\right)^2\right]}$$

$$- \frac{\sigma_1}{2}\left(\frac{1}{E_0} + \frac{1}{E_1}\right)(1 + \cos\omega t)$$

$$+ \frac{\sigma_1\left[-\frac{E_1}{\omega\eta}\sin\omega t + \cos\omega t + e^{-\frac{E_1}{\omega\eta}(\omega t - \pi)}\right]}{2E_1\left[1 + \left(\frac{E_1}{\omega\eta}\right)^2\right]} \qquad \text{(C.29)}$$

This equation is valid between the time of maximum stress and the time of maximum strain. At maximum strain, locking occurs, and the unloading parameters must be used to find the strain response. The time of maximum strain is given by

$$\frac{\partial\epsilon}{\partial t} = 0 \qquad \text{(C.30)}$$

where the strain is given by the expression in C.29. The condition is

$$\left[\frac{\sigma_0}{\sigma_1} e^{-\zeta\pi} + \frac{\sigma_0}{\sigma_1} - 1\right]e^{-\zeta\omega t_l} + \cos\omega t_l - \left(\zeta + \frac{\lambda}{\zeta} + \lambda\zeta\right)\sin\omega t_l = 0 \qquad \text{(C.31)}$$

where $\zeta = \frac{E_1}{\omega\eta}$

$t_\ell = t = \pi/\omega$, the lag time between peak stress and peak strain

$\lambda = E_1/E_0$

The lag time can be determined from the difference between peak times on the stress-time and the strain-time curves obtained from the compression tests. Then Eq. C.31 provides one condition on λ and ζ. A second condition was generated by taking the maximum value of λ for which a solution could be obtained for ζ from Eq. C.21. For smaller values of λ, two solutions of ζ are obtained; for larger values there are no solutions.

Hence, by the choice of this second condition, a unique value of ζ is required. The values of λ obtained by this procedure are in the range found by Whitman.[16]

A complete graphical solution of Eq. C.31 and the second condition are given in Fig. C.7. A minor variable in the solution is the ratio of σ_0/σ_1. Given ωt_ℓ and σ_0/σ_1, $\zeta = E_1/\omega\eta$ and $\lambda\omega t_\ell \sigma_1/\sigma_0$ can be found from the figure.

The next step is to find the compacting dissipative parameter, α. The parameter, α, is given by the ratio of the slopes at zero strain rate and, hence, by the ratio of the moduli, E_0 and E_2.

$$\alpha = \frac{1 - \sqrt{E_0/E_2}}{1 + \sqrt{E_0/E_2}} \tag{C.32}$$

The slopes of the stress-strain curves would be proportional to the moduli E_0 and E_2 if there were no viscous efforts. The rate-dependent character will modify the proportionality to some extent. The slopes will be evaluated at mid-height of the unloading stress-time loop because the viscous effects will be minor at that stress level (see Fig. B.11). To evaluate these slopes it is necessary to continue the loading analysis to determine the strain at all times during the initial loading and unloading. In the analysis it was assumed that $E_1/E_3 = E_0/E_2$ to reduce the number of parameters. For the initial loading, the strain is simply

$$\epsilon = \frac{\sigma_0}{2}\left(\frac{1}{E_0} + \frac{1}{E_1}\right)(1 - \cos\omega t) - \frac{\sigma_0\left(\frac{E_1}{\omega\eta}\sin\omega t - \cos\omega t + e^{-\frac{E_1 t}{\eta}}\right)}{2E_1\left[1 + \left(\frac{E_1}{\omega\eta}\right)^2\right]} \quad \text{for} \quad t < \frac{\pi}{\omega} \tag{C.33}$$

The slope of the stress-strain curve is

$$S_1 = \frac{\partial\sigma}{\partial t}\Big/\frac{\partial\epsilon}{\partial t} \tag{C.34}$$

where σ is given by Eq. C.27.

The slope was evaluated at a loading stress level equal to the mid-height stress of the unloading stress-strain loop; hence,

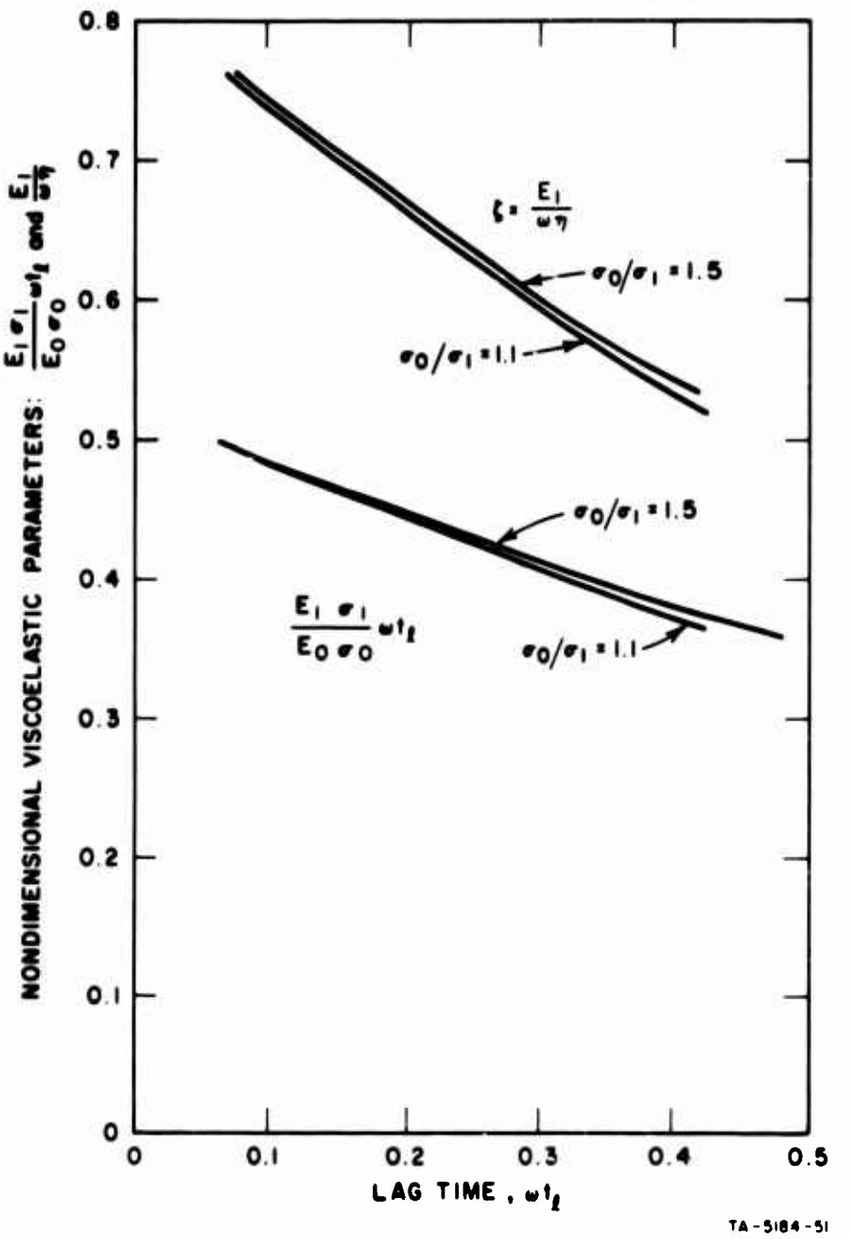

FIG. C.7 GRAPHICAL SOLUTION FOR VISCOELASTIC PARAMETERS FOR THE VISCOELASTIC COMPACTING MODEL

at

$$\left.\begin{aligned} \frac{\sigma_0}{2}(1 - \cos \omega t_m) &= \sigma_0 - \frac{\sigma_1}{2} \\ \text{or} \qquad \cos \omega t_m &= -1 + \frac{\sigma_1}{\sigma_0} \end{aligned}\right\} \tag{C.35}$$

The slope of the loading curve at the time given by Eq. C.35 is

$$S_1 = \frac{E_0\left[1 + \left(\frac{E_1}{\omega\eta}\right)^2\right]}{1 + \left(\frac{E_1}{\omega\eta}\right)^2 + \frac{E_1 E_0}{\omega^2\eta^2} - \frac{E_0/\omega\eta}{\sqrt{2\sigma_0/\sigma_1 - 1}}\left(1 - \frac{\sigma_0}{\sigma_1} - \frac{\sigma_0}{\sigma_1} e^{-\frac{E_1}{\eta} t_m}\right)} \tag{C.36}$$

where t_m is to be evaluated from Eq. C.35.

For convenience, the sum in the denominator will be designated by Σ_1 so that

$$S_1 = \frac{E_0\left[1 + \left(\frac{E_1}{\omega\eta}\right)^2\right]}{\Sigma_1} \tag{C.37}$$

The strain during unloading is

$$\begin{aligned} \epsilon = {} & \sigma_0\left(\frac{1}{E_2} + \frac{1}{E_3}\right) - \frac{\sigma_1}{2}\left(\frac{1}{E_2} + \frac{1}{E_3}\right)(1 + \cos \omega t) \\ & - \frac{\sigma_0\left(1 + e^{-\frac{E_1 \pi}{\omega\eta}}\right) e^{-\frac{E_1}{\omega\eta}(\omega t_l)} e^{-\frac{E_3}{\omega\eta}(\omega t - \pi - \omega t_l)}}{2E_3\left[1 + \left(\frac{E_1}{\omega\eta}\right)^2\right]} \\ & + \frac{\sigma_1\left(\frac{E_1}{\omega\eta}\sin \omega t_l - \cos \omega t_l + e^{-\frac{E_1}{\eta} t_l}\right) e^{-\frac{E_3}{\omega\eta}(\omega t - \pi - \omega t_l)}}{2E_3\left[1 + \left(\frac{E_1}{\omega\eta}\right)^2\right]} \end{aligned}$$

$$- \frac{\sigma_1\left(\frac{E_3}{\omega\eta}\sin\omega t_l - \cos\omega t_l\right) e^{-\frac{E_3}{\omega\eta}(\omega t - \pi - \omega t_l)}}{2E_3\left[1 + \left(\frac{E_3}{\omega\eta}\right)^2\right]}$$

$$- \frac{\sigma_1\left(\frac{E_3}{\omega\eta}\sin\omega t - \cos\omega t\right)}{2E_3\left[1 + \left(\frac{E_3}{\omega\eta}\right)^2\right]} \qquad \text{(C.38)}$$

The slope S_2 is evaluated at the middle of the unloading cycle; hence, at $\omega t = 3\pi/2$. The slope is

$$\frac{1}{S_2} = \frac{1}{E_2\left[1 + \left(\frac{E_1}{\omega\eta}\right)^2\right]}\left\{\left(1 + \frac{E_0}{E_1}\right)\left[1 + \left(\frac{E_1}{\omega\eta}\right)^2\right] - \frac{1 + \left(\frac{E_1}{\omega\eta}\right)^2}{1 + \left(\frac{E_3}{\omega\eta}\right)^2} \cdot \frac{E_0}{E_1}\right.$$

$$- \frac{E_0}{E_1}\frac{E_3}{\omega\eta}\frac{\left[1 + \left(\frac{E_1}{\omega\eta}\right)^2\right]}{\left[1 + \left(\frac{E_3}{\omega\eta}\right)^2\right]}\left(\frac{E_3}{\omega\eta}\sin\omega t_l - \cos\omega t_l\right) e^{-\frac{E_3}{\omega\eta}\left(\frac{\pi}{2} - \omega t_l\right)}$$

$$\left. - \frac{E_3}{\omega\eta} \cdot \frac{E_0}{E_1}\left[-\frac{E_1}{\omega\eta}\sin\omega t_l + \cos\omega t_l + \left(\frac{\sigma_0}{\sigma_1} e^{-\frac{E_1\pi}{\omega\eta}} + \frac{\sigma_0}{\sigma_1} - 1\right) e^{-\frac{E_1 t_l}{\omega}}\right] e^{-\frac{E_3}{\omega\eta}\left(\frac{\pi}{2} - \omega t_l\right)}\right\}$$

When the sum in braces is replaced by Σ_2, Eq. C.39 becomes (C.39)

$$S_2 = \frac{E_2\left[1 + \left(\frac{E_1}{\omega\eta}\right)^2\right]}{\Sigma_2} \qquad \text{(C.40)}$$

The ratio of the two slopes is

$$\frac{S_1}{S_2} = \frac{E_0}{E_2} \cdot \frac{\Sigma_2}{\Sigma_1} \quad \text{or} \quad \frac{E_0}{E_2} = \frac{S_1}{S_2} \cdot \frac{\Sigma_1}{\Sigma_2} \qquad \text{(C.41)}$$

Because Σ_2 contains the ratio E_0/E_2, Eq. C.41 cannot be solved explicitly. However, E_0/E_2 is approximately equal to S_1/S_2. With this as a first approximation, the correct value of E_0/E_2 can be readily obtained by iteration. Finally, α can be determined from Eq. C.32.

This analysis provided the basis for determining both the visco-elastic and compacting parameters from the soils data.

BLANK PAGE

NOTATION FOR APPENDIX D

A	=	coefficient of stress-strain relation (bars)
B	=	coefficient of convex portion of stress-strain curve
b	=	coefficient for exponential decay of hump
c	=	Lagrangian wave speed (gm/cm^2 sec)
E_0	=	permanent set
$F(m)$	=	strain on shock front
F_1	=	coefficient of variable term in approximation to F
$f(\epsilon, m)$	=	stress-strain relation
G, H	=	functions found in the solution of the initiation problem
G_1	=	coefficient of the approximation to G
g	=	acceleration of gravity, (cm/sec^2)
H, J	=	arbitrary constants
η	=	function defined following Eq. 44
h_1, h_2	=	proportionality factors
k	=	$(R - 1)/(R + 1)$
$M(\ln z)$	=	$G(z)$
m	=	mass per unit cross-section area (gm/cm^2)
N	=	$1/n$
N_2	=	$1/n_2$
n	=	exponent giving curvature of stress-strain relation
n_1	=	curvature parameter for hump on stress-strain curve
n_2	=	curvature of unloading stress-strain relation
P	=	preload on top of column (bars)
p	=	$(\gamma/S_0 - 1)^N - (\gamma/S_0 + 1)^N$
Q	=	peak applied dynamic stress (bars)
q	=	$(\gamma/S_0 - 1)^N + (\gamma/S_0 + 1)^N$
R	=	γ/S_0
R, L	=	subscripts for approximations made on the basis of points to the right and to the left
r, s	=	characteristic coordinates

$\mathcal{J}$ = position of shock front in r-s coordinates

S = dm/dt

S_0 = $\left[\rho^{(o)}Q/E_0\right]^{1/2}$

T = time on the shock front

T_0 = decay constant for loading (sec)

t = time (sec)

U = shock velocity

U_i = initial modulus

u, b = subscripts for approximations made on the basis of points above (upper) and below

$V(m)$ = particle velocity on the shock front

v = particle velocity

v_0, v_1 = particle velocity on front and back of shock

w = arbitrary function

x = depth in the column (cm)

y = $\ln \eta$

z = an arbitrary variable used in defining M

γ = $\left[\rho^{(o)}Qn_2/(E_0 - E_0)\right]^{1/2}$

δ = $(g/A)^N$

ϵ = strain

$\epsilon^{(s)}$ = static strain

ζ = $-m\ (R - 1)$

η = $-m\ (R + 1)$

μ = $\gamma V_0/2Q$

ξ = position of the shock front in time and depth

ρ = density (gm/cm^3)

$\rho^{(o)}$ = initial density

ρ_0, ρ_1 = density on front and back of shock

σ = stress (bars)

$\sigma^{(s)}$ = static stress (bars)

σ_0, σ_1 = stress on front and back of shock

Appendix D

NONLINEAR HYSTERETIC MEDIUM

D.1 Introduction

The analytical work described here was directed toward two aspects of wave propagation:

1. Effect of geostatic stress on attenuation of stress.
2. Wave front formation.

Geostatic stress (initial stress or preload due to overburden) alters the wave velocity and makes the soil stiffer than it would be if it were initially stress free. Usually the geostatic stress causes the wave velocity to increase with depth. Wave propagation through a medium with properties which vary with distance may have characteristics considerably different from that through a homogeneous medium. Concern about these characteristics prompted a wave propagation analysis of a model with nonlinear loading and unloading relations similar to those of soils. The effect of geostatic stress was considered in the analysis.

Wave front formation presents an anomalous situation in one-dimensional wave propagation. As waves propagate through soil, the rise time (time from zero stress to the peak) tends to increase. However, in one-dimensional compression tests, soils exhibit stress-strain relations that are predominantly concave to the stress axis. Such a relation indicates that rise times should decrease as the wave moves through the soil. To explain the lengthening of the rise time then some other factor must be introduced such as effect of loading rate, or of preload. When soil with a preload is dynamically loaded, the stress-strain relations show a small initial portion that is convex to the stress axis. One of the goals of the study was to determine the influence of this convex portion on the rise time of the propagating stress wave.

With these two goals in mind—investigation of the effect of geostatic stress and of wave front formation—a study was undertaken of a theoretical model with nonlinear loading and unloading stress-strain

relations but with no time-dependence. The loading relation could be either wholly concave to the stress axis or initially convex and then concave at higher stresses. The unloading relation was entirely concave to the stress axis. With the wholly concave loading relation, the effect of geostatic stress was considered. Solutions for the wave propagation problem in this medium were obtained for a loading with a shock front and an exponential decay of pressure. This solution provided a determination of the effects of geostatic stress and curvature of the loading relation on the attenuation of stress in a propagating wave.

The loading relation which is initially convex and then concave was required to study the matter of wave front formation. The computer program for the solution of the wave propagation problem with this loading relation was only partially completed at the close of the project. Therefore, no results are available on the subject of wave front development.

D.2 Governing Equations

D.2.1 General Equations

We considered a column of material with cross-sectional area acted upon by gravity and an applied load. Thus, one space dimension and the time are needed as independent variables. Because the stress-strain relation for each particle depends on the history of the particle, it is useful to introduce a Lagrangian space coordinate that is a constant for each particle.

Let x(cm) be the distance below a fixed reference level and t(sec) be the time. For the Lagrangian coordinate, let m(gm/cm^2) be the mass per unit cross-sectional area between the top of the column and point x in the column. Thus, the Lagrangian coordinate represents a product of density and depth in the column.

The loading, or applied stress, is assumed to be

$$\sigma = \begin{cases} P, & t < 0 \\ P + Qe^{-t/T_0} & t \geq 0 \end{cases} \qquad \text{(D.1)}$$

where Q and T_0 are positive constants and P is non-negative. With the loading, a shock front will develop at the surface at $t = 0$.

If σ (dynes/cm^2) is the stress taken positive for compression, then the equation of motion is

$$x_{tt} = g - \sigma_m \tag{D.2}$$

where subscript denote differentiation and g (cm/sec^2) is the acceleration of gravity.

The continuity relation can be determined using the definition of density, ρ, and the Lagrangian coordinate,

$$\rho x_m = 1 \tag{D.3}$$

and the definition of strain

$$\epsilon = 1 - \frac{\rho^{(0)}}{\rho} = 1 - \rho^{(0)} x_m \tag{D.4}$$

where $\rho^{(0)}$ is the density in the stress free state. Then

$$\epsilon_t = -\rho^{(0)} x_{mt} = -\rho^{(0)} v_m \tag{D.5}$$

D.2.2 <u>Constitutive Relations</u>

The static relation between stress, σ, and strain, ϵ, is taken to be

$$\sigma = A\epsilon^n \tag{D.6}$$

With A (dyne/cm^2) and n (dimensionless) positive constants. At time zero, the column is at rest under gravity and an applied load of P (dynes/cm^2). Hence,

$$\sigma^{(s)} = P + mg \tag{D.7}$$

and

$$\epsilon^{(s)} = \left(\frac{P + mg}{A}\right)^{\frac{1}{n}} \tag{D.8}$$

where the superscript (s) indicates static conditions.

For dynamic loading, the constitutive equation is assumed to be

$$\sigma = A\epsilon^n + B[\epsilon^{(s)}]^{n_1} [\epsilon/\epsilon^{(s)} - 1] e^{-b[\epsilon/\epsilon^{(s)} - 1]} \tag{D.9}$$

where B and b are positive constants. The equation applies only where $\epsilon_t > 0$. The form of this equation has been chosen to simulate

the combined yielding-stiffening stress-strain curve that has been observed for sand. The first term gives the basic stiffening behavior. The second term provides an initial "bump", the importance of which is controlled by the initial static strain and hence by the static stress (see Fig. D.1).

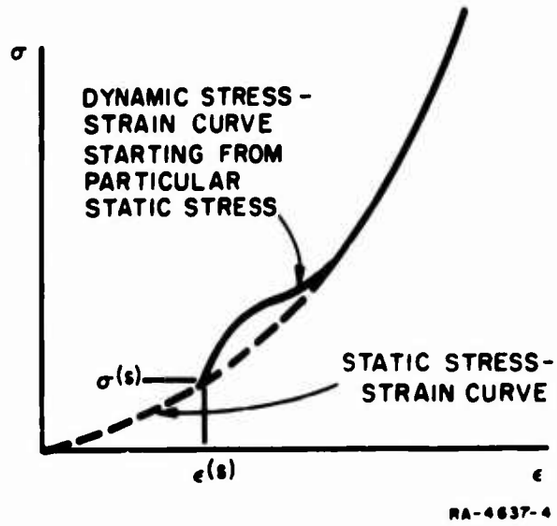

FIG. D.1 S-SHAPED STRESS-STRAIN CURVE FOR SOIL

The tangent modulus right at the start of the "bump" is given by

$$u_t = \left.\frac{d\sigma}{d\epsilon}\right|_{\epsilon=\epsilon(s)} = nA[\epsilon(s)]^{n-1} + B[\epsilon(s)]^{n_1-1}$$

$$= nA\left[\frac{\sigma(s)}{A}\right]^{\frac{n-1}{n}} + B\left[\frac{\sigma(s)}{A}\right]^{\frac{n_1-1}{n}} \qquad \text{(D. 10)}$$

This tangent modulus should be related to the velocity with which seismic level waves propagates through soil. From the available data (Hardin and Richart[23]), it appears that this initial tangent modulus should vary as $\sigma(s)^{1/2}$; that is, n_1 and n should equal 2. In the calculations it was assumed that $n_1 = n$.

Equation D.9 will give combined yielding and stiffening only if the tangent modulus goes through a minimum. The condition for the existence of such a minimum is $A/bB < 1$. Otherwise the curve will always be concave to its stress axis.

For unloading, that is, for $\epsilon_t \leq 0$ the constitutive relation is

$$\sigma = C(\epsilon - E)^{n_2} \tag{D.11}$$

where C (dynes/cm^2) and n_2 are positive constants and E corresponds to the residual strain when unloading is completed. At each point, E is determined by equating D.9 and D.11 at the peak stress. The unloading relation was formulated as a reasonable representation of observed stress-strain relations in sand.

The constitutive relations, Eqs. D.9 and D.11, show that the stress is a function of geostatic stress and the residual strain, which is a function of the previous peak stress at the point. Hence, the constitutive relations will vary with depth. To emphasize this functional dependence, we write $\sigma = f(\epsilon, m)$ where it is understood that either D.9 or D.11 is used depending on the sign of ϵ_t.

The constitutive relations are formulated only for one loading and for one unloading. Due to the nature of the wave propagation problem, it was not necessary to formulate a relation for a second loading cycle.

D.2.3 Characteristic Relations

To develop the characteristic coordinates and equations, the equations of motion and continuity are presented in the following form:

$$v_t = g - (f_\epsilon \epsilon_m + f_m) \tag{D.12}$$

$$\epsilon_t = -\rho^{(0)} v_m \tag{D.5}$$

Following Courant and Friedrichs[24] we form a linear combination of the two equations, say H times the first plus J times the second

$$Hv_t + \rho^{(0)} J v_m + J\epsilon_t + f_\epsilon H \epsilon_m = H(g - f_m) \tag{D.13}$$

This equation is in characteristic form if both v and ϵ are being differentiated in the same direction, that is, if

$$\frac{H}{\rho^{(0)} J} = \frac{J}{f_\epsilon H} \tag{D.14}$$

Put $c^2 = \rho^{(o)} f_\epsilon$ so that the requirement of Eq. D.14 is

$$J = \pm[c/\rho^{(0)}]H \tag{D.15}$$

Substitution into Eq. D.13 gives

$$v_t \pm cv_m \pm [c/\rho^{(0)}](\epsilon_t \pm c\epsilon_m) = g - f_m \tag{D.16}$$

Thus, c (gm/cm^2 - sec) is the speed of waves in the Lagrangian coordinate system. Note that the units of c are <u>not</u> length per unit time.

The characteristic coordinates r and s are introduced by requiring, for any function w, that $w_t - cw_m$ be proportional to w_r and $w_t + cw_m$ be proportional to w_s. Thus,

$$w_t - cw_m = h_1 w_r \quad \text{and} \quad w_t + cw_m = h_2 w_s \tag{D.17}$$

where h_1 and h_2 are proportionality factors. By letting w = t and then m, it follows that

$$t_r = \frac{1}{h_1}, \quad m_r = -\frac{c}{h_1}, \quad t_s = \frac{1}{h_2}, \quad m_s = \frac{c}{h_2} \tag{D.18}$$

Eliminating h_1 and h_2 from D.17 and D.18, results in the following characteristic relations:

Along characteristics where r is constant,

$$m_s = ct_s \tag{D.19}$$

$$v_s + [c/\rho^{(0)}]\epsilon_s = (g - f_m)t_s \tag{D.20}$$

Along characteristics where s is constant,

$$m_r = -ct_r \tag{D.21}$$

$$v_r - [c/\rho^{(0)}]\epsilon_r = (g - f_m)t_r \tag{D.22}$$

The r = constant waves are outgoing waves along which m increases with t. The s = constant waves are incoming since m decreases as t increases. Not that the coefficients c, $c/\rho^{(o)}$, and $g - f_m$ in D.19 to D.22 are functions of ϵ and m.

For use in the numerical calculations, D.19 - D.22 must be approximated by finite difference equations. In the r-s plane, we will set r and s as the vertical and horizontal coordinates, respectively.

Thus, in D.19 and D.20 we consider a left point, L , and a right point, R , in approximating the s-derivatives of the variables ϵ, m, v, and t. The difference equations we shall use are

$$m_R - m_L = c(t_R - t_L) \tag{D.19a}$$

$$v_R - v_L + [c/\rho^{(0)}](\epsilon_R - \epsilon_L) = (g - f_m)(t_R - t_L) \quad . \tag{D.20a}$$

Eqs. D.19a and D.20a best approximate D.19 and D.20 when the coefficients are evaluated for the averages of the values of ϵ and m at L and R. Similarly, for an upper point, u , and a lower point, b , we have

$$m_u - m_b = -c(t_u - t_b) \tag{D.21a}$$

$$v_u - v_b - [c/\rho^{(0)}](\epsilon_u - \epsilon_b) = (g - f_m)(t_u - t_b) \quad . \tag{D.22a}$$

D.2 4 Shock Equations

Now consider a shock front moving relative to the material enveloping at a time, t , the particle with Lagrangian coordinate*, m=m(t). Then if x(m,t) is the position of the particle with the coordinates m and t, the position of the shock front is given by

$$\xi = x[m(t), t]$$

and, thus, the shock velocity is

$$U = x_m \frac{dm}{dt} + x_t = \rho^{-1} \frac{dm}{dt} + v = (1 - \epsilon)[\rho^{(0)}]^{-1} \frac{dm}{dt} + v \quad . \tag{D.23}$$

We may evaluate the expression for U on either side of the shock front, obtaining the relationship

$$v_1 - v_0 = [\rho^{(0)}]^{-1}(\epsilon_1 - \epsilon_0) \frac{dm}{dt} \tag{D.24}$$

where the subscripts 0 and 1 refer to the front and back sides of the shock. For the shock front that moves into undisturbed material, $v_0 = 0$ and $\epsilon_0 = \epsilon^{(s)}$ so that if we write S for $\frac{dm}{dt}$, we have

$$v_1 = [\rho^{(0)}]^{-1}[\epsilon_1 - \epsilon^{(s)}]S \quad . \tag{D.24a}$$

Equation D.24 is the "kinematic" shock condition, which replaces the automatically satisfied condition of conservation of mass. The equation

* Courant and Friedrichs, Supersonic Flow and Shock Waves, pp. 133-134.

for conserving momentum across the shock is found by equating the net rate of change of momentum across the shock front to the net applied force there. Thus, we have

$$\rho_0(v_0 - U)^2 - \rho_1(v_1 - U)^2 = \sigma_1 - \sigma_0 \quad . \tag{D.25}$$

Using D.23, D.24, and the relation $\rho^{-1} = (1-\epsilon)/\rho^{(o)}$, equation D.25 reduces to

$$\sigma_1 - \sigma_0 = S(v_1 - v_0) \tag{D.26}$$

Again, for the shock front that moves into undisturbed material, $v_0 = o$ and $\sigma_0 = \sigma^{(s)}$ so that

$$\sigma_1 - \sigma^{(s)} = v_1 S \tag{D.26a}$$

Equations D.24 and D.26 will be referred to as the shock equations and in the case mentioned will be specialized to D.24a and D.26a.

D.3 Initial Values and the Linear Solution

The characteristic plane of Fig. D.2 has the characteristic coordinates of r and s. The definition of the coordinates is completed by setting $r = s = t$ on the noncharacteristic curve, $m = o$, corresponding to the upper surface of the material. The other noncharacteristic curve, $\mathcal{S}$, represents the position of the shock front in r-s coordinates. Numerical subscripts will now refer to points in Fig. D.2.

With $\sigma_0 = P + Q$, ϵ_0 is found from Eq. D.9. Since both forms of stress-strain relation hold on the shock, D.9 and D.11 may be equated to give E_0. The shock equations D.24a and D.26a can then be used to give values of v_0 and S_0.

Before the numerical method can be applied, variable values must be obtained at point 1. Series representations for these values are developed in the following discussion. We see that in the case of interest, $P = 0$, the second term of D.9 is exponentially small near the surface. Since the series are to be expanded as functions of m about $m = 0$, D.9 is conveniently approximated by

$$\sigma = A\epsilon^n \tag{D.27}$$

It should be noted that retention of the second term of D.9 in the case $P = 0$, while complicating the algebra, presents no difficulty to the analysis. For simplicity, we shall set $P = 0$ in the discussion and use D.27 as the compressive stress-strain relation. Furthermore, the shock moves into undisturbed material initially so that shock relations D.24a and D.26a apply.

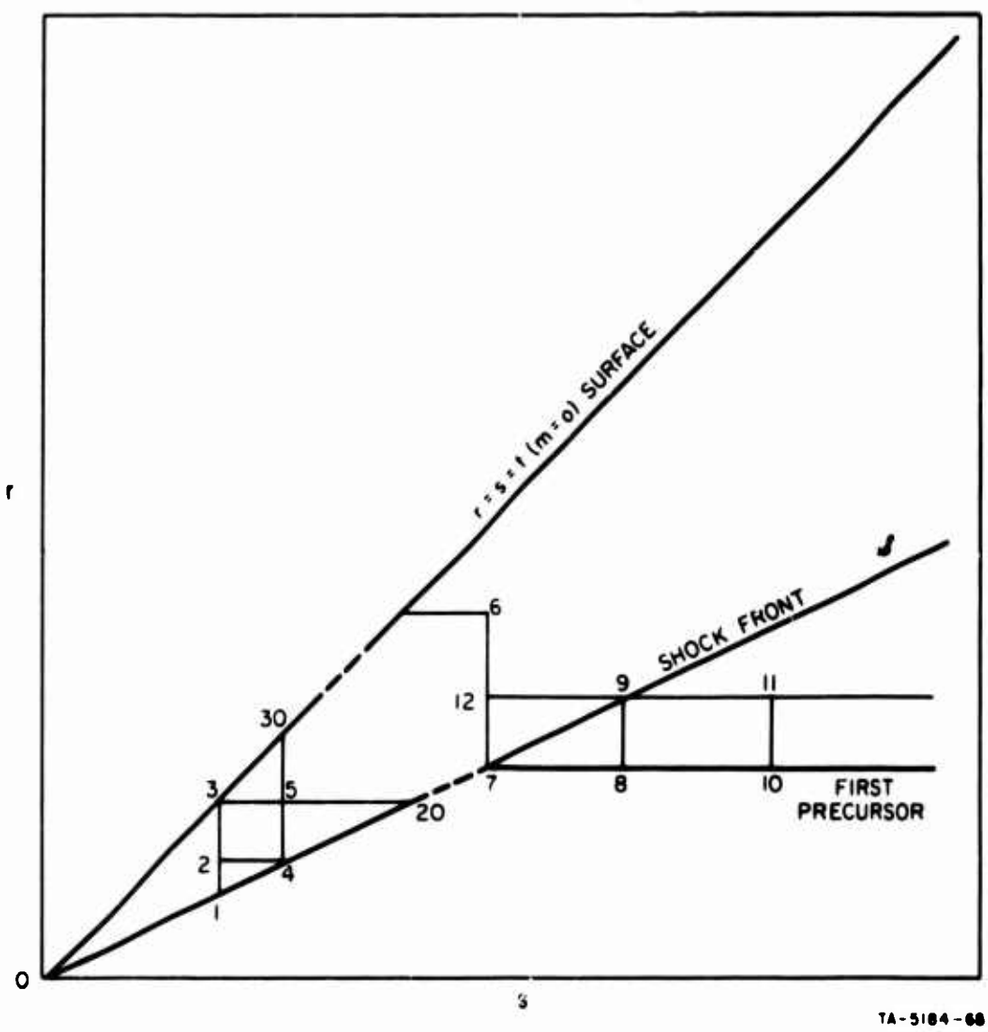

FIG. D.2 THE CHARACTERISTIC PLANE AND POINTS DESIGNATED IN THE ANALYSIS

Since both forms of stress-strain relation hold on the shock, $\epsilon_0 = (Q/A)^N$ and $E_0 = \epsilon_0 - (Q/C)^{N_2}$, where $N = 1/n_2$. The more convenient form of D.11, $\sigma = Q[(\epsilon-E)/(\epsilon_0-E_0)]^{n_2}$, may be linearized in good approximation to

$$\sigma = Q[1 - n_2 + n_2(\epsilon - E)/(\epsilon_0 - E_0)] \tag{D.28}$$

so long as the shock stress and the stress level behind the shock are close.

Using m as the parameter along the shock, define the strain and particle velocity on the shock by $\epsilon = F(m)$ and $v = V(m)$. The shock relations D.24a and D.26a may be rearranged to read

$$S^2 = \rho^{(0)}(AF^n - mg)/[F - (mg/A)^N] \tag{D.29}$$

$$V^2 = (AF^n - mg)[F - (mg/A)^N]/\rho^{(0)} \tag{D.30}$$

Since S is the Lagrangian shock speed, the shock locus $t = T(m)$ is found from

$$T = \int_0^m S^{-1} dm \quad . \tag{D.31}$$

The flow behind the shock is governed by the unloading stress-strain relation D.28 and equations of motion (Eq. G.12 and G.13 of Ref. 4) which read

$$v_t = g - \sigma_m \tag{D.32}$$

$$\epsilon_t = -\rho^{(0)} v_m \quad . \tag{D.33}$$

The use of D.28 permits reduction of the continuous flow equations to

$$\sigma_{tt} = \gamma^2 \sigma_{mm}$$

where $\gamma^2 = \rho^{(0)} Q n_2/(\epsilon_0 - E_0)$. The general solution of this wave equation is conveniently written

$$\sigma = Q[1 + G(m - \gamma t) + H(m + \gamma t)] \tag{D.34}$$

where G and H are functions to be determined.

The stress given by D.34 can now be substituted into the equations governing flow behind the shock.

$$v_t = g - Q[G'(m - \gamma t) + H'(m + \gamma t) \tag{D.35}$$

$$v_m = [-1/\rho^{(0)}]\epsilon_t = -(\epsilon_0 - E_0)\sigma_t/\rho^{(0)} Q n_2 = (Q/\gamma)[G'(m - \gamma t) - H'(m + \gamma t)] \tag{D.36}$$

where the primes represent differentiation with respect to the arguments, $m - \gamma t$ and $m + \gamma t$.

Using the shock front as a reference point, D.35 can be integrated with respect to t,

$$v = V + g(t - T) + (Q/\gamma)[G(m - \gamma t) - G(m - \gamma T) - H(m + \gamma t) + H(m + \gamma T)] \quad , \tag{D.37}$$

and differentiated with respect to m to give

$$v_m = V' - gT' + (Q/\gamma)[G'(m - \gamma t) - (1 - \gamma T')G'(m - \gamma T)$$

$$- H'(m + \gamma t) + (1 + \gamma T')H'(m + \gamma T)] \quad . \tag{D.38}$$

The result of equating D.36 and D.38 is

$$(1 - \gamma T')G'(m - \gamma T) - (1 + \gamma T')H'(m + \gamma T) = (\gamma/Q)(V' - gT')$$

which can be integrated giving

$$G(m - \gamma T) - H(m + \gamma T) = (\gamma/Q)[V - V(0) - gT] \quad . \tag{D.39}$$

Also, on the shock $\sigma = AF^n$ and $t = T$ so that

$$1 + G(m - \gamma T) + H(m + \gamma T) = (A/Q)F^n \quad . \tag{D.40}$$

Equations D.39 and D.40 can be simplified by noting that at the surface $\sigma = Qe^{-t/T_0}$ so that

$$1 + G(-\gamma t) + H(\gamma t) = e^{-t/T_0}$$

or more generally

$$1 + G(-x) + H(x) = e^{-x/(\gamma T_0)} \tag{D.41}$$

Thus, H may be eliminated from D.39 and D.40 to give

$$G(m - \gamma T) + G(-m - \gamma T) = (\gamma/Q)[V - V(0) - gT] + e^{-(m+\gamma T)/(\gamma T_0)} \tag{D.42}$$

and

$$G(m - \gamma T) - G(-m - \gamma T) + e^{-(m+\gamma T)/(\gamma T_0)} = (A/\gamma)F^n \tag{D.43}$$

From the forms of S, V, and T as functions of F and m, it may be surmised that, with two term accuracy, $F = \epsilon_0 + F_1 m^N$. From this, putting $x = m^N/\epsilon_0$ and $\delta = (g/A)^N$, one finds

$$S = S_0\{1 + [(n - 1)F_1 + \delta](x/2)\} \ , \ S_0^2 = \rho^{(0)}Q/\epsilon_0$$

$$V = V_0\{1 + [(n + 1)F_1 - \delta](x/2)\} \ , \ V_0^2 = Q\epsilon_0/\rho^{(0)}$$

$$T = (m/S_0)\{1 - [n/2(n + 1)][(n - 1)F_1 + \delta]x\} \quad .$$

To the same accuracy, $G(m) = G_1 \cdot (-m)^N$ so that putting

$$p = (\gamma/S_0 - 1)^N - (\gamma/S_0 + 1)^N \qquad q = (\gamma/S_0 - 1)^N + (\gamma/S_0 + 1)^N$$

D.42 and D.43 read

$$pG_1 = nF_1/\epsilon_0$$

$$qG_1 = (\mu/\epsilon_0)[(n + 1)F_1 - \delta] \quad , \quad \mu = \rho V_0/2Q \quad .$$

From these G_1 may be eliminated giving, finally,

$$F_1 = \mu\delta p/[\mu(n + 1)p - nq] \quad .$$

With F_1 known, values for F, S, V, and T at point 1 are obtained as functions of m_1 by using the above expressions. Of course, m_1 must be made small enough so that resulting values of F, S, V, and T are consistent with the simplifications made in the stress-strain relations D.9 and D.11.

Linear Model

The above results can be extended to yield an analytic description of the flow if $n = n_2 = 1$ and $B = 0$. In this case,

$$S_0^2 = \rho^{(0)}A$$

$$V^2 = A(F - mg\,A)^2\,\rho^{(0)}$$

$$T = m\,S_0$$

$$\gamma^2 = \rho^{(0)}C \quad .$$

Define $\quad R = \gamma/S_0$, (note that $R > 1$)

$$\xi = -m(R - 1)$$

$$\eta = -m(R + 1)$$

$$k = (R - 1)/(R + 1) \quad .$$

Then D.42 and D.43 read

$$G(\xi) + G(\eta) = \frac{\gamma}{Q}\left\{\sqrt{\frac{A}{\rho^{(0)}}}\,[F(m) - F(0)] - \frac{2mg}{S_0}\right\} + e^{\eta/(\gamma T_0)} - 1$$

$$G(\xi) - G(\eta) + e^{\eta/(\gamma T_0)} = \frac{A}{Q}F(m)$$

Remembering that $F(o) = Q/A$, eliminate $F(m)$ from the above equations and reduce to

$$G(k\eta) = \frac{G(\eta)}{k} - \frac{2gR\eta}{Q(R^2 - 1)} - \frac{e^{\eta/(\gamma T_0)} - 1}{k}$$

Transform by letting $M(\ln|z|) = G(z)$, for $z < o$ to obtain

$$M(\ln|\eta| + \ln k) = \frac{M(\ln|\eta|)}{k} + \frac{2gR|\eta|}{Q(R^2 - 1)} - \frac{e^{-|\eta|/(\gamma T_0)} - 1}{k}$$

With $d = -\ln k$, transform again according to $y = \ln|\eta|$ obtaining the difference equation

$$M(y - d) = \frac{M(y)}{k} + h(y) \qquad \text{(D.44)}$$

where

$$h(y) = \left[\frac{2gR}{Q(R^2 - 1)}\right]e^{y} - \frac{1}{k}\left[e^{-e^{y}/(\gamma T_0)} - 1\right]$$

It follows that $M(-\infty) = o$. A simple recursive process yields

$$k^n M(y - nd) = M(y) + k\sum_{j=0}^{n-1} k^j h(y - jd)$$

which in the limit as $n \to \infty$ reduces to

$$M(y) = -k\sum_{j=0}^{\infty} k^j h(y - jd)$$

or, in terms of G, η, and k

$$G(\eta) = -k\sum_{j=0}^{\infty} k^j h(\ln|\eta| + j\ln k) \quad . \qquad \text{(D.45)}$$

The series in D.45 converges exponentially, allowing efficient numerical evaluation of the function G. The values of the flow variables are then easily obtained as follows:

Equation D.41 is a functional relationship between G and H so that we may consider them equally available. From D.29 and D.31

$$T = m/\sqrt{\rho^{(0)}A} \qquad \text{(D.46)}$$

so that in the m-t plane the shock locus is a straight line. Then D.40 may be solved for F, giving

$$F = (Q/A)[1 + G(m - \gamma T) + H(m + \gamma T)] \tag{D.47}$$

With F known, Eq. D.30 reads

$$V = (AF - mg)/\sqrt{\rho^{(0)}A} \tag{D.48}$$

Thus, the variable values on the shock are given by D.46, D.47 and D.48. Behind the shock, v is obtained directly from Eq. D.37. Equating the shock relations gives $E = F(1 - A/C)$ so that ϵ may be obtained from D.34 as

$$\epsilon = E + (Q/C)[1 + G(m - \gamma t) + H(m + \gamma t)] \tag{D.49}$$

With G given then, the flow on and behind the shock is known completely.

D.4 Numerical Method

With the applied stress given by Eq. D.1, discontinuities in stress and particle velocity will be propagated from the surface at time $t = 0$ down into the medium in the form of a shock front. Initially, the shock will be moving into quiescent material so that flow computations must be performed only for points at the surface, in the continuous flow region behind the shock, and on the shock itself. However, at greater depths, the form of the compressive stress-strain relation allows the formation of sound waves, which precede the shock into the material below. In general then, provision must be made for computation of the flow variables at points

(1) on the surface,
(2) in the continuous flow regions behind and ahead of the shock,
(3) on the shock moving into quiescent material,
(4) on the shock moving into continuous flow, and
(5) on the first precursor, i.e., the sound wave moving into quiescent material.

The points referred to in the following discussion are located in Fig. D.2. Each of the specific points mentioned represents a typical calculation.

I - The Surface

With conditions at a general point 5 in the flow known, the flow variables are computed at point 30 by an iterative process, involving Eqs. D.21a, D.22a, the unloading relation, D.11, and the surface stress, D.1:

$$t_{30}^{(k)} = t_5 + m_5 / c_5^{(k-1)}$$

$$\sigma_{30}^{(k)} = P + Q[\exp(-t_{30}^{(k)}/T_0)]$$

$$\epsilon_{30}^{(k)} = E_0 + [\sigma_{30}^{(k)}/C]^{N_2}$$

$$v_{30}^{(k)} = v_5 + \frac{c_1^{(k-1)}}{\rho^{(0)}} (\epsilon_{30}^{(k)} - \epsilon_5) + [g - R_5^{(k-1)}](t_{30}^{(k)} - t_5)$$

where $f(\epsilon,m)$ is given by (7), $c(\epsilon,m) = [\rho^{(0)} f_\epsilon(\epsilon,m)]^{1/2}$ and

$$c_5^{(k)} = c\left\{\frac{1}{2}[\epsilon_5 + \epsilon_{30}^{(k)}], \frac{1}{2} m_5\right\}$$

$$c_5^{(0)} = c_5$$

$$R_5^{(k)} = f_m\left\{\frac{1}{2}[\epsilon_5 + \epsilon_{30}^{(k)}], \frac{1}{2} m_5\right\}$$

$$R_5^{(0)} = (f_m)_5$$

The procedure is repeated until successive iterates agree to some prescribed precision.

II - The Continuous Flow Regions

In the continuous flow region ahead of the shock, the strain rate, ϵ_t, is positive while behind the shock it is negative. The calculations in the two regions differ only in the choice of stress-strain relation, which must there reflect the sign of ϵ_t. The function $E(m)$ is computed at points on the shock as part of the shock calculations. Values of E used in the unloading relation behind the shock are interpolates of the shock values.

With conditions known at points 3 and 4, the flow variables are calculated at point 5 by iteration of the coefficients, c and f_m,

in Eqs. D.19a - D.22a. The iteration scheme is conveniently written

$$m_5^{(k)} - m_3 = c_3^{(k-1)}[t_5^{(k)} - t_3]$$

$$m_5^{(k)} - m_4 = -c_4^{(k-1)}[t_5^{(k)} - t_4]$$

$$v_5^{(k)} - v_3 + [c_3^{(k-1)}/\rho^{(0)}][\epsilon_5^{(k)} - \epsilon_3] = [g - R_3^{(k-1)}][t_5^{(k)} - t_3]$$

$$v_5^{(k)} - v_4 - [c_4^{(k-1)}/\rho^{(0)}][\epsilon_5^{(k)} - \epsilon_4] = [g - R_4^{(k-1)}][t_5^{(k)} - t_4]$$

where

$$c_{3,4}^{(k)} = c\{0.5[\epsilon_{3,4} + \epsilon_5^{(k)}],\ 0.5[m_{3,4} + m_5^{(k)}]\}$$

$$c_{3,4}^{(0)} = c_{3,4}$$

$$R_{3,4}^{(k)} = f_m\{0.5[\epsilon_{3,4} + \epsilon_5^{(k)}],\ 0.5[m_{3,4} + m_5^{(k)}]\}$$

$$R_{3,4}^{(0)} = (f_m)_{3,4}$$

The process is continued until successive iterates agree to some prescribed precision.

For interior points such as 2, the flow variables are taken as interpolates of the variables at points 1 and 3, i.e., if X represents any of the variables m, t, v, or ϵ then $X_2 = \xi X_1 + (1 - \xi)X_3$. The interpolation constant ξ is chosen so that the mesh remains uniform along the shock front.

III - The Shock Moving into Quiescent Material

If the conditions are known at point 5 behind the shock and point 4 on the shock, then the flow variables at point 20, the intersection of the shock with the horizontal characteristic (see Fig. D.2) through point 5, satisfy the following set of difference equations:

$$m_{20} - m_5 = \bar{c}(t_{20} - t_5)$$

$$v_{20} - v_5 + \frac{\bar{c}}{\rho^{(0)}}(\epsilon_{20} - \epsilon_5) = (g - \bar{f}_m)(t_{20} - t_5)$$

$$\frac{1}{2}(S_4 + S_{20}) = (m_{20} - m_4)/(t_{20} - t_4)$$

$$\rho^{(0)} v_{20} = [\epsilon_{20} - \epsilon_{20}^{(s)}] S_{20}$$

$$\sigma_{20} - \sigma_{20}^{(s)} = v_{20} S_{20}$$

where σ_{20} is defined by D.9 and

$$\bar{c} = c\left[\frac{1}{2}(\epsilon_5 + \epsilon_{20}),\ \frac{1}{2}(m_5 + m_{20})\right]$$

$$\bar{f}_m = \bar{f}_m\left[\frac{1}{2}(\epsilon_5 + \epsilon_{20}),\ \frac{1}{2}(m_5 + m_{20})\right]$$

Since $\bar{c}$ and $\bar{f}_m$ represent conditions behind the shock it is understood that the unloading relation applies in their evaluation.

The variables v_{20}, t_{20}, and S_{20} may be eliminated from the above set leaving two equations that can be solved numerically for ϵ_{20} and m_{20}. Since both forms of stress-strain relation hold on the shock, D.9 and D.11 may be equated to give E_{20}. Back substitution into the original set of equations yields the remaining flow values.

IV - The Shock Moving into Continuous Flow

The vertical characteristic through point 8 meets the shock locus at point 9. The horizontal characteristic that intersects the shock locus at point 9 passes through some point 12, whose variables are defined by

$$X_{12} = \xi X_{7L} + (1 - \xi) X_6$$

where X is written for m, t, v and ϵ. The two equations along the horizontal characteristic,

$$m_9 - m_{12} = c_L(t_9 - t_{12})$$

$$v_{9L} - v_{12} + \frac{c_L}{\rho^{(0)}}(\epsilon_{9L} - \epsilon_{12}) = (g - R_L)(t_9 - t_{12})$$

the two equations along the vertical characteristic,

$$m_9 - m_8 = c_R(t_9 - t_8)$$

$$v_{9R} - v_{12} - \frac{c_R}{\rho^{(0)}}(\epsilon_{9R} - \epsilon_8) = (g - R_R)(t_9 - t_8)$$

and the two shock equations

$$\rho^{(0)}(v_{9R} - v_{9L}) = (\epsilon_{9R} - \epsilon_{9L})S_9$$

$$\sigma_{9R} - \sigma_{9L} = (v_{9R} - v_{9L})S_9 \cdot$$

provide six more relations. A second order difference form of the shock speed is

$$0.5(S_9 + S_7) = (m_9 - m_7)/(t_9 - t_7)$$

In addition, the shock speed and the sound speed at the front face of the shock are equal, giving

$$f_\epsilon(\epsilon_{9R}, m_9) = (\sigma_{9R} - \sigma_{9L})/(\epsilon_{9R} - \epsilon_{9L})$$

for a total of twelve equations in the twelve variables m_{12}, t_{12}, v_{12}, ϵ_{12}, m_9, t_9, v_{9R}, ϵ_{9R}, ϵ_{9L}, S_9 and ξ. The subscripts L and R on the variables v, ϵ and σ indicate the left and right sides of the shock locus, S . Also

$$c_L = c\left[\frac{1}{2}(\epsilon_{12} + \epsilon_{9L}), \frac{1}{2}(m_{12} + m_9)\right], \quad f(\epsilon, m) \text{ given by (D.11)}$$

$$c_R = c\left[\frac{1}{2}(\epsilon_{9R} + \epsilon_8), \frac{1}{2}(m_9 + m_8)\right], \quad f(\epsilon, m) \text{ given by (D.9)}$$

$$R_L = f_m\left[\frac{1}{2}(\epsilon_{12} + \epsilon_{9L}), \frac{1}{2}(m_{12} + m_9)\right], \quad f(\epsilon, m) \text{ given by (D.11)}$$

$$R_R = f_m\left[\frac{1}{2}(\epsilon_{9R} + \epsilon_8), \frac{1}{2}(m_9 + m_8)\right], \quad f(\epsilon, m) \text{ given by (D.9)}$$

The system can be reduced to four equations in m_9, ϵ_{9L}, ϵ_{9R}, and ξ and solved numerically. Back substitution yields the remaining variables. It should be noted that if $\xi < 0$ then point 12 is not physically between points 6 and 7 in Fig. D.2.

V - The First Precursor

On the leading precursor $\epsilon = \epsilon^{(s)}(m)$ so that

$$\bar{c} = c\left[\frac{1}{2}(\epsilon_{7R} + \epsilon_8),\ \frac{1}{2}(m_7 + m_8)\right]$$

$$\bar{R} = f_m\left[\frac{1}{2}(\epsilon_{7R} + \epsilon_8),\ \frac{1}{2}(m_7 + m_8)\right]$$

$$m_8 - m_7 = \bar{c}(t_8 - t_7)$$

$$v_8 - v_{7R} + \frac{\bar{c}}{\rho^{(0)}}(\epsilon_8 - \epsilon_{7R}) = (g - \bar{R})(t_8 - t_7)$$

may be solved as a function of m_8. The function $f(\epsilon,m)$ used in the evaluation of $\bar{c}$ and $\bar{R}$ is given by (D.9).

Logic of the Method

It can be observed that there is a certain freedom of direction in the solution in the continuous flow regions. That is, this solution may be carried out along the vertical characteristics toward the surface or along the horizontal characteristics to deeper points. This corresponds to obtaining information near the surface over long time intervals or at greater depths for shorter periods. Since there is little interest in the flow near the surface, the organization of the computation is such as to obtain the flow information as economically as possible at the greater depths of the material by integrating along the horizontal characteristics.

D.5 Results and Discussion

Results were obtained using that part of the computer program that was complete at the close of the project. The program was developed by steps in such a way that useful information could be obtained at the conclusion of each step. First, the program was written to handle an applied loading with a shock front followed by a decay in pressure. The soil considered followed the simple relation shown in Eq. (D.6), $\tau = A\epsilon^n$. This step was completed. Then the more complex relation of Eq. (D.9) was used for the soil. This relation introduced a precursor, which breaks away from the shock front at some depth and which added considerable difficulty to the solution. At the close of the project, the program could handle the break-away of the precursor but could not follow it very far.

Several calculations were made for the simple nonlinear solid defined by Eq. (D.6) that is, for the solid with a purely concave stress-strain relation. The attenuation of stress and particle velocity were affected by curvature (n), geostatic stress, duration of loading, and stress level. The unique feature of these calculations is the capacity to account for geostatic stress, the initial static stress due to the weight of the soil above.

Curvature of the stress-strain relation is required for the geostatic stress to have any effect on the wave propagation phenomena. That is, if there is no curvature, there is no geostatic effect. In combination, increasing curvature (n) and increasing geostatic stress tend to decrease the attenuation rate. This trend can be seen in Figs. D.3 and D.4. The ordinates are the peak stress at any depth divided by the peak applied stress, or the peak particle velocity at any depth divided by the peak particle velocity at the surface. The abscissas are nondimensional arrival time: arrival time of the peak stress or particle velocity divided by the duration, T_0, of the applied stress. The calculations were made for geostatic stress caused by a soil density of $\rho = 1.6$ gm/cm^3 or for $\rho = o$, the case of no geostatic stress. From these two figures, the curvature and geostatic stress have different effects on stress and particle velocity attenuation and the effects are different for $\alpha = 0.2$ and $\alpha = 0.3$.

Becuase geostatic stress is important, so is the applied stress level, as shown in Figs. D.5 and D.6. An increase in the ratio of geostatic stress to peak applied stress appears to decrease the attenuation rate. The stress level has only a small effect on particle velocity attenuation. The curve for no geostatic stress is shown for comparison in each figure.

The duration, T_0, of the loading also affects attenuation because of the importance of geostatic stress (see Figs. D.7 and D.8). The nondimensional depth, T/T_0, eliminates the duration as a parameter for the case where there is no geostatic stress. But it also brings together many real depths at the same abscissa. For instance, at $T/T_0 = 4$, twice as much depth is involved for the $T_0 = 10$ msec as for

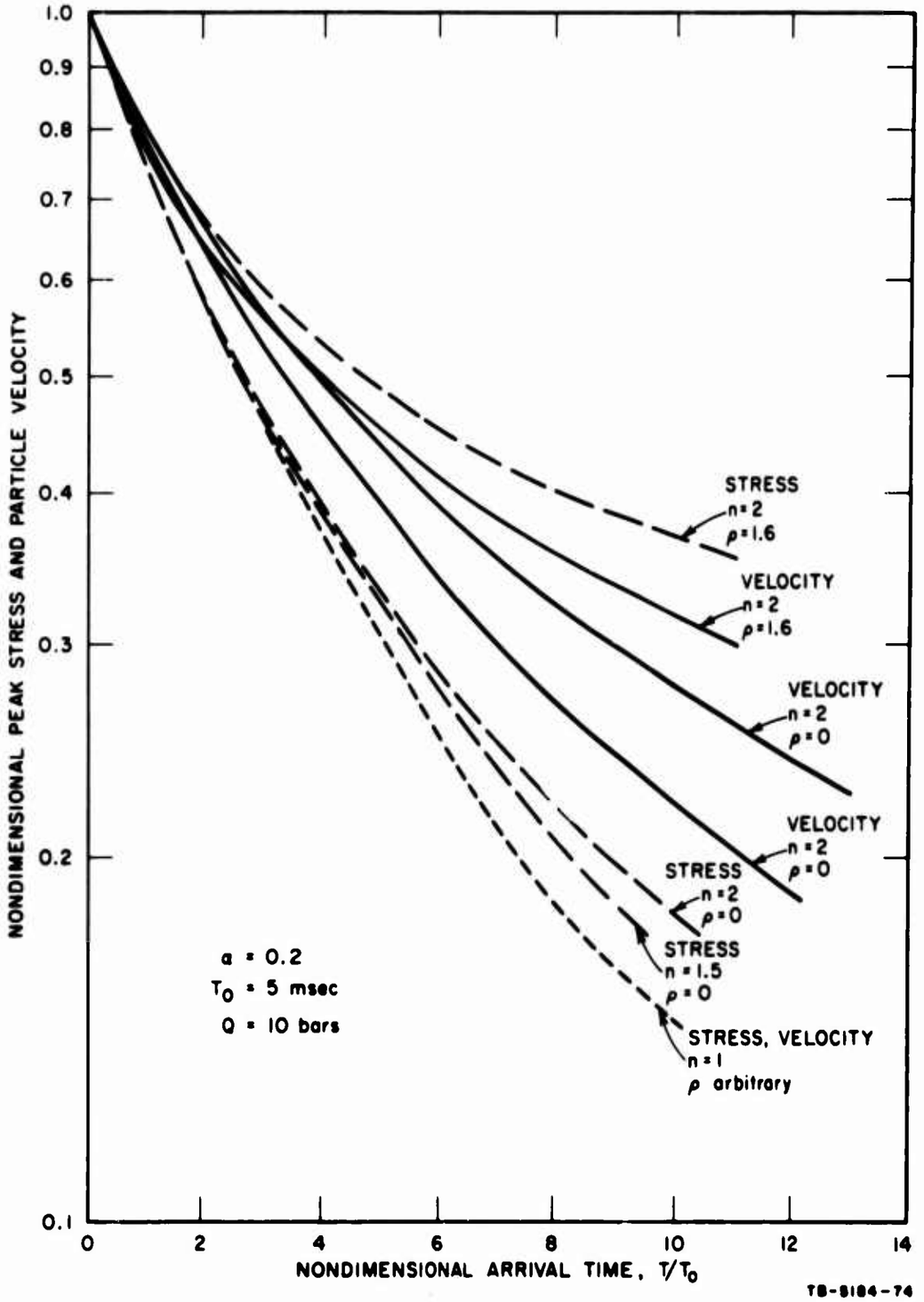

FIG. D.3 EFFECT OF CURVATURE AND GEOSTATIC STRESS ON ATTENUATION

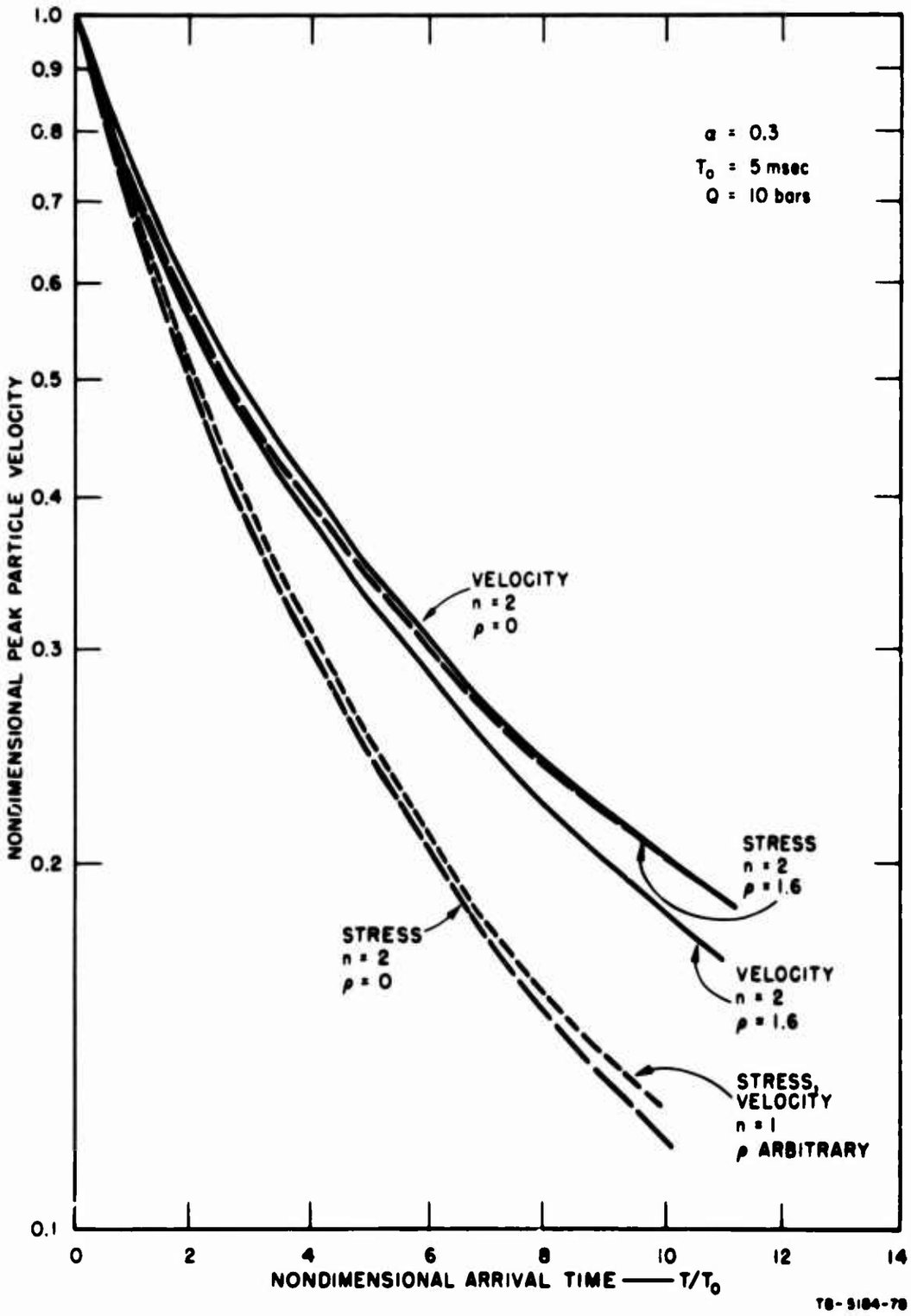

FIG. D.4 EFFECT OF CURVATURE AND GEOSTATIC STRESS ON ATTENUATION

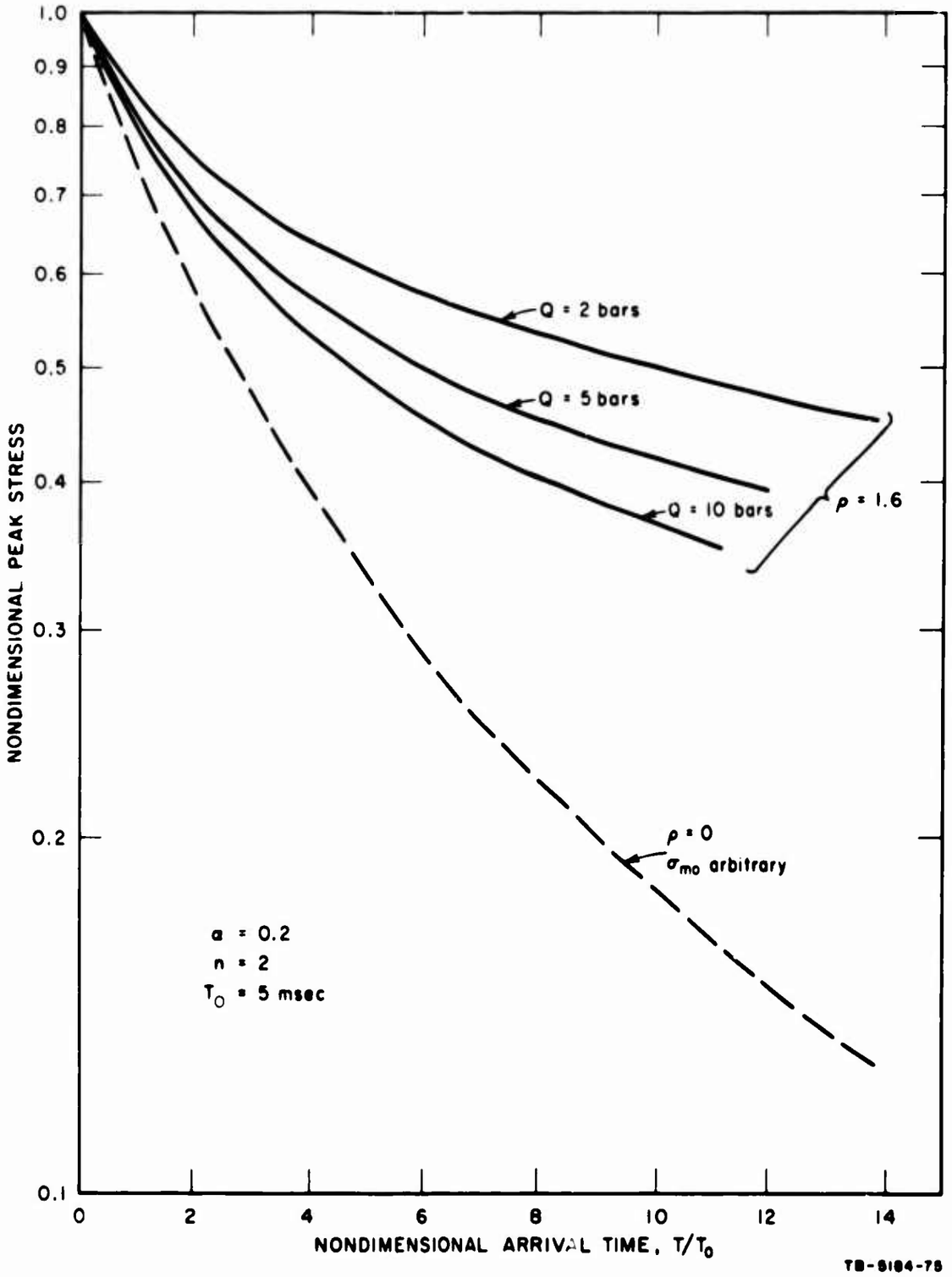

FIG. D.5 EFFECT OF STRESS LEVEL ON STRESS ATTENUATION

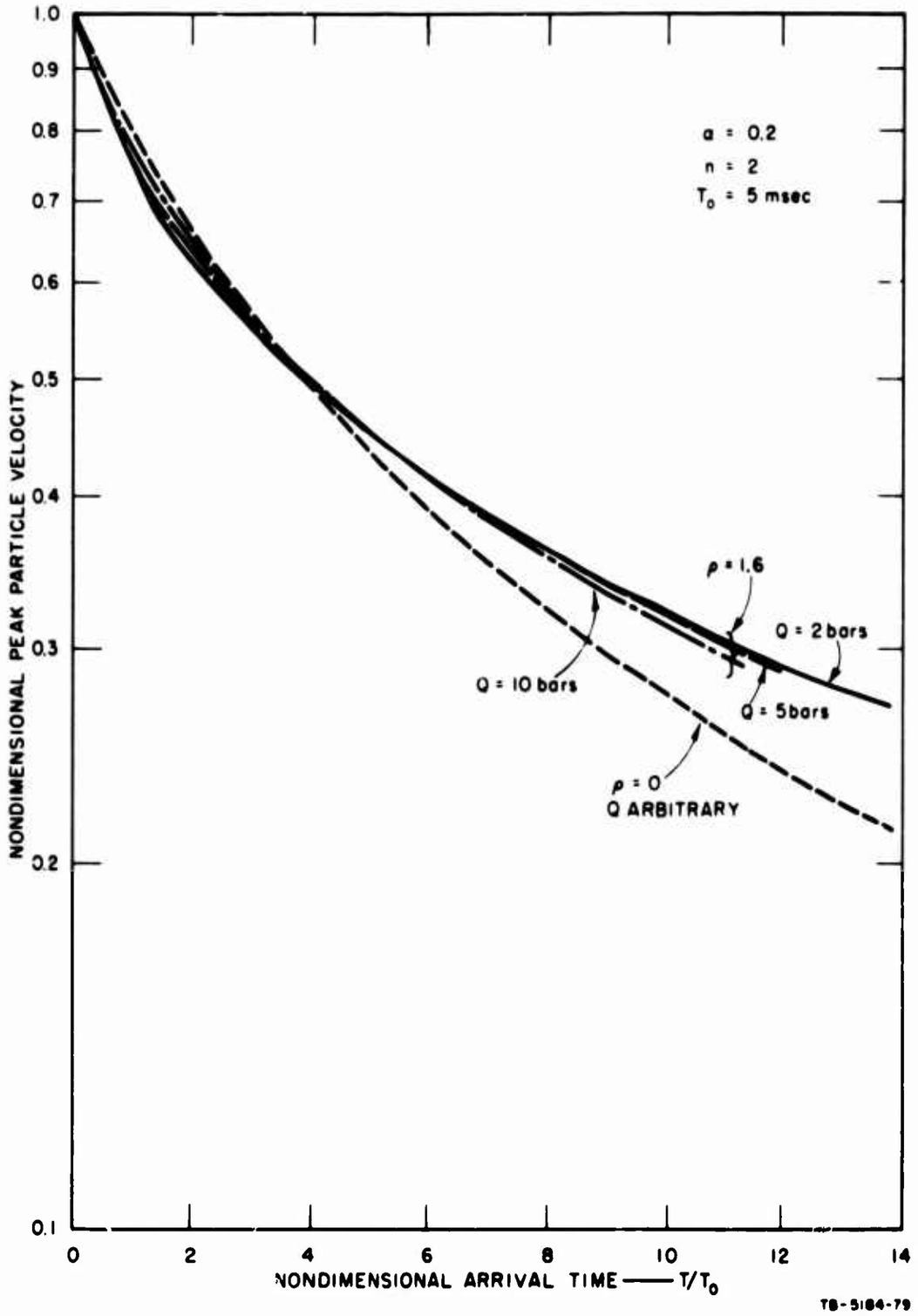

FIG. D.6 EFFECT OF STRESS LEVEL ON PARTICLE VELOCITY ATTENUATION

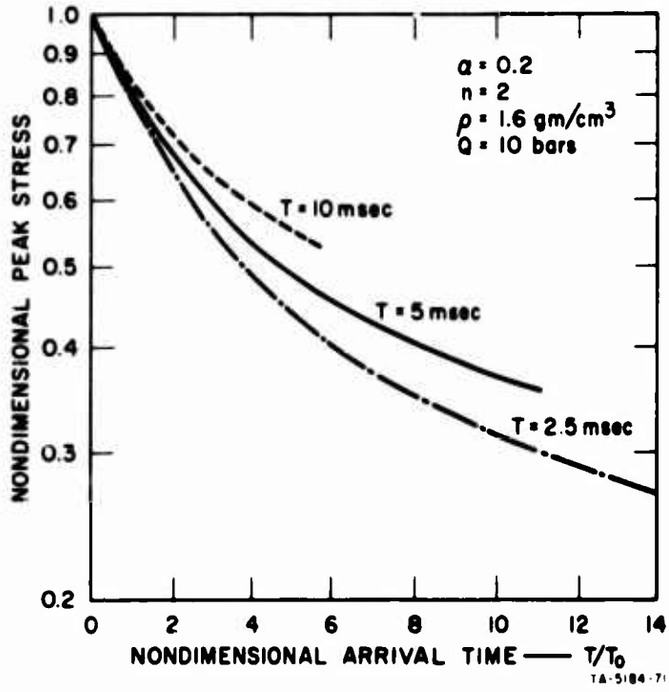

FIG. D.7 EFFECT OF APPLIED STRESS DURATION ON STRESS ATTENUATION

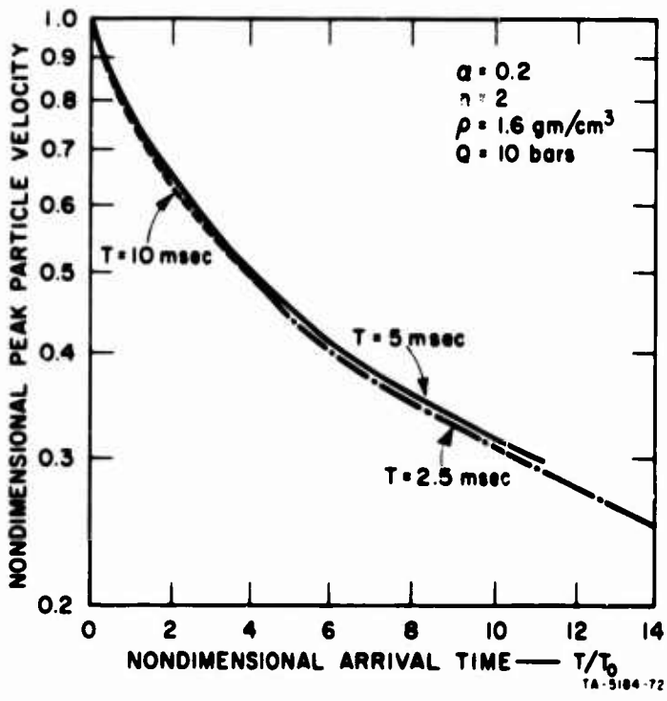

FIG. D.8 EFFECT OF APPLIED STRESS DURATION PARTICLE VELOCITY ATTENUATION

the 5 msec case. Hence, also twice as much geostatic stress is involved. Since stress attenuation is generally reduced by geostatic stress, we would expect that longer durations would diminish attenuation: this is verified in Fig. D.7. The next figure shows that particle velocity is almost completely insensitive to the duration of loading.

We may conclude from this study that, for soil with a marked curvature in the stress-strain relation, geostatic stress will be quite important. It will be necessary to specialize an attenuation prediction to the stress level, duration, and unit weight of soil as well as for the values of σ and n.

REFERENCES

1. Lai, W. and F. M. Sauer, Propagation of Stress Pulses in Linear Viscoelastic Materials, Stanford Research Institute, Project PHU-2917, Final Report, Part I, DASA 1266-1, August 1961.

2. Kriebel, H. W., Feasibility Study of an Experimental Apparatus for Unidimensional Stress Propagation in Soil, Stanford Research Institute, Project PHU-2917, Final Report, Part II, DASA 1266-2, February 1962.

3. Seaman, L., G. N. Bycroft, and H. W. Kriebel, Stress Propagation in Soils, Stanford Research Institute, Project PHU-2917, Final Report, Part III, DASA 1266-3, November 1963.

4. Seaman, L. and R. V. Whitman, Stress Propagation in Soils, Stanford Research Institute, Project PHU-2917, Final Report, Part IV, DASA 1266-4, June 1964.

5. Selig, E. T., Shock-Induced Stress Wave Propagation in Sand, Ph.D. thesis, Dept. of Civil Engineering, Illinois Institute of Technology, Chicago, January 1964.

6. McNeill, Robert L., A Study of the Propagation of Stress Waves in Sand, Sc.D. thesis to the Department of Mechanical Engineering, University of New Mexico, Albuquerque, New Mexico, 1965.

7. Heierli, Werner, Inelastic Wave Propagation in Soil Columns, Proc. ASCE, Paper No. 3347, (SM-6), December 1962.

8. Whitman, R. V., The Behavior of Soils under Transient Loadings, Proc. Fourth International Conference on Soil Mechanics and Foundation Engineering, Butterworths Scientific Publications, London, 1957.

9. Zaccor, James V. and N. R. Wallace, Techniques and Equipment for Determining Dynamic Properties of Soils, URS Corporation, Burlingame, California, Final Report, DASA 1421, November 1963.

10. Salvadori, Mario G., Richard Skalak, and Paul Weidlinger, Waves and Shocks in Locking and Dissipative Media, Trans. Amer. Soc. of Civil Engin., 126, Part I, 1961, p. 305.

11. Skalak, Richard and Paul Weidlinger, Attenuation of Stress Waves in Bilinear Materials, ibid, 127, Part I, 1962, p. 352.

12. Weidlinger, Paul and Alva T. Matthews, Shock and Reflection in a Nonlinear Medium, Proc. of the Amer. Soc. of Civil Engin., Paper No. 4375, (EM-3), 1.147, June 1965.

13. Kondner. Robert L. and Raymond J. Krizek, A Rheological Investigation of the Dynamic Response Spectra of Soils, Report 2: A Response Spectra Formulation for a Cohesive Soil, Technological Institute of Northwestern University, for U.S. Army Engineers Waterways Experiment Station, August 1963.

14. Kondner, Robert L. and Michael M. K. Ho, A Rheological Investigation of the Dynamic Response Spectra of Soils, Report 3: Energy Dissipation Response of a Cohesive Soil, The Technological Institute of Northwestern University, for U.S. Army Engineers Waterways Experiment Station, June 1964.

15. Christensen, Richard W. and Tien Hsing Wu, Analysis of Clay Deformation as a Rate Process, American Society of Civil Engineers, Jour of the Soil Mechanics and Foundation Division, Vol. 90, SM 6, p. 125, November 1964.

16. Whitman, Robert V., The Response of Soils to Dynamic Loading, Report 17: Stress-Strain-Time Behavior of Soil in One-Dimensional Compression, Department of Civil Engineering, Massachusetts Institute of Technology Report No. R63-25 for U.S. Army Waterways Experiment Station, May 1963.

17. Mason, H. G., O. H. Criner, R. Waissar, and N. R. Wallace, A Study of the Dynamic Soil-Structure Interaction Characteristics of Real Soil Media, Paper presented to Amer. Soc. of Civil Engineers Conference in San Francisco, California, October 1963, printed as a report by United Research Services, Burlingame, California.

18. Zaccor, J. V., N. R. Wallace, W. L. Durbin, and H. G. Mason, Study of Dynamic Stress-Strain and Wave Propagation Characteristics of Soil, Report 4: Concepts of Shock Behavior in a Granular Medium, URS Corporation, Burlingame, California, for Waterways Experiment Station, Vicksburg, Mississippi, Report No. 3-91, March 1965.

19. Witherly, T. D., Instruments for Measurement of Dusty Airblast Effects in High Pressure Regions, Final Report for Phase V, DASA 1433, September 1963.

20. Jackson, J. G., Jr. and P. F. Hadala, Dynamic Bearing Capacity of Soils, Report 3: The Application of Similitude to Small-Scale Footing Tests, Report for DASA by Waterways Experiment Station, Vicksburg, Mississippi, December 1964.

21. Moore, Peter J., One-Dimensional Compression and Wave Propagation in a Sand, Sc.D. thesis, Massachusetts Institute of Technology, Department of Civil Engineering, September 1963.

REFERENCES (Continued)

22. Bland, D. R., The Theory of Linear Viscoelasticity, Pergamon Press, London, 1960.

23. Hardin, B. O. and F. E. Richart, Jr., Elastic Wave Velocities in Granular Soils, Journal of Soil Mechanics and Foundations Division, Proc. ASCE, 89, (SM-1), Part I, February 1963, pp. 33-65.

24. Courant, R. and K. O. Friedrichs, Supersonic Flow and Shock Waves, Interscience Publishers, New York, 1958.

BLANK PAGE

UNCLASSIFIED
Security Classification

DOCUMENT CONTROL DATA · R&D

(Security classification of title, body of abstract and indexing annotation must be entered when the overall report is classified)

1. ORIGINATING ACTIVITY *(Corporate author)* Stanford Research Institute Menlo Park, California	2a. REPORT SECURITY CLASSIFICATION UNCLASSIFIED 2b. GROUP

3. REPORT TITLE

One-Dimensional Stress Wave Propagation in Soils

4. DESCRIPTIVE NOTES *(Type of report and inclusive dates)*

Final Report, September 1964 to December 1965

5. AUTHOR(S) *(Last name, first name, initial)*

Seaman, Lynn

6. REPORT DATE February 1966	7a. TOTAL NO. OF PAGES 165	7b. NO. OF REFS 24
8a. CONTRACT OR GRANT NO. DA 49-146-XZ-343 b. PROJECT NO. c. d.	9a. ORIGINATOR'S REPORT NUMBER(S) Final Report, Project PHU-5184 9b. OTHER REPORT NO(S) *(Any other numbers that may be assigned this report)*	

10. AVAILABILITY/LIMITATION NOTICES

Distribution of this document is unlimited.

11. SUPPLEMENTARY NOTES	12. SPONSORING MILITARY ACTIVITY Defense Atomic Support Agency

13. ABSTRACT

Soil behavior during stress wave propagation was studied on a sand and two clays by making one-dimensional wave propagation tests on 5-meter long columns of the soils. Attempts were made to predict this behavior by determining soil properties in dynamic compression tests on small samples and by using these properties in a variety of mathematical models for soils.

In all the wave propagation tests, stress and acceleration records were very similar, showing that the three soils differ in degree, not in kind. Peak stress and particle velocity attenuated to 20-40% of the peak value in the length of the 5-meter column.

Two theoretical soil models were analyzed: one to investigate the effect of combined time-dependent and time-independent dissipation, and one to study the effects of nonlinear stress-strain relations and geostatic stress. Comparison of the theoretical predictions from the first of these and two previously studied models (using properties obtained from compression tests on soil samples) with the wave propagation results shows

1. For clays the arrival time of the wave at the column base was within 10% of that calculated from the tangent modulus, and for sand it was within 25%.
2. Attenuation of peak stress and particle velocity was predicted within ±50% at the base of the column (5-meter length).

DD FORM 1 JAN 64 1473

UNCLASSIFIED
Security Classification

14. KEY WORDS	LINK A ROLE	LINK A WT	LINK B ROLE	LINK B WT	LINK C ROLE	LINK C WT

INSTRUCTIONS

1. ORIGINATING ACTIVITY: Enter the name and address of the contractor, subcontractor, grantee, Department of Defense activity or other organization *(corporate author)* issuing the report.

2a. REPORT SECURITY CLASSIFICATION: Enter the overall security classification of the report. Indicate whether "Restricted Data" is included. Marking is to be in accordance with appropriate security regulations.

2b. GROUP: Automatic downgrading is specified in DoD Directive 5200.10 and Armed Forces Industrial Manual. Enter the group number. Also, when applicable, show that optional markings have been used for Group 3 and Group 4 as authorized.

3. REPORT TITLE: Enter the complete report title in all capital letters. Titles in all cases should be unclassified. If a meaningful title cannot be selected without classification, show title classification in all capitals in parenthesis immediately following the title.

4. DESCRIPTIVE NOTES: If appropriate, enter the type of report, e.g., interim, progress, summary, annual, or final. Give the inclusive dates when a specific reporting period is covered.

5. AUTHOR(S): Enter the name(s) of author(s) as shown on or in the report. Enter last name, first name, middle initial. If military, show rank and branch of service. The name of the principal author is an absolute minimum requirement.

6. REPORT DATE: Enter the date of the report as day, month, year; or month, year. If more than one date appears on the report, use date of publication.

7a. TOTAL NUMBER OF PAGES: The total page count should follow normal pagination procedures, i.e., enter the number of pages containing information.

7b. NUMBER OF REFERENCES: Enter the total number of references cited in the report.

8a. CONTRACT OR GRANT NUMBER: If appropriate, enter the applicable number of the contract or grant under which the report was written.

8b, 8c, & 8d. PROJECT NUMBER: Enter the appropriate military department identification, such as project number, subproject number, system numbers, task number, etc.

9a. ORIGINATOR'S REPORT NUMBER(S): Enter the official report number by which the document will be identified and controlled by the originating activity. This number must be unique to this report.

9b. OTHER REPORT NUMBER(S): If the report has been assigned any other report numbers *(either by the originator or by the sponsor)*, also enter this number(s).

10. AVAILABILITY/LIMITATION NOTICES: Enter any limitations on further dissemination of the report, other than those imposed by security classification, using standard statements such as:

(1) "Qualified requesters may obtain copies of this report from DDC."

(2) "Foreign announcement and dissemination of this report by DDC is not authorized."

(3) "U. S. Government agencies may obtain copies of this report directly from DDC. Other qualified DDC users shall request through _____."

(4) "U. S. military agencies may obtain copies of this report directly from DDC. Other qualified users shall request through _____."

(5) "All distribution of this report is controlled. Qualified DDC users shall request through _____."

If the report has been furnished to the Office of Technical Services, Department of Commerce, for sale to the public, indicate this fact and enter the price, if known.

11. SUPPLEMENTARY NOTES: Use for additional explanatory notes.

12. SPONSORING MILITARY ACTIVITY: Enter the name of the departmental project office or laboratory sponsoring *(paying for)* the research and development. Include address.

13. ABSTRACT: Enter an abstract giving a brief and factual summary of the document indicative of the report, even though it may also appear elsewhere in the body of the technical report. If additional space is required, a continuation sheet shall be attached.

It is highly desirable that the abstract of classified reports be unclassified. Each paragraph of the abstract shall end with an indication of the military security classification of the information in the paragraph, represented as *(TS)*, *(S)*, *(C)*, or *(U)*.

There is no limitation on the length of the abstract. However, the suggested length is from 150 to 225 words.

14. KEY WORDS: Key words are technically meaningful terms or short phrases that characterize a report and may be used as index entries for cataloging the report. Key words must be selected so that no security classification is required. Identifiers, such as equipment model designation, trade name, military project code name, geographic location, may be used as key words but will be followed by an indication of technical context. The assignment of links, rules, and weights is optional.